Towards improved sensitivity of solid-state NMR experiments in biosolids

Université Pierre et Marie Curie

L'Ecole doctorale de Chimie Physique et de Chimie Analytique de Paris Centre

Laboratoire des Biomolécules- UMR 7203

Towards Improved Sensitivity of Solid-State NMR Experiments in Biosolids

Par [Rudra Narayan Purusottam]

Thèse de doctorat de [Chimie Physique et Chimie Analytique]

Dirigée par [Dr. Piotr Tekely]

Présentée et soutenue publiquement le [18 septembre 2015]

Devant un jury composé de :

[M. Hartmut Oschkinat, Professuer (Rapporteur), M. Yoshitaka Ishii, Professuer (Rapporteur), Mme. Sabine Hediger, Chargé de Recherche (Examinateur), Mme. Sandrine Sagan, Directrice de Recherche (Examinateur), M. Geoffrey Bodenhausen, Professuer (Examinateur)]

This thesis is dedicated to my parents.

for their endless love, support and encouragement

Remerciements

First and foremost I would like to thank my supervisor Dr. Piotr Tekely for his encouragement, patient tutelage and invaluable support over the years. His scientific guidance and fruitful ideas was the base for my research work. Numerous interesting and stimulating discussions formed my scientific views and were a key point for my results. His trust and concerns on me allowed to keep my own scientific freedom and opinion and turned a hopeless project into a success. I would like to quote a line of his, which will remain etched on my memory throughout life ‘Anything is perfectible’. I can’t even fathom to reach the level of perfection he seeks in his students. All of it taken together makes him a great mentor and it was a pleasure working under his supervision.

I am fortunate to have studied under excellent colleagues and advisors. Among them is Prof. Geoffrey Bodenhausen; I am thankful to him for giving me the opportunity to work in his lab and for his motivation and insightful discussions about the research. I must also acknowledge my former supervisor during my Master’s degree dissertation thesis, Dr. Neeraj Sinha for introducing me to the field of NMR.

I recognize that this research would not have been possible without the financial assistance of the Université Pierre et Marie Curie (UPMC) doctoral school and the state of the art high-field NMR access provided by the Infrastructure de Recherche Très Grands Equipements de Résonance Magnétique Nucléaire à Très Hauts Champs (IR RMN THC) of the Centre National de la Recherche Scientifique (CNRS).

I would like to thank all former and current members of Geoffrey’s group for a wonderful time and stimulating discussions. For the non-scientific side of my thesis I am indebted to many friends here and back in India. I would like to single out Mouna Rouabah for putting up with me and always there cheering me up through the good times and bad. My life in Paris would have been incomplete without her. At last I want to thank my family for their unfailing encouragement, for never once questioning my capabilities and supporting me in all my pursuits. Seeing the pride in their eyes is the most meaningful thing to me in this world.

Sommaire

1 Overview of solid state NMR

1.1 Introduction

Solid-state nuclear magnetic resonance has emerged as an indispensable spectroscopic technique to provide atomic-scale information in heterogeneous complex biological systems and biopolymers [1]. Solution NMR spectroscopy has been extensively explored to this end, taking advantage of substantial experimental and spectral simplification due to the presence of time-averaging caused by rapid motional fluctuations signals Alternatively, high-resolution solid state NMR can be achieved when the anisotropic spin interactions are successfully removed by specific manipulations of spin system [2, 3]. A large part of solid-state NMR methodology refers indeed to the dissection of the anisotropic interactions or to suppressing of their influence on NMR spectra in a controlled manner. Solid-state NMR is a unique technique in structural biology, since local motions can be studied without the complexity of overall tumbling of biological complexes over a wide dynamic range With the recent stunning advances [4] in solid-state NMR and its unrivaled feasibility as compared with crystallographic and other spectroscopic techniques, it has emerged as a leading technique to reveal dynamic aspects of membrane proteins [5, 6], viruses [7, 8], amyloid fibrils [9] and native cellular components [10] at atomic resolution.

1.2 Dipolar spin interactions in solid state NMR

The magnetic moment of a nuclear spin often interacts with the magnetic field of another spin. This interaction is called spin-spin coupling and occurs between the same type (homonuclear) or different types (heteronuclear) of nuclei. Two modes of coupling are possible. The first is a direct interaction between the spins while the other is mediated through the electrons and is referred to as indirect coupling (*J*-coupling). The second mode involves polarizing electrons surrounding one nucleus, which gives rise to a magnetic field at the site of the second nucleus.

This indirect dipole-dipole interaction causes spins to be sensitive to their bond neighboring spins giving rise to multiplet peak structures observed in the spectra of most liquids. This is most routinely exploited in the determination of molecular structures, via solution-state NMR spectroscopy. The *J*-couplings are also observed in the solid state, where they can be orientationally dependent.

Couplings between the magnetic dipole moments of nuclei can also be experienced directly through space, which is known as direct dipolar coupling, D_{IS}. This interaction is characterized by the angle θ between the internuclear vector and the external magnetic field, and by the coupling constant b_{IS}

$$D_{IS} = b_{IS}\frac{1}{2}(3\cos^2\theta - 1)$$

The coupling constant between spins **I** and **S** is proportional to their respective gyromagnetic γ ratios and to the internuclear distance r_{IS}

$$b_{IS} = \frac{\mathrm{h}\mu_0\gamma_I\gamma_S}{4\pi r^3_{IS}}$$

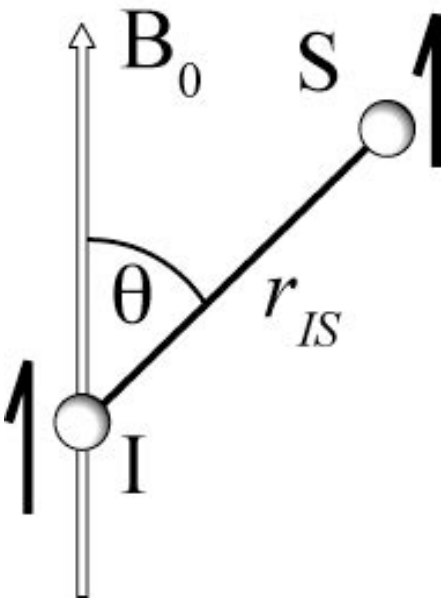

Figure 1.1 Dipolar two--spin system IS in the presence of an external magnetic field B_0.

The direct dipolar coupling is characterized by a traceless tensor [11], which means that it has an isotropic value of zero. This implies that the direct dipolar coupling is not manifesting in liquid-state NMR spectra due to the fast and isotropic molecular motion. Solid-state NMR spectra, however, can exhibit very strong dipolar coupling effect, ranging from a few Hz to several tens of kHz.

Strong homonuclear couplings give rise to homogenous line broadening, which can severely limit spectral resolution. Such interactions are especially strong and frequent in the case of abundant nuclei with large gyromagnetic ratios, such as ^{1}H, where these broad linewidths are common and spectra lack sufficient resolution to decipher structural information. In contrast, ^{13}C is only 1% natural abundant and has a small gyromagnetic ratio, which results in weak rarely occurring homonuclear interactions at natural abundance. Heteronuclear interactions from ^{1}H do not give rise to homogeneous line broadening and can be efficiently suppressed using decoupling sequences. In chapters 6 and 7 of the thesis we have addressed how sensitivity improvement can be achieved during heteronuclear decoupling in solid-state NMR at high MAS spinning frequencies and moderate radio-frequency amplitudes. Finally, it is crucial to have experimental control over coupling so that it can be either suppressed to improve spectral resolution, or introduced to measure internuclear distances and determine connectivities, as will be discussed in the first part of this thesis.

1.3 Basic experimental techniques: Magic-Angle Spinning (MAS) and Cross Polarization (CP)

Magic-angle spinning

Providing fast macroscopic spinning at the magic-angle, several anisotropic terms in the Hamiltonian such as the chemical shift and the heteronuclear dipolar coupling collapse to their trace value, resulting in isotropic spectra which resemble those obtained in the solution state. The magic angle (θ_m) can be defined as the angle between the *z*-axis and the body diagonal of a unit cube. Rotating an object about the direction of this diagonal would equally interchange its respective *x*,*y*,*z* coordinates and give rise to the equivalent to isotropic motion, as seen in fig.1.2 (left).

Magic-angle spinning NMR experiments on solids attempt to average out the orientational dependence of the nuclear spin interactions and suppress the relevant inhomogeneous broadening, significantly improving the spectral resolution [12-15] (shown in fig. 1.2, right).

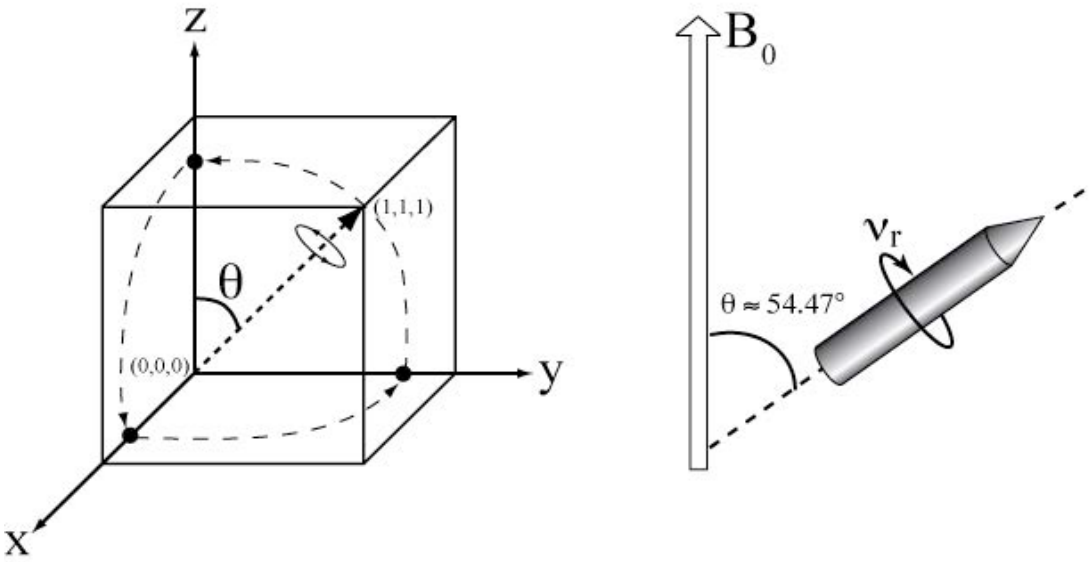

Figure 1.2 Geometrical interpretation of the magic angle (left); sample rotation at the magic angle in solid state NMR (right).

At magic angle, the spatial anisotropic part of the interactions, describable as second-rank tensors like the dipolar coupling or the chemical shift anisotropy (CSA), can be averaged out. The orientation dependence of these interactions is proportional to $3(\cos^2\theta\text{-}1)/2$, which is the second Legendre polynomial $P_2(\cos\theta)$. This expression becomes zero at $\theta = 54.74$, which is therefore called the magic angle, $\theta_{m.}$ Spin interaction effects that give rise to line broadening can only be effectively suppressed using spinning frequencies exceeding the magnitude of the internal interactions such as chemical shift anisotropy, dipolar or quadrupolar interactions. This is not often achievable at even modern limits of spinning speed. If the interactions are too strong to be removed by MAS, one obtains a manifold of spinning sidebands centered at the isotropic chemical shift of the spin and separated by rotational frequency. The appearance of sidebands is a result of the time-periodic modulation of internal interactions due to sample rotation.

As the envelope of the sideband pattern depends on the spectral features of each internal interaction, valuable information can be obtained on these interactions from the analysis of the relevant sideband amplitudes.

MAS itself does not suffice to suppress second-order quadrupolar broadening which results from a $P_4(\cos\theta)$ dependence. An elegant means to average out further such spectral features is the double rotation (DOR) technique [15], which requires spinning the sample at two angles simultaneously.

Cross polarization

Nuclei with smaller gyromagnetic ratio and low natural abundance give weak NMR signals. Nuclei of this type also tend to have long T_1 requiring lengthy relaxation delays [16]. In order to improve the signal-to-noise ratio (S/N) of such spectra, either the sample has to be isotopically enriched or long experimental times are required, both of which being expensive and often impracticable. These problems can be partially circumvented by using cross-polarization which involves magnetization transfer from an abundant nucleus to the rare/low gamma nucleus of interest [17]. CP exploits the flip-flop transitions, the mutual 'up-down/down-up' zero-quantum transitions (also called spin exchange or spin diffusion) that in the absence of rf fields occur only between strongly coupled homonuclear spins.

In principle, I→ S cross-polarization can give an enhancement factor of γ_I/γ_S. CP transfer from spin I to spin S is established by creating a transverse I magnetization, via a $\pi/2$ r.f. pulse, followed by a simultaneous spin-locking field B_{1I} along the direction of the I magnetization and irradiation on the S channel. The rf amplitudes on both channels must meet the Hartmann-Hahn condition ($\omega_{1I} = \gamma_I B_{1I} = \gamma_S B_{1S} = \omega_{1S}$), allowing for cross-polarization to take place and leading to the build-up of S magnetization during the contact period.

When the irradiation terminates on both channels, it is followed by simultaneous detection of spin S and decoupling of spin I, as shown in fig. 1.3.

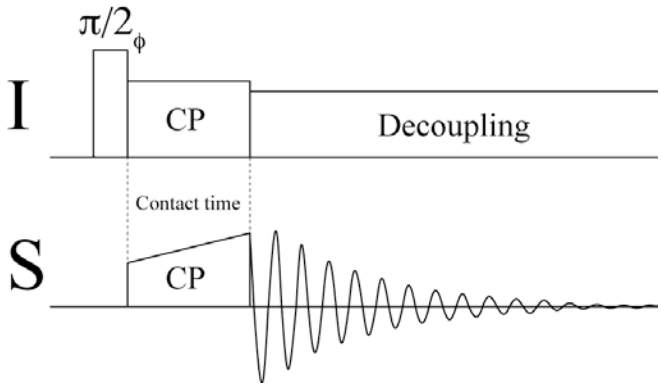

Figure 1.3: Standard pulse sequence for Hartmann-Hahn cross-polarization transfer from abundant spin I to low-gamma spin S.

The optimum duration of the magnetization transfer, referred to a contact time, is determined by the $T_{1\rho}$ of spin I. The rate of polarization transfer, k_{IS}, is a complex function of the dipolar couplings between the two spins. The dynamics of the I → S CP is characterized by $T_{1\rho}$ and k_{IS}. The magnetization of abundant nuclei decreases exponentially with contact time, at a rate of 1 / $T_{1\rho}$ (I), while that of the low-gamma nuclei grows at a rate determined by k_{IS}, reaching a maximum and subsequently decaying at a rate determined by $T_{1\rho}$(S).

The development of cross-polarization techniques revolutionized modern NMR spectroscopy for solids and made it suitable for routine application. CP provides a many-fold enhancement of the signal to noise ratio for low-gamma nuclei on a per scan basis. In addition, it allows for a faster repetition rate as it is limited by T_1(I) rather than T_1(S), which is usually longer, often by orders of magnitude. As a result, the signal to noise ratio over a fixed experimental duration is improved dramatically.

Spectral assignment requires heteronuclear transfer steps that allow a direct magnetization transfer from one spin to the next in the polypeptide chain, to obtain the sequential assignment. To achieve heteronuclear transfer in polypeptides, the conventional CP approach has been modified for polarization transfer between ^{15}N-^{13}C spins in a chemical shift selective manner [17]. Selective magnetization transfer between the backbone nitrogen atom and the Cα or C′ carbon atom can be established using specific CP (^{15}N-^{13}C CP) experiments, where off-resonance low power r.f.pulses are applied to spin lock the ^{15}N and ^{13}C spins. The spin locking has to fulfil the specific-CP matching condition. The low r.f. applied ensures that the CP is band-

selective, while the off-resonance components can be adjusted to fulfil the specific-CP conditions for NCA or NCO spectra. Additionally, a gain in sensitivity for such an experiment was observed by applying an adiabatic pulse shape to one of the CP pulses [18].

NCA and NCO experiments can be extended by a DREAM scheme [19], yielding N(CA)CB, N(CO)CA and N(CA)CO experiments which can also be run in a three dimensional fashion. In ideal cases, these schemes can be extended to record a four dimensional CANCOCX experiment [20]. However, for such experimental schemes relatively high signal-to-noise (S/N) ratios are necessary.

1.4 Dipolar recoupling and decoupling

Recoupling

Solid state MAS NMR permits to record high-resolution spectra determined by the isotropic chemical shifts. Although magic-angle spinning [12, 14] introduces high resolution by suppressing the anisotropic broadening, it also average out the nuclear dipole-dipole interactions that are the source of most structural information in the spectra. Such information can be reintroduced by the application of a carefully chosen sequence of radiofrequency pulses which is referred to as dipolar recoupling. In other words, recoupling refers to the reintroduction of anisotropic NMR interactions, mainly the dipolar interactions, which are otherwise averaged out by MAS. Since these interactions are orientation and/or distance dependent, their controlled reintroduction can yield structural information. Today, a plethora of recoupling pulse sequences exists suited to tackle structure determination of biomolecular systems [21].

Structure information in solid-state NMR is mostly derived from the low-gamma nuclei like ^{13}C and ^{15}N, with 2D ^{13}C-^{13}C correlation experiments playing a prominent role. The dipolar mediated ^{13}C-^{13}C correlations can be obtained with first-order homonuclear dipolar recoupling schemes [19, 22-24]. These schemes suffer from dipolar truncation effects where strong dipolar couplings mask the weaker ones [25]. Whilst this effect helps in the selective observation of directly bonded carbon atoms, which is very helpful in assigning the ^{13}C resonances in a protein skeleton, the same effect makes these schemes unsuitable for observing intermediate and long-

range ^{13}C-^{13}C contacts, which are essential for determining tertiary structure of proteins. A number of recoupling schemes with attenuated dipolar truncation are available today [26-30]. Second-order dipolar recoupling schemes are one such kind of schemes and have been widely used to observe a range of range ^{13}C-^{13}C correlations [31, 32]. Proton Driven Spin Diffusion (PDSD) [31], Dipolar Assisted Rotational Resonance (DARR) [32]/ Rf Assisted Diffusion (RAD) [33], Phase Alternated Recoupling Irradiation Schemes (PARIS) [34-37] and the recently introduced Second-order Hamiltonian among Analogous Nuclei Generated by Heteronuclear Assistance Irradiation (SHANGHAI) [38] and Proton Assisted Recoupling (PAR) [39] come under the category of second-order recoupling schemes.

Dipolar couplings between spin-1/2 and quadrupolar nuclei can be measured using Transfer of Population in Double Resonance (TRAPDOR) [40-42] or 'Rotational-Echo, Adiabatic Passage Double Resonance' (REAPDOR) [43-46] experiments. Other examples of recoupling sequences include Dipolar Recovery at the Magic Angle (DRAMA) [47], Transferred Echo Double Resonance (TEDOR) [48, 49], and the numerous symmetry-based sequences. C_n^N and R_n^N. [50-59]. Another example of a two-dimensional dipolar recoupling experiment is the Rotational Echo Double Resonance, first introduced by Gullion et al [59]. The REDOR sequence is commonly used to measure heteronuclear distances in the range of 2–8 Å. [60-62].

For a strongly dipolar-coupled spin pair it is possible, in principle, to create a double quantum coherence. Through a series of r.f. pulses a double-quantum coherence between two spins can be excited and subsequently allowed to evolve under dipolar coupling. One the most commonly used experiments for exciting the double quantum coherence is the back-to-back (BABA) sequence. [63, 64]. Such sequences, which are referred to as double quantum filters (DQF), provide information about the dipolar coupling between two spins, from which spatial configuration and proximity at the atomic level can be determined. BABA is also commonly used in heteronuclear correlation experiments, where applying a pulse sequence on both spin channels simultaneously creates the double-quantum coherence between two different spins. These sequences are usually a part of a two-dimensional experiment and allow for measuring homonuclear and heteronuclear dipolar couplings.

The retrospective review of recoupling techniques is not easy because of multiple contributions strongly influenced by pioneering work in the early days of NMR related to spin echo experiments [64, 65], the development of double-resonance experiments [leading to the CP transfer experiment [66], proton-enhanced nuclear induction spectroscopy [67, 68], CP under MAS conditions [69], and the experimental observation by Andrew et al. [70] of line-broadening effects (i.e., R^2) when the spinning frequency matches the chemical shift difference.

Decoupling

Heteronuclear dipolar decoupling in solid-state NMR of biosolids relates to the decoupling of low-gamma nuclei from the protons. The mode of action of strong rf pulses applied to the proton spins may be imagined as to cause a fast nutation of the proton spins around the effective field with frequency higher than the heteronuclear dipolar couplings. In fact, the nutation frequency also has to be larger than the homonuclear dipolar proton couplings. MAS modulate spatial part of the NMR interactions while application of heteronuclear dipolar decoupling scheme perturbs the spin part of dipolar interaction. In its simplest form, heteronuclear decoupling refers to the application of high-power continuous wave (CW) r.f. irradiation on the proton channel. However, interference effects between heteronuclear dipolar couplings and the proton chemical shift anisotropy through second-orded terms in spin Hamiltonian can compromise the performance of CW decoupling, especially at fast MAS. This interference is significantly reduced in the case of phase-modulated sequences like two-pulse phase modulation (TPPM) [71] and its phase-cycled version, small phase incremental alternation (SPINAL) [72]. There exist a large number of modifications of these two basic decoupling sequences. With increasing MAS frequency, more sophisticated decoupling sequences like PISSARRO [73] usually perform better than TPPM or SPINAL.

Besides high-power irradiation, some of these heteronuclear decoupling sequences can be applied as low-power variants at very fast MAS spinning frequencies. Low-power decoupling prevents excessive sample heating, which may be of particular importance for lossy biological samples, although slight losses in performance usually have to be accepted. Generally, the subtle differences among different decoupling pulse sequences manifest in the higher order terms of their effective Hamiltonians

[74]. Chapter 6 of the thesis gives a more detailed description of the latest heteronuclear decoupling schemes and an analysis of their performance in a large range of static magnetic fields and spinning frequencies.

As mentioned earlier, high resolution in ^{1}H MAS NMR spectroscopy is often elusive due to strong homonuclear dipolar interactions and small range of isotropic chemical shifts. Homonuclear dipolar decoupling in solid-state NMR usually relates to proton-proton decoupling. A powerful way to achieve additional spin space averaging of these couplings is the Lee–Goldburg (LG) irradiation technique [75]. It is achieved by tilting the effective rf field to the magic angle by means of offset irradiation on the ^{1}H channel, which suppresses dipolar proton-proton couplings to the lowest order, leaving the heteronuclear dipolar coupling scaled by $1/\sqrt{3}$. LG technique is routinely used in its frequency and phase modulated versions, which average out the homonuclear ^{1}H-^{1}H couplings to higher order [76-78]. These homonuclear decoupling techniques have proven very effective in enhancing resolution in NMR spectra under fast MAS conditions, as well as in suppressing spin diffusion.

1.5 Sensitivity enhancement techniques

Sensitivity enhancement strategies

NMR spectroscopy has become an indispensable tool with innumerable applications in physics, chemistry, biology and medicine. One of the main obstacles in NMR is its notorious lack of sensitivity which is due to the low equilibrium polarization of nuclear spins at ambient temperature. Sensitivity-enhancing strategies promise to extend this spectroscopy to larger and more biologically interesting systems than previously feasible. A myriad of advancements have been made over the years to address this issue. It takes a mutual investment not only by the practitioners of art but also at instrumental engineering level too. Overall the strategies can be summarized as follows:

a) Ultra-high magnetic fields

Advances to build ultra-high field magnets place the most stringent demands on field-strength, stability and homogeneity. This critically depends upon availability of suitable materials for superconducting wires, robust cryostat technology in the long-term operation and a lot of other factors. Increasing the static magnetic field (B_0), which dictates the Larmour frequency of the spin as well as Boltzmann population distribution on spin energy levels leads to increase the NMR signals through a B_0^{α} dependency with $\alpha>1$. Efforts are being made to develop low-temperature superconductor outer coil and high-temperature superconductor inner coil or LTS/HTR magnets to generate static-field beyond already existing 1 GHz magnets for high-resolution NMR spectroscopy [79]. Another promising advance in this area are the hybrid magnets, consisting of a resistive magnet located inside a superconducting coil and operated in series to achieve the highest possible continuous magnetic fields as well as an enhanced inductive-derived stability [80]. However, the operational costs of these hybrid magnets are quite higher as compared to non-stop operation of superconducting magnets.

b) Better performing probes and coil designs

Improving the electronics can also significantly enhance the sensitivity of NMR spectrometer. Some advances made in this area in the recent years are the development of cryoprobes and coil geometries. Solenoids are the most common geometry for magnetic resonance microcoils probe that improves the sensitivity per unit sample volume whereas for the cryoprobes, which operate between 20-77 K copper-based saddle coils are preferred. Significant gain in S/N ratio up to a factor of 4 has been achieved employing this in protein NMR studies. Additionally using high-temperature superconductors (HTS) can even further boost the sensitivity. Some other specialized probes to suit special needs have also been developed in the past few years. The E-free probes consisting of a low inductance proton coil reduces r.f. sample heating which results from the interaction between the electric field and the sample. In the case of hydrated and lossy biological samples the use of high power

proton decoupling can lead to excessive sample heating [81]. Reducing the E-field at the location of the sample can alleviate this situation.

The recently released ultra-fast magic angle spinning capabilities of 111 kHz MAS probe allows for the direct and high resolution observation of proton resonances from complex biomolecules. It gives double the resolution in protonated samples compared to it's counterpart 60 kHz MAS probe. The use of ultrafast MAS provides sensitivity enhancement through increased ^{1}H transverse relaxation time (T_2). These new tools in the solid-state NMR spectroscopist's arsenal are quite beneficial to extract atomic-scale information in complex biological systems.

c) Sample optimization

Although not directly related to the sensitisity issue, the sample preparation for NMR experiments in biosolids can influence significantly the quality of recorded spectra. Freezing, freeze-drying and crystallization can be used to prepare the samples. The first two approaches lead to poor resolution and heterogeneous samples even in the presence of cryoprotectants. Microcrystalline proteins on the other hand give high-resolution spectrum and serve as an ideal benchmark for methodology development in solid-state NMR [82, 83]. Recently another method of preparing samples has been introduced by ultracentrifugation [84]. The transient sedimented state is achieved from a clear protein solution by centrifugal force exerted by spinning of MAS rotors [85]. It is a milder technique and gives comparable spectra in term of resolution like the microcrystalline proteins. The efficiency of sedimentation depends on the molecular weight and concentration of the protein. For small globular proteins it can be bound to a complex to increase the molecular weight and ease the sedimentation [86]. Since sedimentation promises to become a viable additional option for the preparation of samples for solid- state NMR spectroscopy, prediction tools are being developed for the best sedimentation strategy [87]. Even increasing the filling factor of the sample by raising the concentration of an analyte, will result in concomitant gain in the S/N ratio.

d) **Optimized pulse sequences**

NMR being a unique flexible tool where advances in understanding the spin physics underlying the experiment are directly linked to improvements in the amount of information that can be extracted from it. In recent years there have been major advances in the development of sensitivity enhanced experiments and fast data acquisition. Both of these aspects are in fact somewhat linked, as improvements in S/N ratios bring about reductions in the time needed for an experiment, and vice versa. Reducing the recovery times of the observed nuclei renders substantial increases in sensitivity per unit signal averaging time. Adding a paramagnetic relaxation agent will shorten the longitudinal relaxation time of the spins without bringing about a concomitant transverse relaxation decrease (i.e. line broadening) [88]. Alternate way is to increase the relaxation of surrounding water by addition of lanthanide based relaxation agents to the solvent [89]. In the case of solids the inherently strong dipole based broadening makes it even difficult to benefit from fast recycling due to indispensable high power needed during the experiments to get rid of these interactions. Although with the realization of fast MAS (>40 kHz) in combination with low-power pulse schemes and paramagnetic doping this problem has been circumvented [88]. Implementing low r.f. power schemes during recoupling [35], decoupling [90, 91] and cross-polarization [92, 93]that is mild to both the sample and the electronics hardware also obviates this need and thereby enabling faster recycling. Solid-state NMR experiments employing low power during are also of particular advantage when studying lossy biological or fully hydrated heat sensitive samples.

In NMR typically one species of nuclei is observed and interactions with other species are undesirable during acquisition. These unwanted interactions are averaged out by use of heteronuclear decoupling sequences. This is the case for liquid as well as solid-state NMR; however, since the interactions are stronger in solid-state NMR the need for efficient decoupling schemes becomes very pronounced. The interactions in the solid-state are so strong that the favourite nucleus for observation in biological samples, the proton, becomes less attractive due to huge dipolar couplings and the petite frequency dispersion. However, a few studies [94-97] have shown that the use of perdeuterated proteins makes solid-state proton detection feasible by diluting the proton dipolar network [98, 99].

This leaves the spectroscopist working with biosolids with the carbon-13 nucleus as the main observable. However, if not avoided during sample preparation, a network of dipolar coupled protons are present in the sample and interactions through the heteronuclear dipolar couplings between the protons and the carbons lead to fast relaxation and dephasing of the carbon magnetization. So even using the carbon-13 nuclei, which show a significantly wider frequency, the decoupling of the protons remains critical. Some recent breakthrough developments in magic angle spinning (MAS) NMR technology have made it possible to spin solid samples up to 110 kHz frequencies. With such remarkable capabilities, ^{1}H-detected NMR experiments that have traditionally been challenging on rigid solids can now be implemented [100].

e) Increased sensitivity by spin-alignment transfer techniques

The detected signals from an ensemble of nuclear spins can be enhanced by transferring the spin polarization from electrons, which have a large magnetic moment to the observable nuclei of interest. Irradiation from microwave sources like gyrotron mediates the electron-nuclear transitions. This theoretical concept was introduced by Overhauser and is referred to as Dynamic nuclear polarization (DNP) [101]. The first application of this method followed shortly thereafter in metals [102]. With the development of microwave sources for ultra-high magnetic field strengths, the past decade has witnessed promising applications of DNP to several areas of magnetic resonance including high resolution liquid state [103, 104] (dissolution DNP), in vivo NMR studies [105], metabolic studies [106] etc.

DNP also offers tremendous opportunity for the enhancement of solid-state NMR signals [107]. This typically requires a high-power microwave source and low-temperature capabilities, as well as polarization agents that serve as the electron spin reservoir. Application of DNP in solid-state NMR has yielded significant signal enhancements for membrane proteins [108, 109] and other complex biological samples such as intact viruses [110], bacterial cell walls [111] and whole cells [112]. With such improvements, biological solid-state NMR will open new ways for in situ structural studies of small compounds in their biologically active state.

In materials which have low surface areas and/or low concentrations of active/surface sites, application of DNP to enhance surface NMR signals, an approach known as DNP surface enhanced NMR spectroscopy (DNP SENS) has proven immensely

useful [113]. Enabling DNP for these systems requires bringing an exogenous radical solution into contact with surfaces without diluting the sample of interest. Such enhancement enables the comprehensive and expedient atomic level characterization of the surfaces of complex materials at natural isotopic abundance by NMR.

f) Spin-alignment alternatives: Nuclear Hyperpolarization by para-Hydrogen & optical pumping

Apart from polarization transfers from unpaired electrons reservoir to achieve nuclear hyperpolarization, another source of polarization is the H_2 molecule itself. Hydrogen molecule exists at room temperature as two isomeric forms: *ortho* and *para*-hydrogen. Although para-hydrogen itself has no net spin angular momentum and is NMR silent, it can be used as a reagent to create reaction products that possess non- Boltzmann nuclear distributions with high degrees of spin alignment. Hydrogen can be enriched in the *para* form at low temperature in the presence of a paramagnetic catalyst. Following the addition of *para*-H_2 to an unsaturated substrate, the perturbation of the spin populations is maintained in the product, and typical NMR spectra characterized by strongly enhanced signals and adsorption-emission patterns are observed. This procedure is termed as para-Hydrogen-induced polarization (PHIP) and is limited to molecules with unsaturation double or triple bonds [114, 115]. Depending on whether the chemical reaction is conducted in the high or very low magnetic field there are two protocols leading to different signal patterns, named PASADENA (Parahydrogen And Synthesis Allow Dramatically Enhanced Nuclear Alignment) and ALTADENA (Adiabatic Longitudinal Transfer After Dissociation Engenders Nuclear Alignment). Another alternative is to transfer the *para*-H_2 derived spin order to other molecules via reversible interactions, without hydrogenation termed as SABRE (Signal Amplification By Reversible Exchange) [116].

An important current trend in solid-state nuclear magnetic resonance is also the exploitation of optical pumping of nuclear spin polarizations as a means of enhancing and localizing NMR signals. Recent work in this domain focuses mainly in two areas, namely optically pumped NMR in semiconductors and optical pumping of noble gases. Xenon (^{129}Xe) is an attractive substrate because it is usually not present in living organisms and optical pumping is a rather easy method for imparting hyperpolarization, and because it can resonate over a wide range of chemical shifts,

thus being an accurate reporter for changes in its proximity. Introducing optically pumped noble gases can boost NMR sensitivity by three to four orders of magnitude. In addition ^{129}Xe is particularly well suited for biosensing applications because it is a nontoxic element that retains its laser-induced polarization for relatively long time periods [117].

1.6 Introduction to internal dynamics in biomolecules

The synergy between structure and dynamics is essential to the function of biological macromolecules. For a comprehensive understanding of key biological processes, collective information of the static three-dimensional structures and the pivotal dynamic character associated with the biomolecules involved are required. Proteins are central to many cellular functions, and the urge to unveil the secrets of these complex biomolecules has baffled researchers for decades. The initial outburst in determination of protein structures is now being emulated by consideration of their dynamics as well [118]. NMR is a powerful tool in providing unprecedented atomic level dynamics information of proteins ranging from 10^{-12}(ps) to 10^{2}(s) [119]. Many NMR observables serve as highly sensitive probes to precisely characterize motions of protein backbones and side-chains. When it comes to investigate biological macromolecular assemblies or heterogeneous biological systems, solid-state nuclear magnetic resonance is the most preferred method with no inherent size limitation.

It is used primarily to decipher the intramolecular motions of proteins that are immobilized as part of supramolecular structures in solution, such as membrane proteins [6], virus particles [7] or crystalline samples [120], Many studies have shown striking evidence that often the intramolecular motions in suitably hydrated solid samples are quite similar to those encountered in solution [121-123].
Hitherto most of the site-specific protein dynamics studies by solid-state NMR in the picoseconds-nanoseconds timescale rely primarily on exploiting spin-lattice relaxation rate (R_1) of ^{13}C/^{15}N nuclei [124-127].

One of the major drawback of this is its high susceptibility to spin-diffusion, presence of paramagnetic impurities and also MAS dependency [128] which makes precise quantitative analysis a daunting task. Another highly sensitive site-specific relaxation observable in the same motional timescale regime is heteronuclear nuclear

Overhauser effect (NOE). Heteronuclear NOE 1H-^{13}C/^{15}N has been previously observed in microcrystalline proteins [129-131]. The fast rotating methyl groups benefit the most from this effect, also the most mobile parts of the protein, especially in side-chains that are inherently mobile, also benefit to some degree.

1.7 Heteronuclear Overhauser Effect in organic solids

The use of nuclear Overhauser effect (NOE) [132, 133] as a tool for structural elucidation has been extensively demonstrated in solution-state NMR [134]. It is one of the most widely exploited phenomena in solution-state NMR but NOEs in the solid state are rare. The effect arises through cross-relaxation driven by the modulation of the dipolar interaction between two spatially proximate spins, conventionally labelled I and S. Upon perturbation of the populations of the I-spin energy levels, cross-relaxation processes act to return the populations of the energy levels to their equilibrium values. This has the simultaneous effect of altering the population differences across the S-spin system through zero- and double quantum transitions, so leading to the observed change in S-spin signal intensity. This says that for zero mixing time (τ_m) the S magnetization is equal to its equilibrium value, but that as the mixing time increases the S magnetization has an additional contribution depending on the mixing time and the cross-relaxation rate, σ_{IS}. This latter term results in a change in the intensity of the S spin signal, and this change is called an NOE enhancement.

The normal procedure for visualizing these enhancements is to record first a reference spectrum in which the intensities are unperturbed. Modulation of the dipole-dipole interaction arises due to the presence of molecular motion on the appropriate timescale. In the solution state, this motion exists as a result of the rapid, random tumbling. In the solid state, such motions are rarely observed due to the structural rigidity imposed on the molecules, so mainly the rapid rotation of methyl groups or modulation of dipolar interactions by rapid molecular tumbling leads to enhancement of the ^{13}C/^{15}N signal intensity.

The heteronuclear Overhauser effects in solids have been observed first in a single crystal of L-alanine [135], small molecules and polymers [136] and more recently in a microcrystalline protein [129, 130]. More particularly, the nuclear Overhauser polarization (NOP) induced by DARR irradiation [32] has been used to

enhance single-pulse ^{13}C spectra of glycilisoleucine and threonine [137] and of lyophilized proteins [138].

Steady-state and transient NOE

The NOE itself depends on the competing balance between various relaxation pathways. In aforementioned difference NOE experiment, a relatively long (in the order of seconds), low-power irradiation to saturate I spins is used. During this time, the NOE will gradually build-up, as we start saturating I spin more and more. What we get after sufficiently long irradiation is the so-called "steady state NOE", i.e. the steady state population distribution of the neighboring spins that derives from two counter-acting effects: the NOE build-up from cross relaxation with the irradiated spin I and the T_1 relaxation of the spins that have deviated from their Boltzmann equilibrium due to the NOE, trying to bring them back to the equilibrium state. Instead of steady-state saturation, an inversion of the I spin magnetization can be used:

(180^o) (I) —t_{CR}— 90^o (S)—acquisition

The transient build-up of the S spins magnetization is followed as a function of time t_{CR}.

In chapter 2 of this thesis we have exploited both steady-state and transient heteronuclear nuclear Overhauser effect for recording one and two-dimensional ^{13}C spectra with enhanced sensitivity in microcrystalline proteins and a membrane protein [130].

In chapter 3 we have used site-specific heteronuclear transient NOE experiments for studying site-specific dynamics in a biological macromolecular assembly. We show the potential of this method and their advantage over routinely used longitudinal relaxation parameters which are more susceptible to be affected by motionally irrelevant spin diffusion and by paramagnetic impurities.

1.8 References

1. Mcdermott, A.E. and T. Polenova, Solid-state NMR studies of biopolymers. 2010, Chichester, West Sussex: John Wiley & Sons.
2. Mehring, M. Principles of High Resolution NMR in Solids. 1983;
3. Häeberlen, U., High resolution NMR in solids : selective averaging. 1976, New York [u.a.]: Acad. Pr.
4. Separovic, F. and A. Naito. Advances in biological solid-state NMR : proteins and membrane-active peptides. 2014;
5. Mcdermott, A., *Annu. Rev. Biophys.* 2009, 38 (1), 385-403.
6. Hong, M., Y. Zhang, and F. Hu, *Annu. Rev. Phys. Chem.* 2012, 63 (1), 1-24.
7. Opella, S.J., A.C. Zeri, and S.H. Park, *Annu. Rev. Phys. Chem.* 2008, 59 (1), 635-657.
8. Quinn, C.M., M. Lu, C.L. Suiter, G. Hou, H. Zhang, and T. Polenova, *Prog. Nucl. Magn. Reson. Spectrosc.* 2015, 86–87 (0), 21-40.
9. Tycko, R., *Annu. Rev. Phys. Chem.* 2011, 62 (1), 279-299.
10. Renault, M., R. Tommassen-Van Boxtel, M.P. Bos, J.A. Post, J. Tommassen, and M. Baldus, *Proc. Natl. Acad. Sci. U.S.A.* 2012, 109 (13), 4863-4868.
11. Chandra Shekar, S. and A. Jerschow, Tensors in NMR, in *eMagRes*. 2007, John Wiley & Sons, Ltd.
12. Andrew, E.R., A. Bradbury, and R.G. Eades, *Nature* 1958, 182 (4650), 1659-1659.
13. Andrew, E.R., A. Bradbury, and R.G. Eades, *Nature* 1959, 183 (4678), 1802-1803.
14. Lowe, I.J., *Phys. Rev. Lett.* 1959, 2 (7), 285-287.
15. Samoson, A., E. Lippmaa, and A. Pines, *Mol. Phys.* 1988, 65 (4), 1013-1018.
16. Duer, M.J., Solid-State NMR Spectroscopy: principles and applications. 2002, Oxford: Blackwell Science.
17. Baldus, M., A.T. Petkova, J. Herzfeld, and R.G. Griffin, *Mol. Phys.* 1998, 95 (6), 1197-1207.
18. Baldus, M., D.G. Geurts, S. Hediger, and B.H. Meier, *J. Magn. Reson. A* 1996, 118 (1), 140-144.
19. Verel, R., M. Ernst, and B.H. Meier, *J. Magn. Reson.* 2001, 150 (1), 81-99.
20. Franks, W.T., K. Kloepper, B. Wylie, and C. Rienstra, *J. Biomol. NMR* 2007, 39 (2), 107-131.
21. De Paëpe, G., *Annu. Rev. Phys. Chem.* 2012, 63 (1), 661-684.
22. Bennett, A.E., C.M. Rienstra, J.M. Griffiths, W. Zhen, P.T. Lansbury, and R.G. Griffin, *J. Chem. Phys* 1998, 108 (22), 9463-9479.
23. Hohwy, M., C.M. Rienstra, C.P. Jaroniec, and R.G. Griffin, *J. Chem. Phys* 1999, 110 (16), 7983-7992.
24. Lafon, O., J. Trebosc, B. Hu, G.D. Paepe, and J.-P. Amoureux, *Chem. Commun.* 2011, 47 (24), 6930-6932.
25. Bayro, M.J., M. Huber, R. Ramachandran, T.C. Davenport, B.H. Meier, M. Ernst, and R.G. Griffin, *J. Chem. Phys* 2009, 130 (11), 114506.
26. Levitt, M.H., D.P. Raleigh, F. Creuzet, and R.G. Griffin, *J. Chem. Phys* 1990, 92 (11), 6347-6364.
27. Ramachandran, R., V. Ladizhansky, V.S. Bajaj, and R.G. Griffin, *J. Am. Chem. Soc.* 2003, 125 (50), 15623-15629.
28. Paravastu, A.K. and R. Tycko, *J. Chem. Phys* 2006, 124 (19), 194303.

29. Marin-Montesinos, I., G. Mollica, M. Carravetta, A. Gansmüller, G. Pileio, M. Bechmann, A. Sebald, and M.H. Levitt, *Chem. Phys. Lett.* 2006, 432 (4–6), 572-578.
30. Scholz, I., M. Huber, T. Manolikas, B.H. Meier, and M. Ernst, *Chem. Phys. Lett.* 2008, 460 (1–3), 278-283.
31. Szeverenyi, N.M., M.J. Sullivan, and G.E. Maciel, *J. Magn. Reson.* 1982, 47 (3), 462-475.
32. Takegoshi, K., S. Nakamura, and T. Terao, *Chem. Phys. Lett.* 2001, 344 (5–6), 631-637.
33. Morcombe, C.R., V. Gaponenko, R.A. Byrd, and K.W. Zilm, *J. Am. Chem. Soc.* 2004, 126 (23), 7196-7197.
34. Weingarth, M., G. Bodenhausen, and P. Tekely, *J. Am. Chem. Soc.* 2009, 131 (39), 13937-13939.
35. Weingarth, M., G. Bodenhausen, and P. Tekely, *Chem. Phys. Lett.* 2010, 488 (1–3), 10-16.
36. Weingarth, M., D.E. Demco, G. Bodenhausen, and P. Tekely, *Chem. Phys. Lett.* 2009, 469 (4–6), 342-348.
37. Weingarth, M., Y. Masuda, K. Takegoshi, G. Bodenhausen, and P. Tekely, *J. Biomol. NMR* 2011, 50 (2), 129-136.
38. Hu, B., O. Lafon, J. Trébosc, Q. Chen, and J.-P. Amoureux, *J. Magn. Reson.* 2011, 212 (2), 320-329.
39. De Paëpe, G., J.R. Lewandowski, A. Loquet, A. Böckmann, and R.G. Griffin, *J. Chem. Phys* 2008, 129 (24), 245101.
40. Grey, C.P. and A.J. Vega, *J. Am. Chem. Soc.* 1995, 117 (31), 8232-8242.
41. Vaneck, E.R.H., R. Janssen, W. Maas, and W.S. Veeman, *Chem. Phys. Lett.* 1990, 174 (5), 428-432.
42. Ba, Y., H.M. Kao, G.P. Grey, L. Chopin, and T. Gullion, *J. Magn. Reson.* 1998, 133 (1), 104-114.
43. Holland, G.P. and T.M. Alam, *PCCP* 2005, 7 (8), 1739-1742.
44. Huang, W.L., A.J. Vega, T. Gullion, and T. Polenova, *J. Am. Chem. Soc.* 2007, 129 (43), 13027-13034.
45. Hughes, E., T. Gullion, A. Goldbourt, S. Vega, and A.J. Vega, *J. Magn. Reson.* 2002, 156 (2), 230-241.
46. Tycko, R. and G. Dabbagh, *Chem. Phys. Lett.* 1990, 173 (5-6), 461-465.
47. Hing, A.W., S. Vega, and J. Schaefer, *J. Magn. Reson.* 1992, 96 (1), 205-209.
48. Hing, A.W., S. Vega, and J. Schaefer, *J. Magn. Reson., Ser A* 1993, 103 (2), 151-162.
49. Brinkmann, A., M. Eden, and M.H. Levitt, *J. Chem. Phys.* 2000, 112 (19), 8539-8554.
50. Brinkmann, A. and M.H. Levitt, *J. Chem. Phys.* 2001, 115 (1), 357-384.
51. Kristiansen, P.E., M. Carravetta, W.C. Lai, and M.H. Levitt, *Chem. Phys. Lett.* 2004, 390 (1-3), 1-7.
52. Kristiansen, P.E., M. Carravetta, J.D. Van Beek, W.C. Lai, and M.H. Levitt, *J. Chem. Phys.* 2006, 124 (23), 1-19.
53. Madhu, P.K., X. Zhao, and M.H. Levitt, *Chem. Phys. Lett.* 2001, 346 (1-2), 142-148.
54. Marin-Montesinos, I., D.H. Brouwer, G. Antonioli, W.C. Lai, A. Brinkmann, and M.H. Levitt, *J. Magn. Reson.* 2005, 177 (2), 307-317.

55. Paul, S., R.S. Thakur, M. Goswami, A.C. Sauerwein, S. Mamone, M. Concistre, H. Forster, M.H. Levitt, and P.K. Madhu, *Journal of Magnetic Resonance* 2009, 197 (1), 14-19.
56. Van Beek, J.D., R. Dupree, and M.H. Levitt, *J. Magn. Reson.* 2006, 179 (1), 38-48.
57. Zhao, X., M. Eden, and M.H. Levitt, *Chem. Phys. Lett.* 2001, 342 (3-4), 353-361.
58. Zhao, X., W. Hoffbauer, J. Gunne, and M.H. Levitt, *Solid State Nucl. Magn. Reson.* 2004, 26 (2), 57-64.
59. Gullion, T. and J. Schaefer, *J. Magn. Reson.* 1989, 81 (1), 196-200.
60. Gan, Z.H., *Journal of Magnetic Resonance* 2006, 183 (2), 235-241.
61. Vogt, F.G., S.M. Mattingly, J.M. Gibson, and K.T. Mueller, *Journal of Magnetic Resonance* 2000, 147 (1), 26-35.
62. Feike, M., D.E. Demco, R. Graf, J. Gottwald, S. Hafner, and H.W. Spiess, *J. Magn. Reson., Ser A* 1996, 122 (2), 214-221.
63. Sommer, W., J. Gottwald, D.E. Demco, and H.W. Spiess, *J. Magn. Reson., Ser A* 1995, 113 (1), 131-134.
64. Hahn, E.L., *Physical Review* 1950, 80 (4), 580-594.
65. Pines, A., W.-K. Rhim, and J.S. Waugh, *J. Magn. Reson.* 1972, 6 (4), 457-465.
66. Hartmann, S.R. and E.L. Hahn, *Physical Review* 1962, 128 (5), 2042-2053.
67. Pines, A., M.G. Gibby, and J.S. Waugh, *J. Chem. Phys* 1973, 59 (2), 569-590.
68. Pines, A., M.G. Gibby, and J.S. Waugh, *J. Chem. Phys* 1972, 56 (4), 1776-1777.
69. Stejskal, E.O., J. Schaefer, and J.S. Waugh, *J. Magn. Reson.* 1977, 28 (1), 105-112.
70. Andrew, E.R., S. Clough, L.F. Farnell, T.D. Gledhill, and I. Roberts, *Physics Letters* 1966, 21 (5), 505-506.
71. Bennett, A.E., C.M. Rienstra, M. Auger, K.V. Lakshmi, and R.G. Griffin, *J. Chem. Phys* 1995, 103 (16), 6951-6958.
72. Fung, B.M., A.K. Khitrin, and K. Ermolaev, *J. Magn. Reson.* 2000, 142 (1), 97-101.
73. Weingarth, M., P. Tekely, and G. Bodenhausen, *Chem. Phys. Lett.* 2008, 466 (4–6), 247-251.
74. Ramachandran, R., V.S. Bajaj, and R.G. Griffin, *J. Chem. Phys.* 2005, 122 (16), 164503.
75. Lee, M. and W.I. Goldburg, *Physical Review* 1965, 140 (4A), A1261-A1271.
76. Bielecki, A., A.C. Kolbert, and M.H. Levitt, *Chem. Phys. Lett.* 1989, 155 (4–5), 341-346.
77. Vinogradov, E., P.K. Madhu, and S. Vega, *Chem. Phys. Lett.* 1999, 314 (5–6), 443-450.
78. Halse, M.E. and L. Emsley, *PCCP* 2012, 14 (25), 9121-9130.
79. Bascuñán, J., S. Hahn, D.K. Park, and Y. Iwasa, *IEEE transactions on applied superconductivity : a publication of the IEEE Superconductivity Committee* 2011, 21 (3 Pt 2), 2092-2095.
80. Van Sciver, S.W., J.R. Miller, S. Welton, H.J. Schneider-Muntau, and G.E. Mcintosh, Cryogenic System for the 45 Tesla Hybrid Magnet, in *Adv. Cryog. Eng.*, P. Kittel, Editor. 1994, Springer US. p. 375-380.
81. Grant, C.V., C.H. Wu, and S.J. Opella, *J. Magn. Reson.* 2010, 204 (2), 180-188.

82. Franks, W.T., B.-J. Van Rossum, B. Bardiaux, E. Ravera, G. Parigi, C. Luchinat, and H. Oschkinat, Microcrystalline Proteins – An Ideal Benchmark for Methodology Development, in *NMR of Biomolecules*. 2012, Wiley-VCH Verlag GmbH & Co. KGaA. p. 376-392.
83. Zech, S.G., A.J. Wand, and A.E. Mcdermott, *J. Am. Chem. Soc.* 2005, 127 (24), 8618-8626.
84. Bertini, I., C. Luchinat, G. Parigi, E. Ravera, B. Reif, and P. Turano, *Proc. Natl. Acad. Sci. U.S.A.* 2011, 108 (26), 10396-10399.
85. Polenova, T., *Nat Chem* 2011, 3 (10), 759-760.
86. Lamley, J.M., D. Iuga, C. Öster, H.-J. Sass, M. Rogowski, A. Oss, J. Past, A. Reinhold, S. Grzesiek, A. Samoson, and J.R. Lewandowski, *J. Am. Chem. Soc.* 2014, 136 (48), 16800-16806.
87. Ferella, L., C. Luchinat, E. Ravera, and A. Rosato, *J. Biomol. NMR* 2013, 57 (4), 319-326.
88. Wickramasinghe, N.P., S. Parthasarathy, C.R. Jones, C. Bhardwaj, F. Long, M. Kotecha, S. Mehboob, L.W.M. Fung, J. Past, A. Samoson, and Y. Ishii, *Nat. Methods* 2009, 6 (3), 215-218.
89. Yamamoto, K., M.A. Caporini, S. Im, L. Waskell, and A. Ramamoorthy, *J. Magn. Reson.* 2013, 237, 175-181.
90. Kotecha, M., N.P. Wickramasinghe, and Y. Ishii, *Magn. Reson. Chem.* 2007, 45 (SUPPL.), S221-S230.
91. Weingarth, M., G. Bodenhausen, and P. Tekely, *J. Magn. Reson.* 2009, 199 (2), 238-41.
92. Lange, A., I. Scholz, T. Manolikas, M. Ernst, and B.H. Meier, *Chem. Phys. Lett.* 2009, 468 (1–3), 100-105.
93. Demers, J.-P., V. Vijayan, S. Becker, and A. Lange, *J. Magn. Reson.* 2010, 205 (2), 216-223.
94. Barbet-Massin, E., A.J. Pell, J.S. Retel, L.B. Andreas, K. Jaudzems, W.T. Franks, A.J. Nieuwkoop, M. Hiller, V. Higman, P. Guerry, A. Bertarello, M.J. Knight, M. Felletti, T. Le Marchand, S. Kotelovica, I. Akopjana, K. Tars, M. Stoppini, V. Bellotti, M. Bolognesi, S. Ricagno, J.J. Chou, R.G. Griffin, H. Oschkinat, A. Lesage, L. Emsley, T. Herrmann, and G. Pintacuda, *J. Am. Chem. Soc.* 2014, 136 (35), 12489-12497.
95. Chevelkov, V., B.J. Van Rossum, F. Castellani, K. Rehbein, A. Diehl, M. Hohwy, S. Steuernagel, F. Engelke, H. Oschkinat, and B. Reif, *J. Am. Chem. Soc.* 2003, 125 (26), 7788-7789.
96. Knight, M.J., A.L. Webber, A.J. Pell, P. Guerry, E. Barbet-Massin, I. Bertini, I.C. Felli, L. Gonnelli, R. Pierattelli, L. Emsley, A. Lesage, T. Herrmann, and G. Pintacuda, *Angew. Chem. Int. Ed.* 2011, 50 (49), 11697-11701.
97. Barbet-Massin, E., M. Felletti, R. Schneider, S. Jehle, G. Communie, N. Martinez, Malene r. Jensen, Rob w.H. Ruigrok, L. Emsley, A. Lesage, M. Blackledge, and G. Pintacuda, *Biophys. J.* 107 (4), 941-946.
98. Reif, B., Deuterated Peptides and Proteins: Structure and Dynamics Studies by MAS Solid-state NMR, in *eMagRes*. 2007, John Wiley & Sons, Ltd.
99. Linser, R., M. Dasari, M. Hiller, V. Higman, U. Fink, J.-M. Lopez Del Amo, S. Markovic, L. Handel, B. Kessler, P. Schmieder, D. Oesterhelt, H. Oschkinat, and B. Reif, *Angew. Chem. Int. Ed.* 2011, 50 (19), 4508-4512.
100. Mroue, K.H., Y. Nishiyama, M. Kumar Pandey, B. Gong, E. Mcnerny, D.H. Kohn, M.D. Morris, and A. Ramamoorthy, *Scientific Reports* 2015, 5, 11991.
101. Overhauser, A.W., *Physical Review* 1953, 89 (4), 689-700.

102. Carver, T.R. and C.P. Slichter, *Physical Review* 1953, 92 (1), 212-213.
103. Ardenkjær-Larsen, J.H., B. Fridlund, A. Gram, G. Hansson, L. Hansson, M.H. Lerche, R. Servin, M. Thaning, and K. Golman, *Proc. Natl. Acad. Sci. U. S. A.* 2003, 100 (18), 10158-10163.
104. Miéville, S. Jannin, L. Helm, and G. Bodenhausen, *CHIMIA International Journal for Chemistry* 2011, 65 (4), 260-263.
105. Dutta, P., G. Martinez, and R. Gillies, *Biophys Rev* 2013, 5 (3), 271-281.
106. Meier, S., M. Karlsson, P.R. Jensen, M.H. Lerche, and J.O. Duus, *Molecular BioSystems* 2011, 7 (10), 2834-2836.
107. Ni, Q.Z., E. Daviso, T.V. Can, E. Markhasin, S.K. Jawla, T.M. Swager, R.J. Temkin, J. Herzfeld, and R.G. Griffin, *Acc. Chem. Res.* 2013, 46 (9), 1933-1941.
108. Smith, A.N., M.A. Caporini, G.E. Fanucci, and J.R. Long, *Angew. Chem. Int. Ed.* 2015, 54 (5), 1542-1546.
109. Yamamoto, K., M.A. Caporini, S.-C. Im, L. Waskell, and A. Ramamoorthy, *Biochimica et Biophysica Acta (BBA) - Biomembranes* 2015, 1848 (1, Part B), 342-349.
110. Rosay, M., A.-C. Zeri, N.S. Astrof, S.J. Opella, J. Herzfeld, and R.G. Griffin, *J. Am. Chem. Soc.* 2001, 123 (5), 1010-1011.
111. Takahashi, H., I. Ayala, M. Bardet, G. De Paëpe, J.-P. Simorre, and S. Hediger, *J. Am. Chem. Soc.* 2013, 135 (13), 5105-5110.
112. Renault, M., S. Pawsey, M.P. Bos, E.J. Koers, D. Nand, R. Tommassen-Van Boxtel, M. Rosay, J. Tommassen, W.E. Maas, and M. Baldus, *Angew. Chem. Int. Ed.* 2012, 51 (12), 2998-3001.
113. Lesage, A., M. Lelli, D. Gajan, M.A. Caporini, V. Vitzthum, P. Miéville, J. Alauzun, A. Roussey, C. Thieuleux, A. Mehdi, G. Bodenhausen, C. Copéret, and L. Emsley, *J. Am. Chem. Soc.* 2010, 132 (44), 15459-15461.
114. Bowers, C.R. and D.P. Weitekamp, *Phys. Rev. Lett.* 1986, 57 (21), 2645-2648.
115. Eisenschmid, T.C., R.U. Kirss, P.P. Deutsch, S.I. Hommeltoft, R. Eisenberg, J. Bargon, R.G. Lawler, and A.L. Balch, *J. Am. Chem. Soc.* 1987, 109 (26), 8089-8091.
116. Bouguet-Bonnet, S., F. Reineri, and D. Canet, *J. Chem. Phys* 2009, 130 (23), 234507.
117. Palaniappan, K.K., R.M. Ramirez, V.S. Bajaj, D.E. Wemmer, A. Pines, and M.B. Francis, *Angew. Chem. Int. Ed.* 2013, 52 (18), 4849-4853.
118. *Nat Chem Biol* 2009, 5 (11), 773-773.
119. Krushelnitsky, A., D. Reichert, and K. Saalwächter, *Acc. Chem. Res.* 2013, 46 (9), 2028-2036.
120. Mollica, L., M. Baias, J.R. Lewandowski, B.J. Wylie, L.J. Sperling, C.M. Rienstra, L. Emsley, and M. Blackledge, *J. Phys. Chem. Lett.* 2012, 3 (23), 3657-3662.
121. Cole, H.B.R. and D.A. Torchia, *Chem. Phys.* 1991, 158 (2–3), 271-281.
122. Williams, J.C. and A.E. Mcdermott, *Biochemistry* 1995, 34 (26), 8309-8319.
123. Agarwal, V., Y. Xue, B. Reif, and N.R. Skrynnikov, *J. Am. Chem. Soc.* 2008, 130 (49), 16611-16621.
124. Lewandowski, J.R., *Acc. Chem. Res.* 2013, 46 (9), 2018-2027.
125. Chevelkov, V., A. Diehl, and B. Reif, *J. Chem. Phys* 2008, 128 (5), 052316.
126. Asami, S., J.R. Porter, O.F. Lange, and B. Reif, *J. Am. Chem. Soc.* 2015, 137 (3), 1094-1100.

127. Lewandowski, J.R., J. Sein, H.J. Sass, S. Grzesiek, M. Blackledge, and L. Emsley, *J. Am. Chem. Soc.* 2010, 132 (24), 8252-8254.
128. Fry, E.A., S. Sengupta, V.C. Phan, S. Kuang, and K.W. Zilm, *J. Am. Chem. Soc.* 2011, 133 (5), 1156-1158.
129. Lesage, A., L. Emsley, F. Penin, and A. Böckmann, *J. Am. Chem. Soc.* 2006, 128 (25), 8246-8255.
130. Giraud, N., J. Sein, G. Pintacuda, A. Böckmann, A. Lesage, M. Blackledge, and L. Emsley, *J. Am. Chem. Soc.* 2006, 128 (38), 12398-12399.
131. Purusottam, R., G. Bodenhausen, and P. Tekely, *J. Biomol. NMR* 2013, 57 (1), 11-19.
132. Overhauser, A.W., *Physical Review* 1953, 92 (2), 411-415.
133. Anderson, W.A. and R. Freeman, *J. Chem. Phys* 1962, 37 (1), 85-103.
134. Neuhaus, D. and M.P. Williamson, The nuclear Overhauser effect in structural and conformational analysis. 2000, New York: John Wiley.
135. Naito, A. and C.A. Mcdowell, *J. Chem. Phys* 1986, 84 (8), 4181-4186.
136. Higgins, J.S., A.H. Hodgson, and R.V. Law, *J. Mol. Struct.* 2002, 602–603, 505-510.
137. Takegoshi, K. and T. Terao, *J. Chem. Phys* 2002, 117 (4), 1700-1707.
138. Katoh, E., K. Takegoshi, and T. Terao, *J. Am. Chem. Soc.* 2004, 126 (11), 3653-3657.

2 Sensitivity enhancement and quantitative 1D & 2D ^{13}C spectra

2.1 Introduction to quantitative solid state NMR

NMR is by definition a quantitative spectroscopic tool because the intensity of a resonance line is directly proportional to the number of resonant nuclei (determined by the difference of spin populations at energy levels). This fact enables, in principle, a precise determination of the amount of molecular structures and, hence, of substances in solids as well as liquids. With the increase of sensitivity due to stronger static magnetic fields, including improved electronics, the detection limits have been pushed down significantly. Apart from NMR, various techniques can be used to provide quantitative analysis of small-molecule organic compounds. The most common is chromatographic separation followed by detection of the analyte based on spectroscopic detection (e.g., UV/Visible, evaporative light scattering, etc.) or spectrometric detection (e.g., mass spectrometry). Quantitative NMR (qNMR) has been shown to be particularly useful in metabolomics [1], drug discovery and analysis [2], and natural product analysis [3]. Analytical methods based on solid-state NMR are also becoming increasingly popular. However, these flourishing activities bring up the issue of how accurately NMR can assess an analyte proportion in a solid sample [4]. In biological solid-state NMR, characterization of protein dynamics by solid-state NMR spectroscopy requires robust and accurate measurement protocols, which is still in developmental stage. The quantitative analysis can reveal vital information of backbone [5, 6] and side chain motion dynamics in solution and in a crystalline state [7, 8]. Earlier studies have shown that methyl dynamics in the solution and solid samples are quantitatively similar [7]. In general, it shows that the entire dynamic network, including side chains motions in the protein hydrophobic core and backbone motions, are similar. Hence, internal protein dynamics can be characterized by combined interpretation of solid and solution-state NMR data, eventually leading to a meticulous characterization of internal protein dynamics on a wide range of time scales. Besides quantitative analysis, recording sensitive and quantitative spectra of

low-gamma nuclei such as ^{13}C constitutes also a long-standing challenge for solid-state NMR spectroscopy.

Most solid-state ^{13}C NMR spectra are inherently non-quantitative since cross-polarization (CP) from protons to carbons is not uniform, and single-pulse experiments are not quantitative when the delays between successive acquisitions are too short to allow a uniform recovery of the longitudinal ^{13}C magnetization of all sites. The most pronounced distortions of intensities in CP spectra are observed between proton-carrying carbons on the one hand, and carbonyl, carboxyl, or quaternary carbons on the other, since the latters' magnetization suffers from a slow build-up during cross polarization. Additional deviations from quantitative peak intensities can also arise in CP spectra because local variations in internal mobility lead to variations in CP efficiency and/or rotating-frame relaxation rates $R_{1\rho}$.

Phase Alternated Recoupling Irradiation Scheme (PARIS)

Two-dimensional ^{13}C-^{13}C correlation experiments are widely employed in structure determination of protein assemblies using solid-state nuclear magnetic resonance. PARIS [9, 10] and PARIS-xy [11] schemes permit one to reach similar peak amplitudes (± 10%) for chemically different sites on time scales as short as a few hundreds of milliseconds. Requirement for recording quasi-quantitative single pulse or CP spectra of labeled amino acids has been discussed recently [12]. PARIS irradiation scheme has been employed hitherto to record sensitive 2D correlation spectra of microcrystalline proteins [10, 13], amyloid fibrils [14] and mixtures of crystallographic forms [15] and to restore the symmetry in 2D homonuclear correlation experiments of simple amino acids [12]. Fig. 2 shows the variants schemes of PARIS irradiation suited for different static fields and effective recoupling of different ^{13}C spin pairs [16].

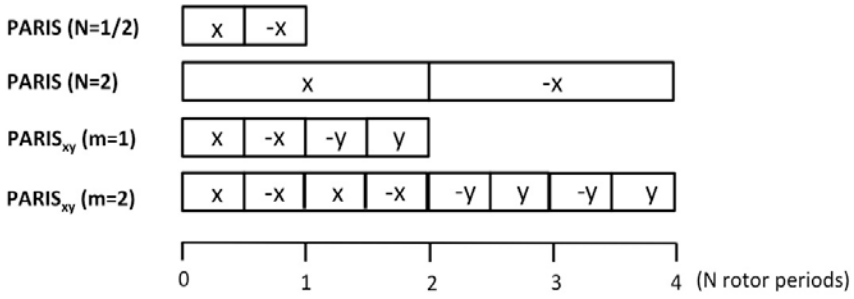

Figure 2: Different versions of Phase Alternated Recoupling Irradiation Scheme (PARIS).

For performing 2D ^{13}C-^{13}C correlation experiments at moderately high magnetic fields, the schemes with half-rotor-synchronised pulses i.e. PARIS (N=1/2), PARIS-xy (m = 1)(N = 1/2) and PARIS-xy (m = 2)(N = 1/2) should be preferred. Magnetisation transfer efficiency is optimal at low r.f. amplitudes at $\nu_{1H} \approx 1/4\ \nu_r$ ad hence, should be applied. For spectrally apart and far-apart ^{13}C nuclei, either schemes containing two-rotor-synchronised pulses (i.e. PARIS (N = 2) and PARIS-xy (m = 1)(N = 2) or PARIS-xy (m = 1)(N = 1/2) should be used. RF amplitude as low as 1/2 ν_r is sufficient for efficient magnetisation transfer. PARIS-xy (m=1)(N=1/2) scheme when employed using an r.f. amplitude of nearly half the MAS frequency (ν_r) is mostly efficient in transferring magnetisation among all kind of ^{13}C nuclei. Hence, this should be the sequence of choice for performing 2D ^{13}C-^{13}C correlation experiments at moderately high magnetic fields and MAS frequencies. For experiments at high static magnetic fields and for spectrally close ^{13}C nuclei, half-rotor-synchronised pulses i.e. PARIS (N = 1/2), PARIS-xy (m = 1)(N = 2) should be used and preferably with low r.f. amplitudes ($\nu_{1H} \approx 1/2\ \nu_r$) for efficient magnetization transfer. For spectrally apart and far-apart ^{13}C nuclei, recoupling schemes containing two-rotor-synchronised pulses i.e. PARIS (N = 2) and PARIS-xy (m = 1)(N = 2) should be used with preferably high r.f. amplitudes ($\nu_{1H} \approx \nu_r$).

In this chapter, it is shown that by applying low-power PARIS or PARIS-xy irradiation, it is possible to record quantitative one- and two-dimensional ^{13}C spectra of microcrystalline proteins after. These spectra not only benefit from uniform sensitivity enhancement due to spin exchange breaking T_1 (^{13}C) constrains but also from the existence of heteronuclear Overhauser effect.

When recording quantitative spectra of labelled microcrystalline proteins, it was realized that one also takes advantage, apart from efficient equilibration of magnetization and accelerated longitudinal recovery, of the simultaneous presence of

heteronuclear Overhauser enhancement induced by low-power PARIS irradiation which has several advantages as compared with DARR irradiation. PARIS pulse scheme allows to achieve efficient dipolar recoupling and to induce uniform exchange of magnetization with low *rf* field amplitudes over a very broad range of spinning frequencies and static fields [9-11]. It spares the experimentalist of the rigorous optimization and are immune to dipolar truncation [14].

Another added advantage is that it is not necessary to fulfill any rotary [17, 18] or rotational resonance [19] for transferring magnetization between spectrally close or distant carbons. The efficiency of PARIS recoupling schemes, in contrast to DARR, does not depend critically on the *rf* amplitude [10] which permits to achieve the magnetization transfer with low-power rf irradiation even at high spinning frequencies. Unlike in DARR, which uses continuous-wave irradiation, both PARIS and PARIS-xy schemes are largely immune to the inherent inhomogeneity of the *rf* field, so that the full sample volume effectively contributes to the signal [9]. So, in overall when recording uniformly enhanced spectra of labelled microcrystalline proteins, the whole set of PARIS features permits to use much lower *rf* amplitudes and shorter irradiation durations as compared with DARR irradiation.

2.2 Results and discussion

2.2.1 Overcoming the T_1 (^{13}C) constraints

To record quantitative solid-state NMR spectra of low-gamma nuclei with integrated signal intensities that are proportional to the number of nuclei, one needs to equalize magnetization between differentially relaxing sites. This is illustrated in Fig. 2.1 by comparing the intensities of resonance signals from different carbons of L-histidine recorded without and with PARIS irradiation applied prior to detection. The latter case leads to a transfer of magnetization from more rapidly relaxing aliphatic carbons to slowly recovering carboxyl and aromatic carbon.

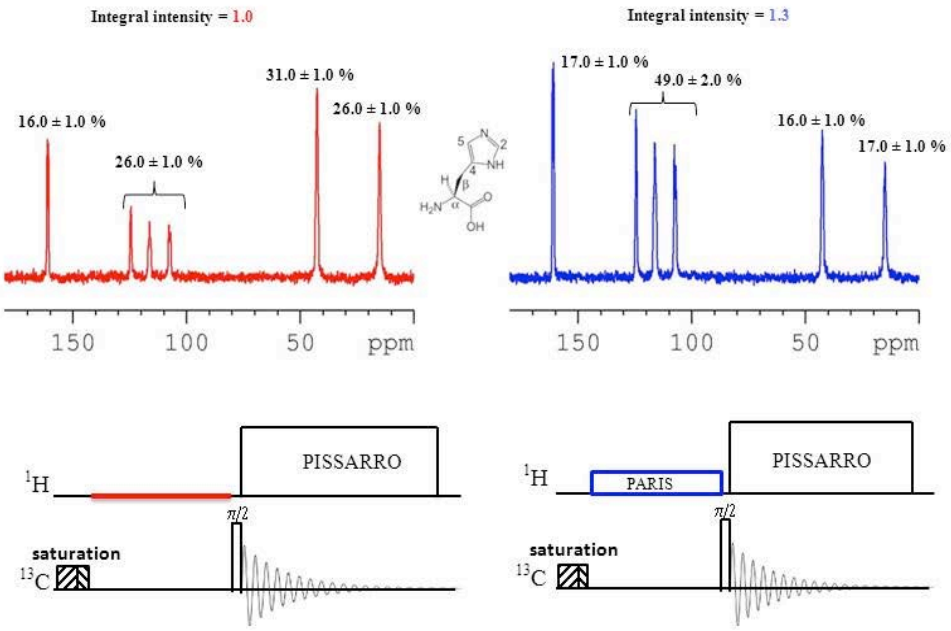

Figure 2.1: (Top) ^{13}C spectra of uniformly labeled L-histidine: single-pulse reference spectrum (red) and quantitative spectrum with enhanced intensity (blue). The numbers give relative integrated intensities of individual resonances or regions. Both spectra were recorded in a magnetic field of 9.4 T (400 MHz for ^{1}H) at a spinning frequency of 23 kHz. (Below) The reference spectrum was obtained after a delay of 3 s; the quantitative spectrum was recorded using PARIS (N = 2) irradiation with a proton *rf* amplitude of 15 kHz during 3.0 s. The proton decoupling field amplitude was 96 kHz using the PISSARRO sequence.

At the same time, efficient spin exchange in the presence of PARIS recoupling accelerates recovery of the latter carbons, which is illustrated in Fig.2.1.1.

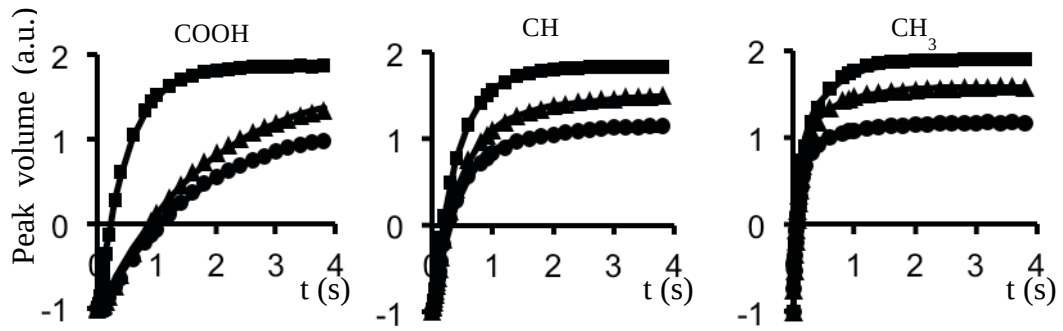

Figure 2.1.1: Inversion recovery of longitudinal ^{13}C magnetization for different carbons of L-alanine in standard T_1 measurements (circles) and when using CW (triangles) or PARIS (squares) irradiation with an rf amplitude of 10 kHz. The spinning frequency was 23 kHz. Note accelerated recovery of

longitudinal magnetization for carboxyl carbons under PARIS irradiation (T_1= 0.55 s) as compared with standard experiment without any irradiation (T_1= 1.87 s)

For L-histidine, this dramatically reduces the time required to record quantitative spectra. Under the experimental conditions used to record the spectra in Fig. 2.1, a recovery delay t_{rd} = 3 s suffices, while roughly t_{rd} = 200 s is required to record quantitative spectra in the absence of PARIS irradiation. Similar observations that the T_1 constraints can be overcome have been reported recently for L-tyrosine [20] and L-histidine [21].

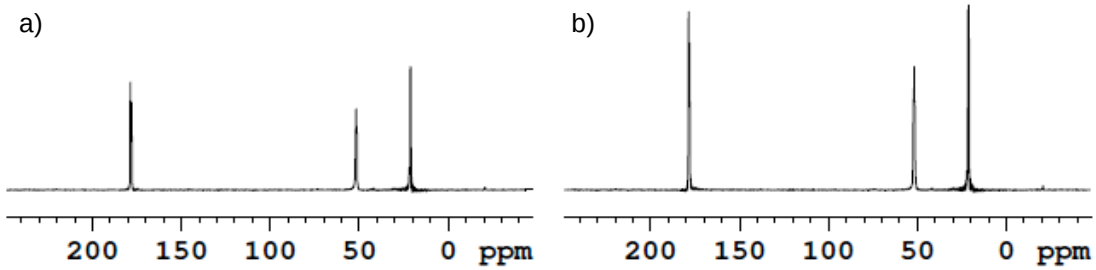

Figure 2.1.2: (a) Single pulse ^{13}C spectrum of L-alanine recorded after a relaxation delay of 30 s or (b) using PARIS irradiation during 3 s preceding the acquisition. Other parameters as in Fig. 2.1.1.

Somewhat unexpectedly, in contrast to L-histidine and L-arginine, while recording quantitative ^{13}C spectra of microcrystalline proteins employing PARIS irradiation, a uniform enhancement of all peaks was observed, as compared with single-pulse spectra obtained after complete relaxation of the longitudinal magnetization. This stimulated the investigation of the role of heteronuclear Overhauser enhancements that could be induced by cross-relaxation in these systems.

Studies on microcrystalline proteins

The initial impulse to use microcrystalline preparations of proteins in the development of a structure determination concept in solid-state NMR stemmed from the requirement to obtain high-resolution spectra, facilitating spectral analysis. Inhomogeneous broadening is the most common source of broadening for biological samples and special care needs to be taken to ensure structural homogeneity over the whole sample. Fortunately, sample inhomogeneity can be addressed through laboratory methods. A proven way to generate samples that yield high-resolution

solid-state NMR spectra is to generate three- or two-dimensional crystals of either soluble or membrane proteins respectively [22].

Initial studies found crystallization conditions that produced high-resolution spectra for the α-spectrin SH3 domain [23, 24], bovine pancreatic trypsin inhibitor (BPTI) [25], ubiquitin [26, 27], and the immunoglobulin- binding domain of protein G (GB1) [28]. Another benefit of using crystalline protein preparation is that the crystal quality does not need to be as high as those used for single-crystal X-ray studies. Crystalline preparations are used for methodology development since the finely resolved spectra readily facilitate resonance assignments and the extraction of structural parameters. It gives access into features of protein structures that are difficult to obtain by conventional X-ray crystallography, such as information about hydrogen atoms and dynamics in the crystalline state.

2.2.2 Revealing the sources of the heteronuclear Overhauser enhancement

To confirm the presence of heteronuclear Overhauser effects and identify the sources of the intensity enhancement, while avoiding the equilibration of magnetization, transient Overhauser experiments were performed [29]. This allows identifying the role of cross-relaxation in a straightforward manner, and clearly reveals the mechanism underlying the intensity enhancement when comparing spectra recorded with and without a π pulse [30, 31].

As shown in Fig. 2.2 for the microcrystalline proteins GB1 and ubiquitin, significant enhancements of some signals are observed after cross-relaxation delays t_{cr} of a few hundreds of milliseconds.

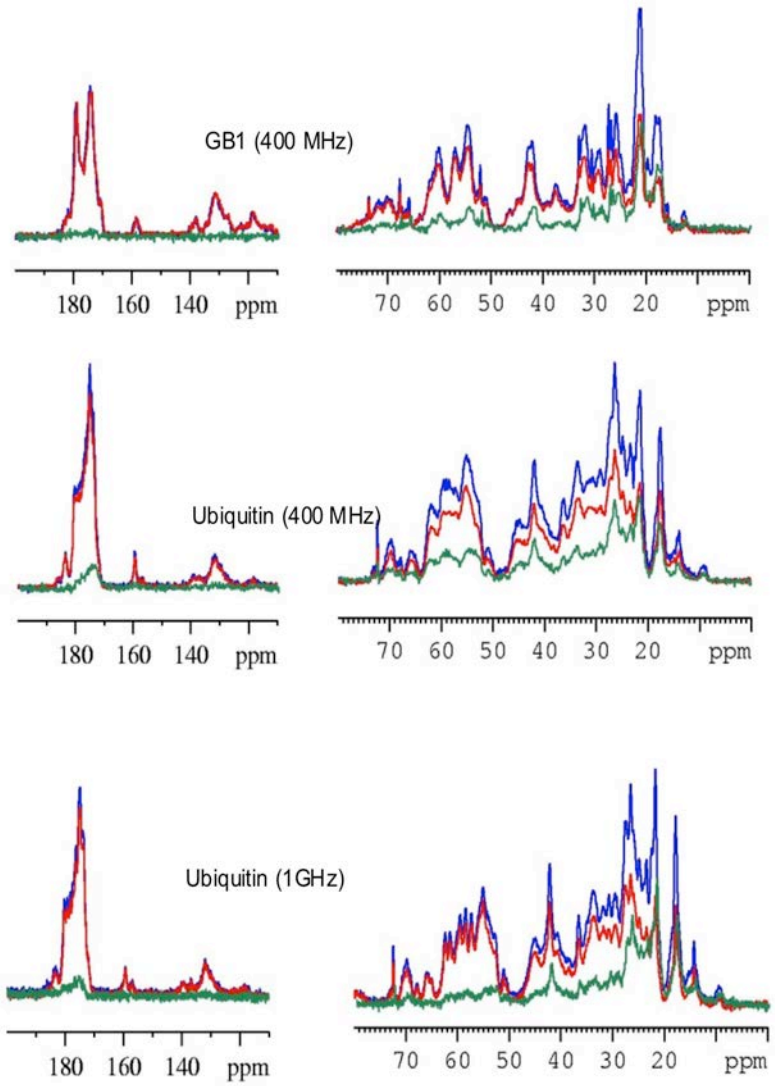

Figure 2.2: Single-pulse reference spectra (red), transient NOE spectra (blue), and difference spectra (green) of ubiquitin and GB, recorded in magnetic fields of 9.4 T or 23.5 T (400 MHz or 1 GHz for protons) with spinning frequencies of 22.5 and 24 kHz respectively and a recycle delay of 10 s.
The transient NOE spectra were recorded with a cross-relaxation delay t_{cr} = 300 ms for GB1 and 500 ms for Ubiquitin (see pulse sequence in Fig. 2.3). The ^{1}H and ^{13}C *rf* amplitudes were 167 kHz and 71 kHz, respectively. The ^{1}H decoupling field was 96 kHz using the PISSARRO sequence.

Such enhancements are not only restricted to fast rotating methyl groups that are expected to constitute the main reservoir of the heteronuclear Overhauser enhancement [32], but also for their nearest neighbours, and even for carbons that are spatially distant from the methyl groups. This suggests that the resonance signals stemming from carbons located in the most mobile parts of the protein, especially in side-chains that are inherently mobile, also benefit to certain degree from such enhancements.

Fig. 2.3 shows that different ^{13}C sites feature specific build-up behaviours of the magnetization as a function of the cross-relaxation delay t_{cr}. A notable thing about each individual ^{13}C site is that, it strictly obeys the Solomon equations. This opens up a way to site-specific quantitative NOE measurements that will be explored further in chapter 3.

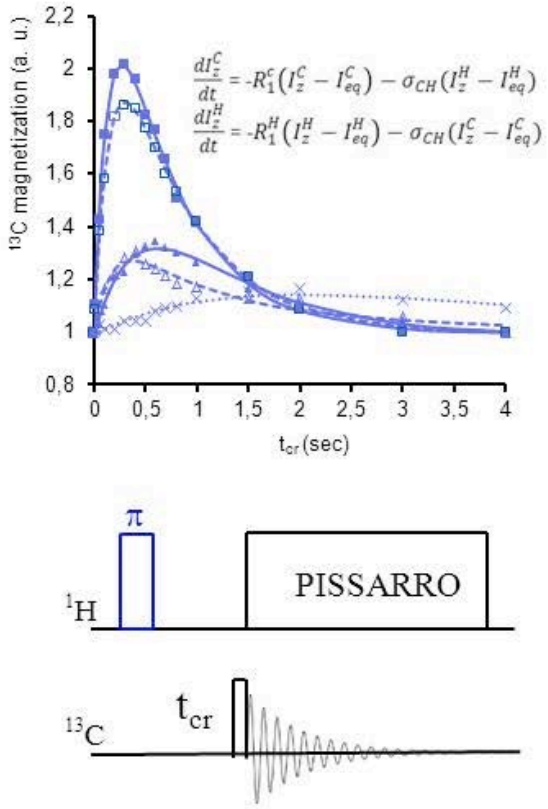

Figure 2.3: (Top) Build-up curves of the magnetization as a function of the cross relaxation delay t_{cr} for isotropic ^{13}C signals of GB1 at 17.8 ppm (filled squares), 21.1 ppm (open squares), 42.2 ppm (open triangles), 54.4 ppm (filled triangles) and 174.0 ppm (crosses). The spectra were recorded in a magnetic field of 9.4 T with a spinning frequency of 24 kHz and a recycle delay of 10 s. The solid, dashed and dotted lines represent fits to the Solomon equations. To fit the build-up of the peak at 42.2 ppm (open triangles), the presence of two populations of CH_2 with different relaxation parameters had to be postulated. (bottom) Pulse sequence to determine the build-up of transient heteronuclear Overhauser effects as a function of the cross relaxation delay t_{cr}.

Corroborative evidence that mobile side-chains can also constitute a source of heteronuclear Overhauser enhancements is provided by the transient ^{15}N spectra shown in Fig. 2.4.

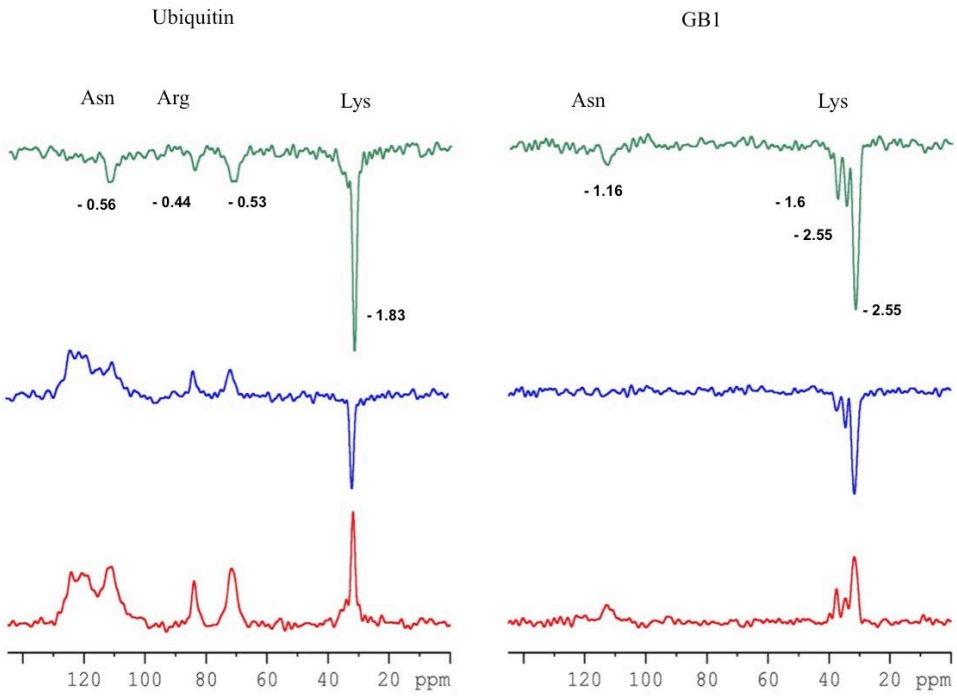

Figure 2.4: Single-pulse ^{15}N reference spectra (bottom), transient NOE spectra (middle), and difference spectra (top) of Ubiquitin (left) and GB1 (right.) All spectra were recorded in a magnetic field of 9.4 T (400 MHz for ^{1}H) with a spinning frequency of 22.5 kHz. In both cases the transient NOE spectra were recorded with a cross-relaxation delay t_{cr} = 500 ms. For Ubiquitin a recycle delay of 4 s was used, while for GB1 the saturation pulses were applied to the ^{15}N spins before the 180° proton pulse. The numbers give the NOE enhancements factors (η) for individual resonances. The three resonance lines of lysine residues in GB1, visible at the isotropic chemical shifts 31.7, 34.7, and 37.7 ppm, most probably result from the presence of different polymorphs and/or crystallographically different forms.

The negative enhancements were mostly pronounced for lysine residues, as has been observed in microcrystalline Crh protein [33]. Also, the spin diffusion mediated fast chemical exchange involving mobile water protons or their direct interaction with a protein, didn't lead to any significant enhancement, at least on a time scale up to a few seconds.

2.2.3 Promoting uniform enhancements with low-power PARIS irradiation

In analogy to solution-state NMR, as illustrated in Fig. 2.5 for L-threonine, significant variations of NOE enhancement factors from one carbon site to another constitute a major impediment to a quantitative utilisation of ^{13}C peak intensities in transient NOE spectra. To record quantitative spectra, the magnetization needs to be equilibrated. . As shown in Fig. 2.5, this can be accomplished by PARIS irradiation that simultaneously promotes heteronuclear Overhauser enhancements and the equilibration of magnetization. Utilizing this dual benefit from PARIS irradiation, the spectrum with uniformly enhanced peak intensities that are proportional to the number of nuclei was obtained (fig. 2.5(right)).

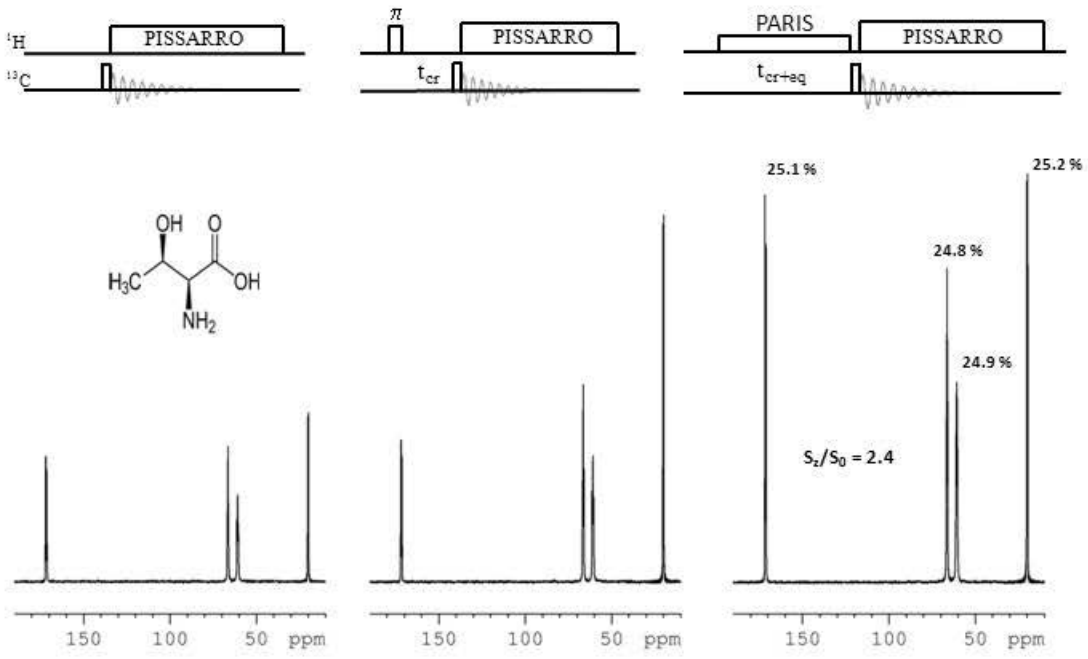

Figure 2.5: (bottom) Single-pulse ^{13}C reference spectrum (left), transient NOE spectrum (middle) and quantitative spectrum with enhanced intensity (right) of uniformly labeled L-threonine. The numbers give relative integrated intensities (in %) of the individual resonances. All spectra were recorded in a magnetic field of 9.4 T (400 MHz for ^{1}H) at a spinning frequency of 20 kHz. (top) The single-pulse reference spectrum was recorded with a recovery delay t_{rd} = 4 s, the transient NOE spectrum with t_{rd} = 3.4 s and t_{cr} = 600 ms, the quantitative spectrum with t_{rd} = 3 s and PARIS-xy (m = 1) irradiation with a proton *rf* amplitude of 15 kHz during 1 s.

Fig. 2.6 shows ^{13}C spectra of the microcrystalline protein GB1 recorded without and with PARIS irradiation prior to signal detection. The observed differences

demonstrate that low-power PARIS irradiation indeed allows one to record quantitative spectra of microcrystalline proteins with the combined benefits of enhanced and uniformly equilibrated magnetization.

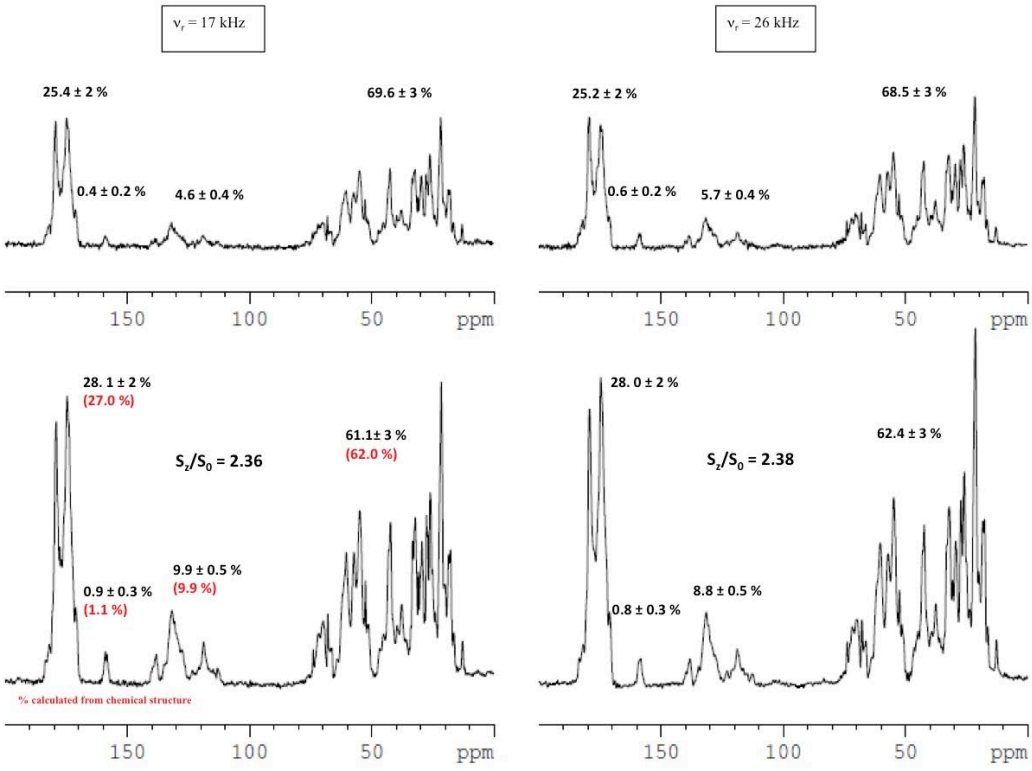

Figure 2.6: Single-pulse ^{13}C reference spectra (top) and uniformly enhanced quantitative spectra (bottom) of GB1 recorded at spinning frequencies ν_{rot} = 17 and 26 kHz using PARIS-xy (n = 1) irradiation with a proton *rf* amplitude of 12 kHz during 2.3 and 3.0 s, respectively. The reference spectra were recorded with recycle delay t_{rd} = 7.0 s while the corresponding uniformly enhanced spectra were recorded with t_{rd} = 4.7 s and 4.0 s, respectively. The numbers give relative integrated intensities for different spectral regions. The overall intensity gain is $S_z/S_0 = 1 + \eta$, where η represents the nuclear Overhauser enhancement factor (referring to the S_0 value of the aliphatic carbons.). The proton decoupling field amplitude was 96 kHz using the PISSARRO sequence.

Quantitative spectra with enhanced intensity can be also recorded, as shown in Fig. 2.7 for microcrystalline Ubiquitin, in a very high static field of 23.5 T using the same duration of low-power PARIS irradiation. It is also worth recalling that the efficiency

of PARIS equilibration does not depend critically on the *rf* amplitude, which need not be matched with the spinning frequency.

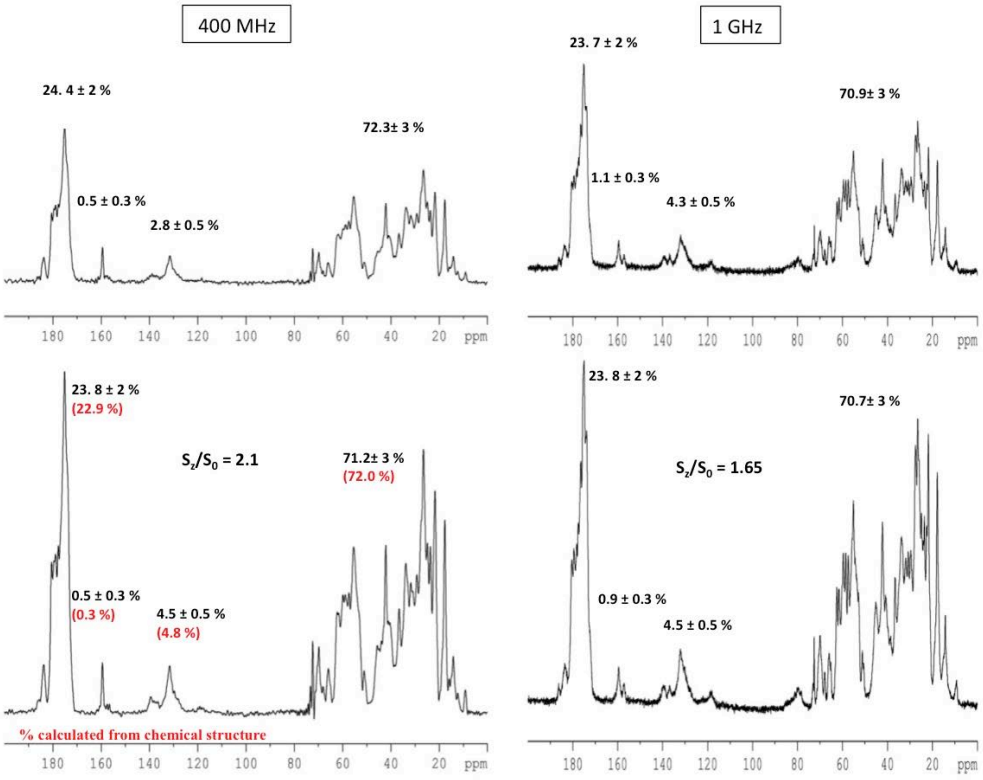

Figure 2.7: Single-pulse ^{13}C reference spectra (top) and uniformly enhanced spectra (bottom) of Ubiquitin recorded at a spinning frequency of 24 kHz at two different static fields. The reference spectra were recorded with recycle delays t_{rd} = 6 s (at 400 MHz) and 13 s (at 1000 MHz) while the corresponding uniformly enhanced spectra were recorded with t_{rd} = 3 and 10 s using PARIS-xy (n = 1) or PARIS (N=1/2) irradiation during 3 s with proton *rf* amplitudes of 15 and 20 kHz applied prior to a reading pulse. The numbers give the experimental (in black) and theoretical (in red) values of the integrated intensities for different spectral regions. The overall intensity gain S_z/S_0, refers to the S_0 value of the aliphatic carbons. The proton decoupling field was 96 kHz using PISSARRO.

As shown in Fig. 2.8, this allows one to record quantitative spectra of hydrated microcrystalline proteins with very modest *rf* fields, while DARR would require at the same spinning frequency roughly seven times higher *rf* power to fulfill the rotary resonance condition.

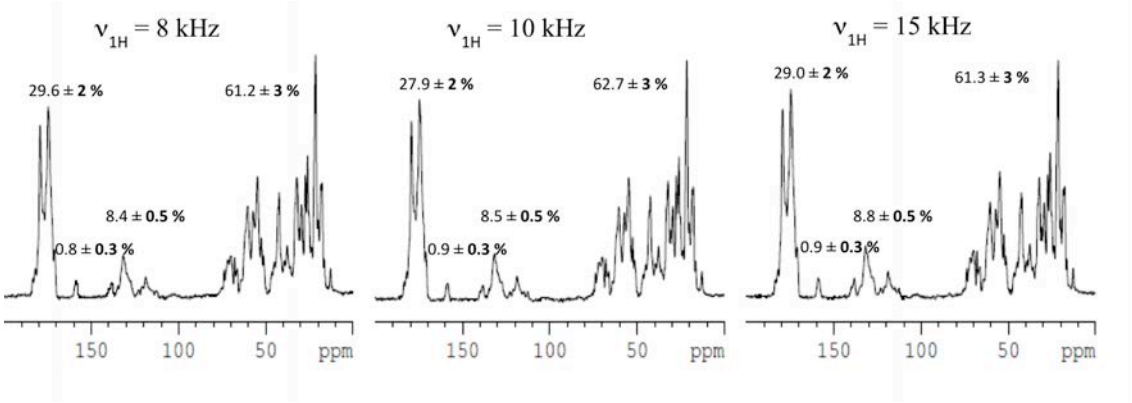

Figure 2.8: Quantitative spectra of GB1 recorded at a spinning frequency of 26 kHz using PARIS-xy (*n* = 1) irradiation during 3 s with proton *rf* amplitudes ν_{1H} = 8, 10 and 15 kHz applied prior to a reading pulse. The numbers give relative integrated intensities for different spectral regions.

Finally, somewhat better enhancements can be achieved by equilibrating the magnetization prepared by cross-polarization. However, as shown in Fig. 2.9, the observed enhancements appear to be modest and are not really worth the effort required to optimize cross-polarization in microcrystalline proteins. It is also worth to remind that due to a low proton/carbon ratio N_I/N_S in a uniformly ^{13}C-labeled protein, the theoretical maximum CP gain is reduced to about 2.4 from a factor of 4 in an ideal case [32]. In practice the CP enhancement in uniformly labeled microcrystalline proteins is found between 1.0 and 2.0. Consequently, and as shown in Fig. 2.9, the heteronuclear Overhauser enhancement will be usually higher than with CP.

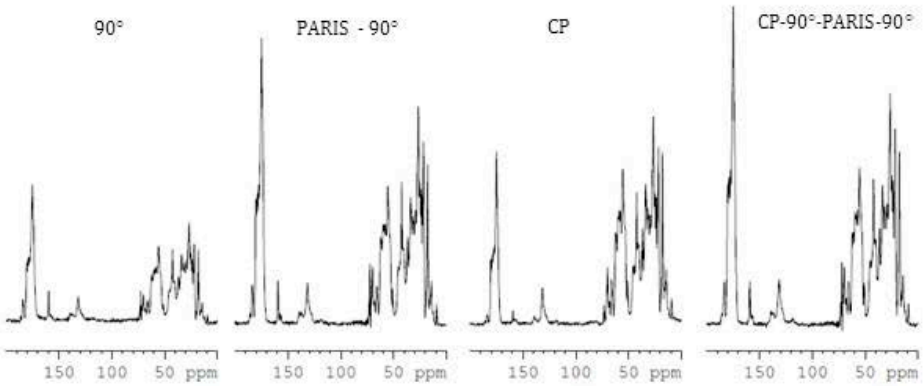

Figure 2.9: (From left to right) Single-pulse ^{13}C reference spectrum, uniformly enhanced spectrum, standard cross-polarization (CP) spectrum (using optimal contact time CT = 1.5 ms for aliphatic carbons) and CP-PARIS spectrum of Ubiquitin recorded at 400 MHz. The uniformly enhanced spectra were recorded using PARIS-xy (*n* = 1) irradiation with a proton *rf* amplitude of 15 kHz applied during 3.0 s prior to a reading pulse. All spectra were recorded at a 24 kHz spinning frequency with the same number of scans and recovery delays after the initial saturation pulses.

As mentioned earlier, the equilibration of magnetization using PARIS irradiation also removes the commonly encountered asymmetries in ^{13}C-^{13}C correlation spectra [12]. Such asymmetries arise from a non-uniform preparation of the magnetization when the initial cross-polarization is used or when the delay between successive acquisitions in single-pulse experiments is too short to allow a uniform recovery of the longitudinal magnetization from all sites. This is illustrated in Figs. 2.10 and 2.11 where, in the absence of PARIS irradiation, the asymmetry is especially pronounced for GB1 because of the slow recovery of the longitudinal magnetization of the carboxyl carbons. Importantly, the rate of recovery is significantly enhanced by PARIS irradiation promoting efficient spin exchange.

As have been previously demonstrated, restoring the symmetry of 2D spectra is crucial to extract reliable rate constants that allow one to deduce internuclear distances and hence structural information [12]. Equally importantly, when recording symmetric 2D correlation spectra as shown in Figs. 2.10 and 2.11, one simultaneously benefits from heteronuclear Overhauser effects, leading *in fine* to uniformly enhanced intensities of all diagonal and cross-peaks. As shown in Fig. 2.11, the efficient restoration of symmetry over the whole spectral range along with a uniform enhancement of intensities was achieved at very high static fields despite a modest *rf* amplitude. However, to record quantitative spectra at very high spinning frequencies it will be necessary to use longer irradiation periods. Heating by *rf* irradiation could be limited by using so-called E-free probes. Low-power PARIS irradiation also significantly enhances and equilibrates the magnetization of ^{13}C nuclei in heterogenous biological samples like membrane proteins embedded in proteoliposomes, which is presented later.

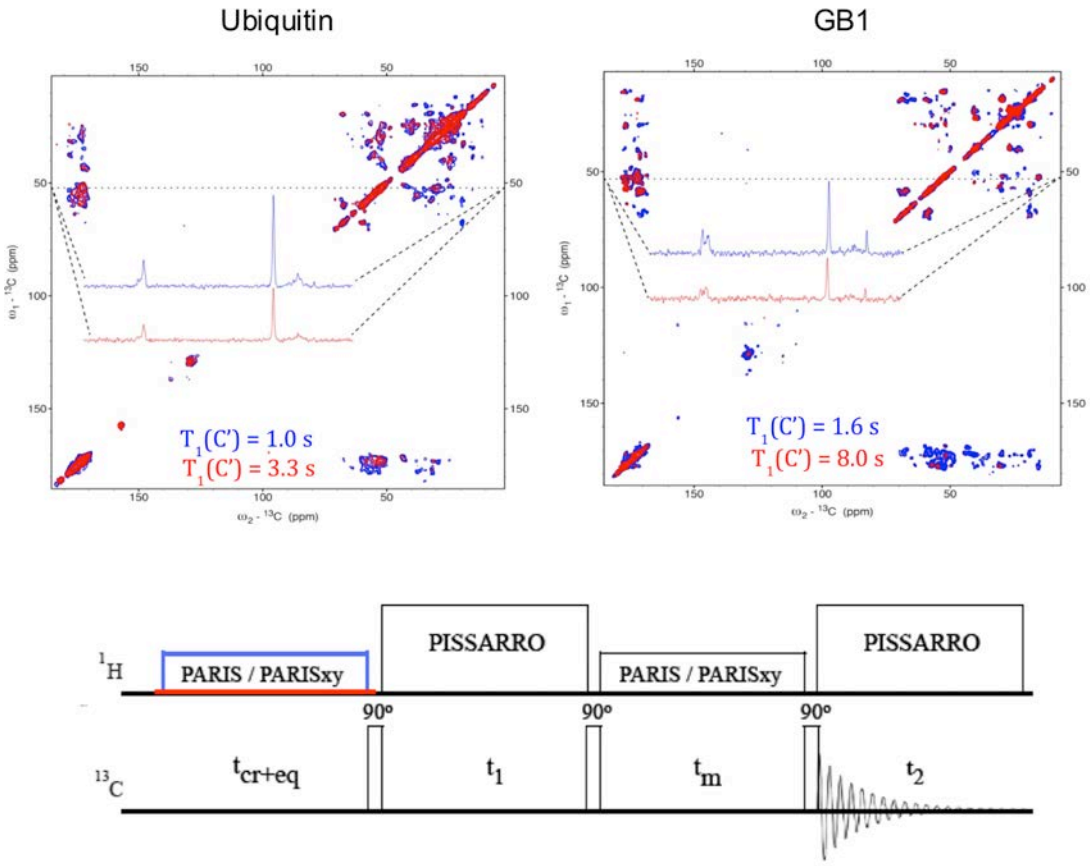

Figure 2.10 : (top) 2D ^{13}C-^{13}C correlation spectra of Ubiquitin (left) and GB1 (right) recorded at 400 MHz. Each figure shows two overlaid spectra recorded either without (red) or with (blue) PARIS-xy (m = 1) irradiation during 1.7 s with an *rf* amplitude ν_{1H} = 15 kHz and the recycle times 6 and 4.3 s, respectively. Both spectra were plotted with the same contour levels. During the mixing time (t_m = 42 and 100 ms for ubiquitin and GB1, respectively), PARIS-xy (m = 1) was applied with the same *rf* amplitude. The 1.3 mm rotors were spun at 24 and 22.5 kHz for ubiquitin and GB1. The proton-decoupling field was 96 kHz with PISSARRO. (bottom) The pulse sequences schemes used to record the 2D spectra.

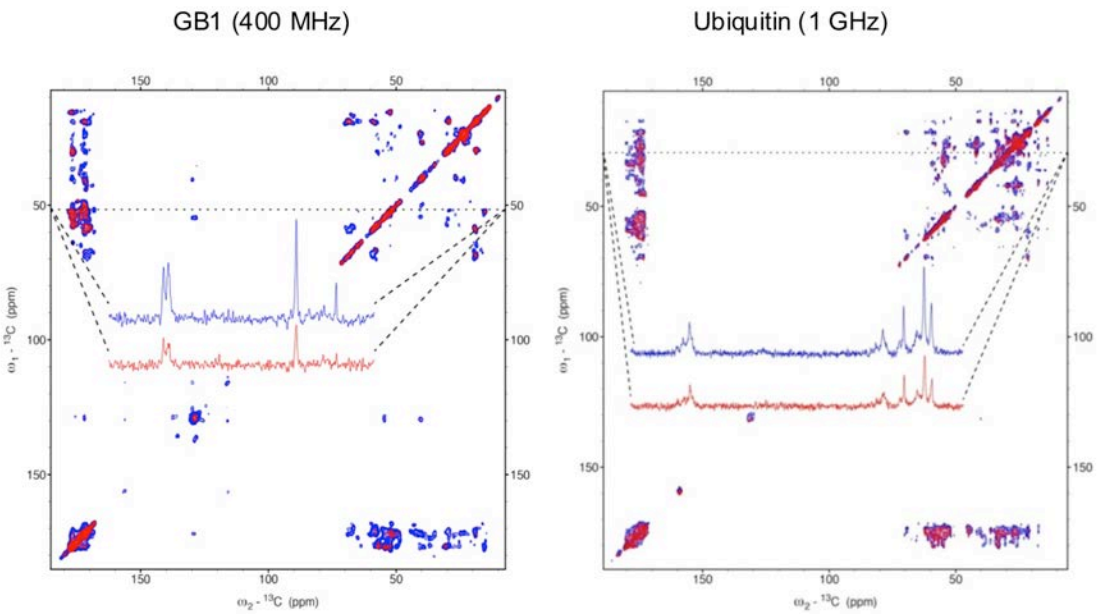

Figure 2.11: 2D ^{13}C-^{13}C correlation spectra of GB1 (left) and Ubiquitin (right) recorded at 9.4 and 23.5 T respectively either without (red) or with (blue) enhancement and equilibration. For GB1, PARIS (N = 2) irradiation with an *rf* amplitude of 15 kHz was applied during 3.0 s for enhancement and equilibration purposes and during the mixing period τ_m = 200 ms. For Ubiquitin, PARIS (N = 1/2) irradiation with an *rf* amplitude of 20 kHz was applied during 3.0 s for enhancement and equilibration and during the mixing period τ_m = 200 ms. The recycle times were the same as in Figs. 7 and 10. The 1.3 mm rotors were spun at 24 kHz. The ^{1}H decoupling field was 96 kHz with PISSARRO. The same pulse sequences were used as in Fig. 2.10.

Studies on mitochondrial membrane protein TSPO

TSPO is a membrane protein that was previously named Peripheral-type Benzodiazepine Receptor (PBR) because of the binding of diazepam, a well-known benzodiazepine, which was initially observed in the kidney. The 18-kilodalton translocator protein TSPO is found in mitochondrial membranes and mediates the import of cholesterol and porphyrins into mitochondria. TSPO transports cholesterol through the external mitochondrial membrane and transfers it to the inner membrane with the assistance of the outer mitochondrial membrane voltage-dependent anion channel (VDAC) and ATPase family AAA domain-containing protein 3 (ATAD3A), which is an integral MP of the inner mitochondrial membrane crossing to the outer membrane [34]. In line with the role of TSPO in mitochondrial function, TSPO ligands are used for a variety of diagnostic and therapeutic applications in animals and humans. The three-dimensional high-resolution structure of mammalian TSPO reconstituted in detergent micelles in complex with its high-affinity ligand PK11195 was recently deciphered [35]. The TSPO-PK11195 structure is described by a tight bundle of five transmembrane α-helices that form a hydrophobic pocket accepting PK11195. Ligand-induced stabilization of the structure of TSPO suggests a molecular mechanism for the stimulation of cholesterol transport into mitochondria.

U-^{13}C, ^{15}N labeled TSPO-PK11195 samples were reconstituted in proeoliposomes (DMPC:DMPE) to check the applicability of sensitivity enhancement by PARIS irradiation. As shown in Fig. 2.12 and 2.13 the method works pretty well for heterogeneous biological systems and significant sensitivity enhancements for further biophysical characterization of this membrane protein can be achieved [36].

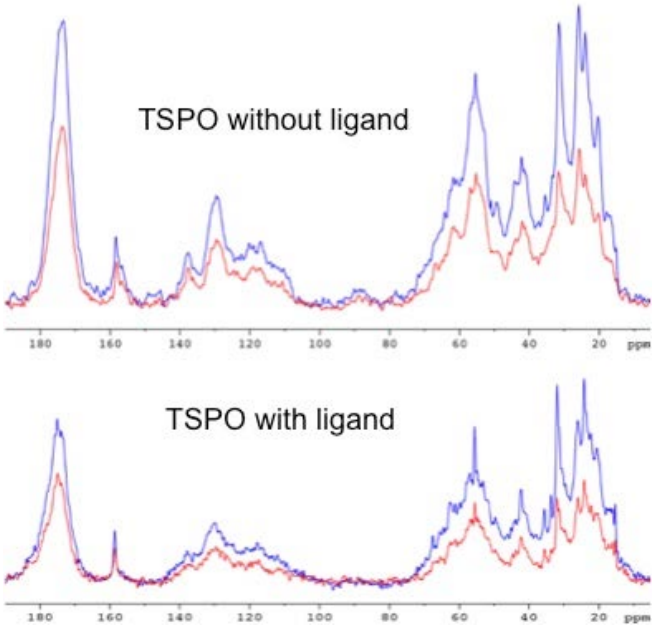

Figure 2.12: Single-pulse reference spectra (red) and PARIS enhanced spectra (blue) of TSPO at 400 MHz (bottom) and 800 MHz (top) respectively. The enhanced spectra were recorded using PARIS-xy (n = 1) irradiation with a proton *rf* amplitude of 10 kHz applied during 3.0 s prior to a reading pulse.

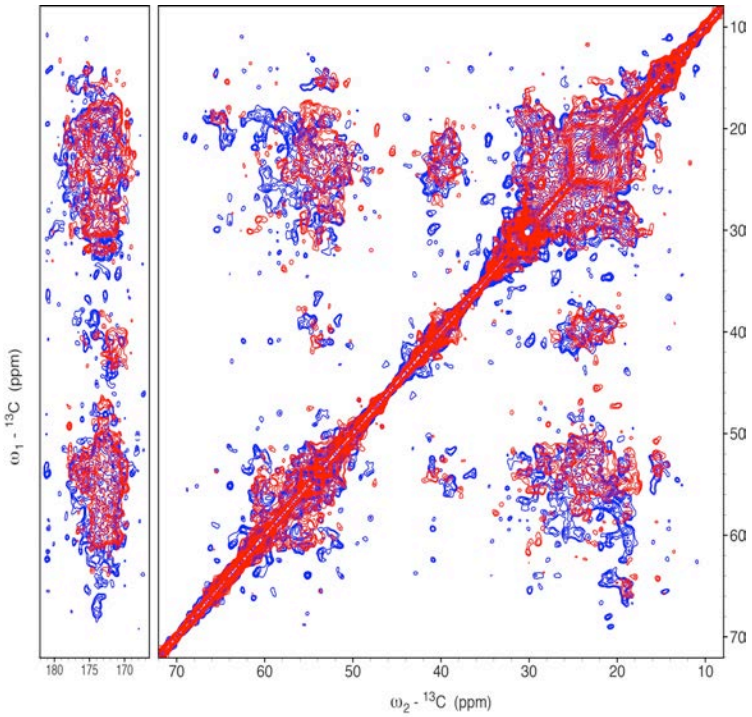

Figure 2.13: 2D ^{13}C-^{13}C correlation spectra of TSPO with PK11195 ligand recorded at 400 MHz either without (red) or with (blue) enhancement and equilibration. PARIS (N = 2) irradiation with an *rf* amplitude of 10 kHz was applied during 3.0 s for enhancement and equilibration purposes and during the mixing period τ_m = 100 ms. The 3.2 mm rotors were spun at 7 kHz. The proton decoupling field was 55 kHz with PISSARRO.

2.2.4 Conclusions

Promoting the efficient equilibration of magnetization by low-power PARIS irradiation leading simultaneously to the spin diffusion breaking of T_1 (^{13}C) constraints and to the heteronuclear Overhauser enhancement, permitted to record quantitative, uniformly enhanced one- and two-dimensional ^{13}C spectra of microcrystalline proteins both at moderate and the highest available static fields. Transient heteronuclear experiments allowed identifying unambiguously the sources of the Overhauser enhancement. The uniformly enhanced quantitative spectra of ^{13}C-labeled microcrystalline proteins, recorded without employing any cross-polarization transfer, show higher gain in intensity than intrinsically non-quantitative, standard cross-polarization spectra. This will benefit a wide range of solid-state NMR experiments to gain insight into structure and dynamics in wide range of bio solids.

2.3 References

1. Wishart, D.S., *TrAC, Trends Anal. Chem.* 2008, 27 (3), 228-237.
2. Holzgrabe, U., R. Deubner, C. Schollmayer, and B. Waibel, *J. Pharm. Biomed. Anal.* 2005, 38 (5), 806-812.
3. Pauli, G.F., B.U. Jaki, and D.C. Lankin, *J. Nat. Prod.* 2005, 68 (1), 133-149.
4. Ziarelli, F. and S. Caldarelli, *Solid State Nucl. Magn. Reson.* 2006, 29 (1–3), 214-218.
5. Chevelkov, V., U. Fink, and B. Reif, *J. Biomol. NMR* 2009, 45 (1-2), 197-206.
6. Schanda, P., B.H. Meier, and M. Ernst, *J. Am. Chem. Soc.* 2010, 132 (45), 15957-15967.
7. Agarwal, V., Y. Xue, B. Reif, and N.R. Skrynnikov, *J. Am. Chem. Soc.* 2008, 130 (49), 16611-16621.
8. Showalter, S.A., E. Johnson, M. Rance, and R. Brüschweiler, *J. Am. Chem. Soc.* 2007, 129 (46), 14146-14147.
9. Weingarth, M., D.E. Demco, G. Bodenhausen, and P. Tekely, *Chem. Phys. Lett.* 2009, 469 (4–6), 342-348.
10. Weingarth, M., G. Bodenhausen, and P. Tekely, *J. Am. Chem. Soc.* 2009, 131 (39), 13937-13939.
11. Weingarth, M., G. Bodenhausen, and P. Tekely, *Chem. Phys. Lett.* 2010, 488 (1–3), 10-16.
12. Herbert-Pucheta, J.-E., P. Pelupessy, G. Bodenhausen, and P. Tekely, *Chem. Phys. Lett.* 2012, 539–540 (0), 245-251.
13. Herbert-Pucheta, J.E., M. Chan-Huot, L. Duma, D. Abergel, G. Bodenhausen, L. Assairi, Y. Blouquit, J.B. Charbonnier, and P. Tekely, *J. Phys. Chem. B* 2012, 116 (50), 14581-91.
14. Weingarth, M., Y. Masuda, K. Takegoshi, G. Bodenhausen, and P. Tekely, *J. Biomol. NMR* 2011, 50 (2), 129-136.
15. Herbert-Pucheta, J.E., H. Colaux, G. Bodenhausen, and P. Tekely, *J. Phys. Chem. B* 2011, 115 (51), 15415-21.

16. Mithu, V.S., S. Bakthavatsalam, and P.K. Madhu, *PLoS ONE* 2013, 8 (1), e50504.
17. Gan, Z.-H. and D.M. Grant, *Chem. Phys. Lett.* 1990, 168 (3–4), 304-308.
18. Gan, Z., D.M. Grant, and R.R. Ernst, *Chem. Phys. Lett.* 1996, 254 (5–6), 349-357.
19. Raleigh, D.P., M.H. Levitt, and R.G. Griffin, *Chem. Phys. Lett.* 1988, 146 (1–2), 71-76.
20. Hou, G., S. Ding, L. Zhang, and F. Deng, *J. Am. Chem. Soc.* 2010, 132 (16), 5538-5539.
21. Giffard, M., M. Bardet, B. Bersch, J. Covès, and S. Hediger, *J. Magn. Reson.* 2009, 200 (1), 153-160.
22. Shahid, S.A., B. Bardiaux, W.T. Franks, L. Krabben, M. Habeck, B.-J. Van Rossum, and D. Linke, *Nat Meth* 2012, 9 (12), 1212-1217.
23. Pauli, J., B. Van Rossum, H. Förster, H.J.M. De Groot, and H. Oschkinat, *J. Magn. Reson.* 2000, 143 (2), 411-416.
24. Pauli, J., M. Baldus, B. Van Rossum, H. De Groot, and H. Oschkinat, *ChemBioChem* 2001, 2 (4), 272-281.
25. Mcdermott, A., T. Polenova, A. Bockmann, K.W. Zilm, E. Paulsen, R. Martin, and G. Montelione, *J. Biomol. NMR* 2000, 16 (3), 209-219.
26. Igumenova, T.I., A.E. Mcdermott, K.W. Zilm, R.W. Martin, E.K. Paulson, and A.J. Wand, *J. Am. Chem. Soc.* 2004, 126 (21), 6720-6727.
27. Igumenova, T.I., A.J. Wand, and A.E. Mcdermott, *J. Am. Chem. Soc.* 2004, 126 (16), 5323-5331.
28. Franks, W.T., D.H. Zhou, B.J. Wylie, B.G. Money, D.T. Graesser, H.L. Frericks, G. Sahota, and C.M. Rienstra, *J. Am. Chem. Soc.* 2005, 127 (35), 12291-12305.
29. Neuhaus, D. and M.P. Williamson, The nuclear Overhauser effect in structural and conformational analysis. 2000, New York: John Wiley.
30. Canet, D., N. Mahieu, and P. Tekely, *J. Am. Chem. Soc.* 1992, 114 (15), 6190-6194.
31. Palmas, P., P. Tekely, P. Mutzenhardt, and D. Canet, *J. Chem. Phys* 1993, 99 (6), 4775-4785.
32. Katoh, E., K. Takegoshi, and T. Terao, *J. Am. Chem. Soc.* 2004, 126 (11), 3653-3657.
33. Giraud, N., J. Sein, G. Pintacuda, A. Böckmann, A. Lesage, M. Blackledge, and L. Emsley, *J. Am. Chem. Soc.* 2006, 128 (38), 12398-12399.
34. Rone, M.B., A.S. Midzak, L. Issop, G. Rammouz, S. Jagannathan, J. Fan, X. Ye, J. Blonder, T. Veenstra, and V. Papadopoulos, *Molecular Endocrinology* 2012, 26 (11), 1868-1882.
35. Jaremko, Ł., M. Jaremko, K. Giller, S. Becker, and M. Zweckstetter, *Science* 2014, 343 (6177), 1363-1366.
36. Lacapere, J.-J., S. Iatmanen-Harbi, L. Senicourt, O. Lequin, P. Tekely, R.N. Purusottam, P. Hellwig, S. Kriegel, S. Ravaud, C. Juillan-Binard, E.P. Peyroula, and V. Papadopoulos, Structural Studies of TSPO, a Mitochondrial Membrane Protein, in *Membrane Proteins Production for Structural Analysis*, I. Mus-Veteau, Editor. 2014, Springer New York. p. 393-421.

3 Site-specific heteronuclear Overhauser measurements in filamentous Pf1 macromolecular assembly

3.1 Introduction

Pf1 virion is a 36 MDa unusually long 20,000-by-60-Å cylinder containing a single-stranded circle of DNA that is extended lengthwise within the particle. This is one of the most highly stretched and twisted form of naturally occurring DNA [1, 2]. Each bacteriophage particle consists of ~7000 symmetrically arranged copies of its 46-residue major capsid protein, a single-stranded circular DNA genome stretched lengthwise on the interior, and a few copies of minor coat proteins at each end.

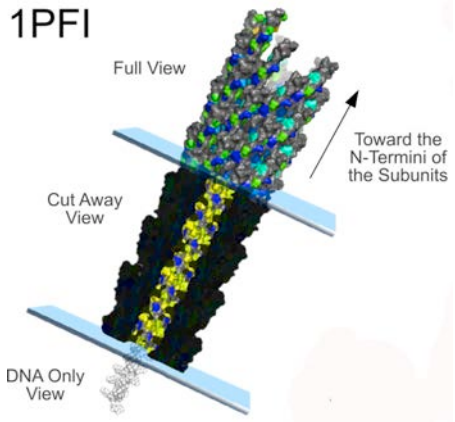

Figure 3: Views of Pf1 bacteriophage capsid structure model (Lorieau et al PNAS, 2007)

It has an unusual 1:1 ratio of nucleotides to major capsid subunits, rather than the usual ratio of 2.0-2.5 within the same family. Filamentous bacteriophages have been investigated in the past extensively using biophysical and molecular biological techniques [3-8]. Earlier studies show that the bacteriophage can exist in two forms, $Pf1_L$ (low temperature) and $Pf1_H$ (high temperature) forms with slightly different symmetries, and that it can undergo a reversible temperature-dependent transition between them and also dependent on the salt concentration [9-16]. The low temperature form, $Pf1_L$ has smaller tilt angle of the monomer subunits resulting into a larger inner pore. Pf1structure is a well-established archetype for the study of one of the two symmetry classes of these viruses [17] and partly due to its unusual assembly mechanism [18-20]. Recently, some studies show the presence of hydration water

inside the highly hydrophobic core of the virion [21, 22]. However, there are still certain puzzling aspects with respect to the structural phase transition and dynamics.

Pf1 is a filamentous bacteriophage in the genus inovirus of family inoviridae that infects specifically strain K of *Pseudomonas aeruginosa* (PAK) [23]. Some filamentous phages also enhance the virulence of their host organisms and are a major concern for human health [24-26]. Much of the acquired knowledge about filamentous phage has been exploited in phage display technology [27]. It has also found application in nanotechnology as templates for assembly of nanostructures [28], and eventually into nano-batteries [29]. Genetically modified and self-assembled form of the phage also generates piezoelectricity [30]. As they have a tendency to orient in magnetic fields, in solution-state NMR it is used for tunable alignment of macromolecules to yield residual dipolar couplings (RDC) [31, 32]. It has also shown promising applications in molecular imaging of cancer cells by hyperpolarized ^{129}Xe chemical exchange saturation transfer (Hyper-CEST) NMR [33, 34].

3.2 Sample preparation

Pf1 phage was isolated and purified from infected cultures of P. aeruginosa; strain K, grown in minimal M9 media with 15NH4Cl and U-13C glucose as the sole nitrogen and carbon sources as described earlier. Following density gradient ultracentrifugation, the sample in high CsCl was precipitated with 4% w/v polyethylene glycol (PEG8000), pelleted, and re-dissolved to a concentration of ~1 mg/ml in 10 mM Tris, pH 8.4. The cryoprotectant ethylene glycol was then added to a final concentration of 30% v/v. A second precipitation was done by mixing MgCl to 5 mM and PEG8000 to 10% w/v. After several minutes of gentle mixing, the suspension was centrifuged for 10 min at 3700 x g. The loose pellet was transferred to a pipette tip sealed at the bottom and further pelleted at ~20,000 x g for 2 h in an Eppendorf micro centrifuge to reduce excess supernatant. The concentration of Pf1 in the pellet was estimated to be ~ 190 mg/ml based on the amount of Pf1 before precipitation (5.5 mg) and the approximate total volume of the resulting pellet. The bottom seal of the pipette tip was then sliced off, and the pellet was sedimented from the tip into a 3.2-mm ZrO2 magic angle spinning NMR rotor. For $Pf1_H$, all steps were carried out at room temperature. All the experiments were performed on a Bruker 800

MHz Avance III spectrometer. The temperature was kept much above the structural transition (283 K) to ensure that the phage is in the high-temperature form.

3.3 Results and discussion

3.3.1 Recording site-specific one- and two-dimensional ^{13}C NOE spectra

The pulse sequences used to record such spectra are shown in Fig. 3.1. The experiments begin with a saturation irradiation applied to carbon-13 magnetization. This saturation consists in two long pulses (10 ms and 5 ms, respectively) applied along the two directions of the rotating frame. This permits to establish perfectly defined initial state of carbon magnetization (magnetization is zero) and to repeat the acquisition according to the proton relaxation times, which are usually much shorter than those of carbons. The saturation period is immediately followed by two 90° proton pulses. The phase inversion of the second proton pulse along with the alternation of the acquisition sign cancels any carbon-13 magnetization, which would recover by longitudinal relaxation during the cross-relaxation period t_{cr}.

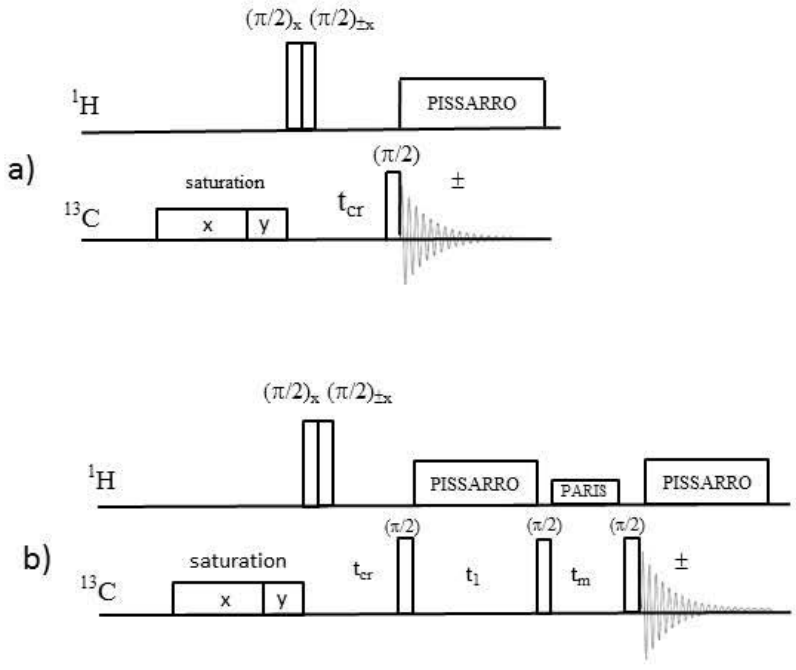

Figure 3.1: Pulse sequences for recording 1D (a) and 2D (b) heteronuclear NOE ^{13}C spectra.

As shown in Fig. 3.2 this permits to record 1D ^{13}C NOE spectra at different cross-relaxation delays.

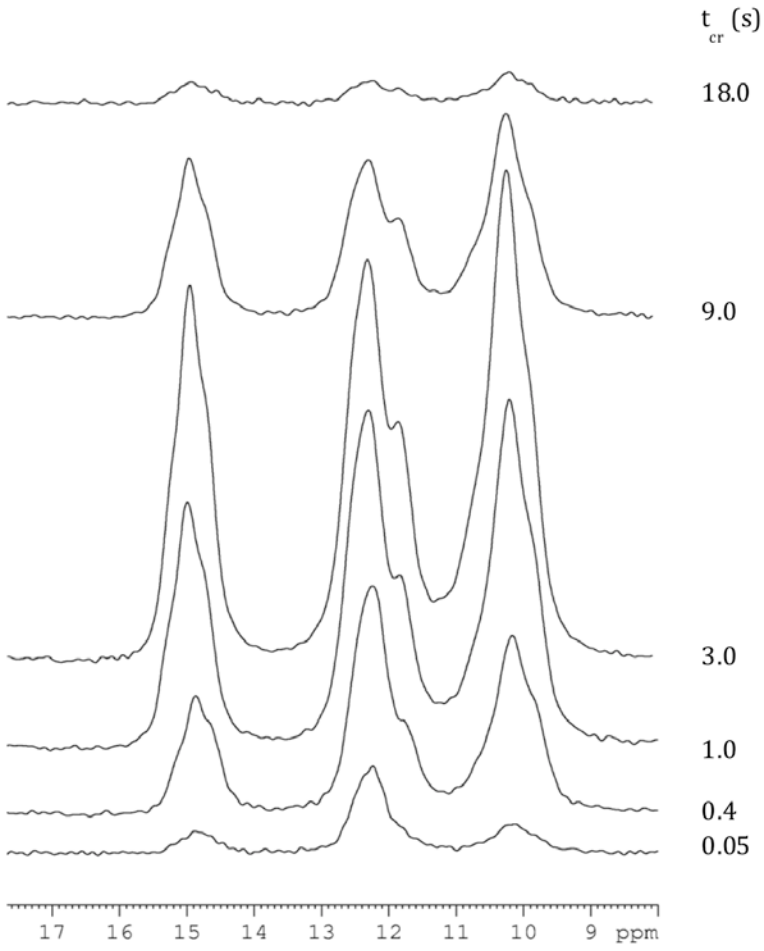

Figure 3.2: Pure NOE ^{13}C spectra of methyl groups from two crystallographically independent molecules in L-isoleucine recorded on a 800 MHz Bruker spectrometer at 13 kHz MAS using the pulse sequence from 3.3.1a with different cross-relaxation delay t_{cr}.

Site-specific heteronuclear NOE information remains inaccessible from the 1D spectra with overlapping ^{13}C resonances. Moreover, in fully protonated solids, the access to individual proton sites is not available even at very high spinning frequencies. However, the site-specific heteronuclear NOE information can still be obtained by using the pulse sequence shown in 3.1b, which combines 1D NOE experiment and a 2D procedure permitting to record the ^{13}C-^{13}C correlations spectra. To promote efficient magnetization exchange between directly bonded carbons, a short-time low-power PARIS irradiation is applied during the mixing period.

^{13}C-^{13}C correlations NOE spectrum of L-isoleucine recorded by using the pulse sequence in Fig. 3.1b is shown in Fig. 3.3.

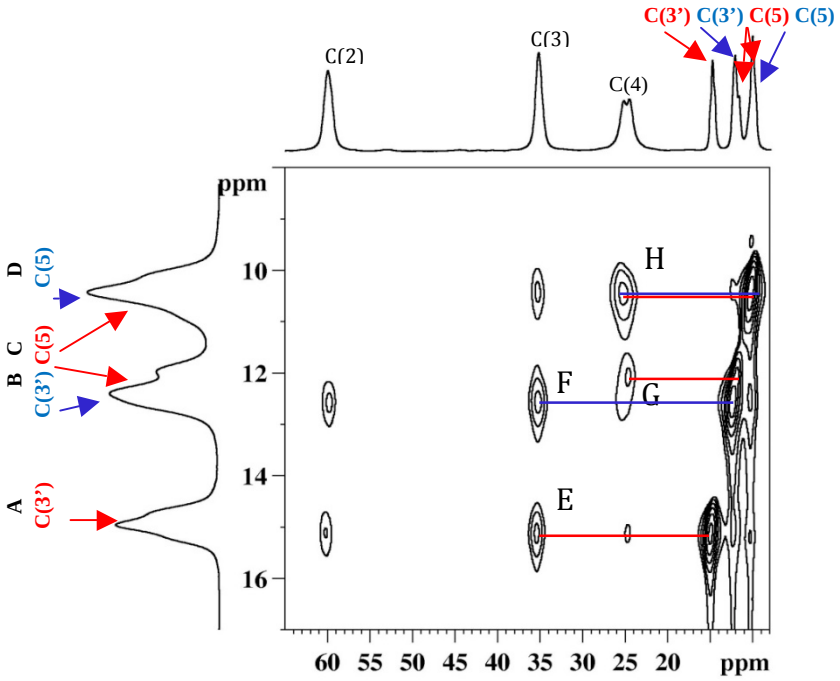

Figure 3.3: ^{13}C-^{13}C correlation spectrum of U-^{13}C labeled L-isoleucine recorded on a 800 MHz Bruker spectrometer at 13 kHz MAS using the pulse sequence from Fig. 3.1b with a cross-relaxation delay t_{cr} = 3 s. First-neighbor contacts of the methyl carbons in two crystallographically independent molecules are represented by cross-peaks E, F, G, H. During a mixing period t_m = 5 ms, low-power PARIS irradiation was used with an rf amplitude of 10 kHz.

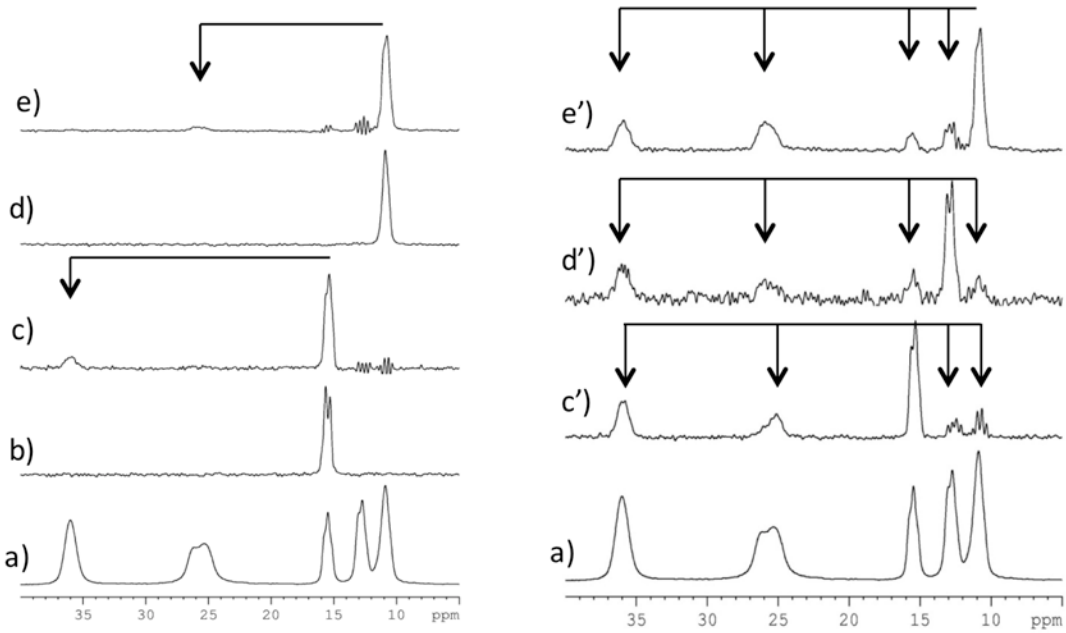

ure 3.4: (bottom) Excerpts from ^{13}C CP/MAS spectra of L-isoleucine. (b, d) Selective excitation of methyl resonances A and D using SELDOM pulse sequence [35]. Other spectra were recorded after selective excitation and a period of spin-exchange during 2.5 ms (c, e) and 50 ms (c', d', e') using PARIS irradiation with an rf amplitude of 10 kHz.

The assignment of partially overlapping resonances of methyl groups from two crystallographically independent molecules having different torsional angles about the C(1) C(2) bond of L-isoleucine [36], has been fully corroborated by selective excitation experiments as shown in Fig. 3.4. The full set of build-up curves extracted from one- and two-dimensional NOE experiments are shown in Fig. 3.5.

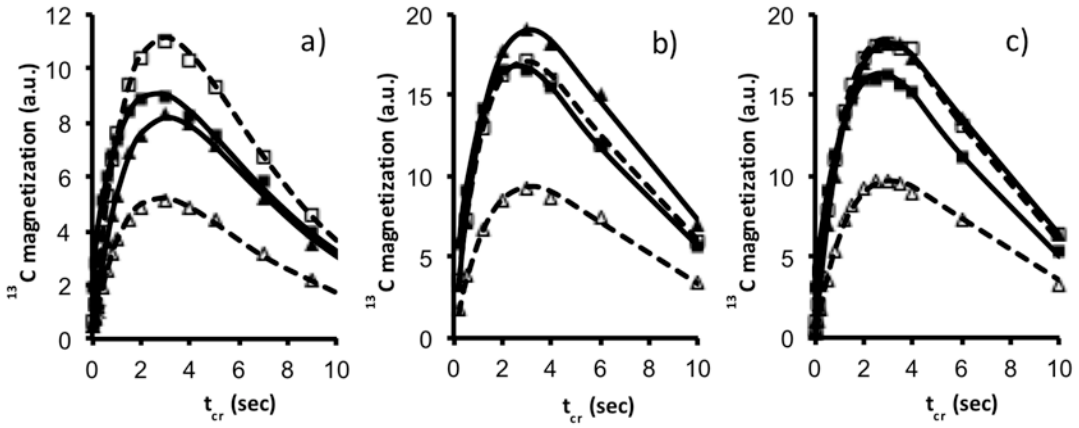

Figure 3.5: Experimental (symbols) and fitted (lines) build-up curves of carbon-13 magnetization due to transient heteronuclear Overhauser effects as a function of the cross relaxation delay t_{cr} for resonances of the methyl carbons of L-isoleucine extracted from the 1D spectra (a) and from the cross-peaks in 2D ^{13}C-^{13}C correlation spectra (b, c). PARIS (N=1/2) irradiation with an *rf* amplitude of 10 kHz was applied during 5 ms (b) and 10 ms (c). The experimental data in (a) are for resonance peaks A (filled triangles), B (filled squares), C (empty triangles) and D (empty squares), in (b, c) for the cross-peaks E (filled triangles), F (filled shares), G (open triangles) and H (open squares) as specified in Fig. 3.3.

In analogy to the dynamics of cross-relaxation of GB1 (chapter 2), in all cases the data strictly obey the temporal evolution described by the Solomon equations. Equally importantly, the same (± 5%) sets of cross-relaxation rate constants for relevant methyl groups were obtained by fitting the experimental data from 1D and 2D experiments with two different mixing times. This proves the feasibility and reliability of our 2D approach in accessing site-specific NOE data, providing limited duration of the mixing period to restrict to nearest-neighbor contacts.

	Molecule I		Molecule II	
	C(3')	C(5)	C(3')	C(5)
$<\sigma_{CH}>$	0.1	0.47	0.42	0.56
R_1^H	1.05	1.04	0.92	1.04
R_1^C	0.59	0.84	0.87	0.84

Table 1: Average cross-relaxation rate constants $<\sigma_{CH}>$ (s^{-1}) for C(3') and C(5) methyl carbons in two crystallographically independent molecules of L-isoleucine extracted from one-and two-dimensional experiments. The relevant R_1^H and R_1^C relaxation rates were extracted from the initial slopes in independent relaxation measurements.

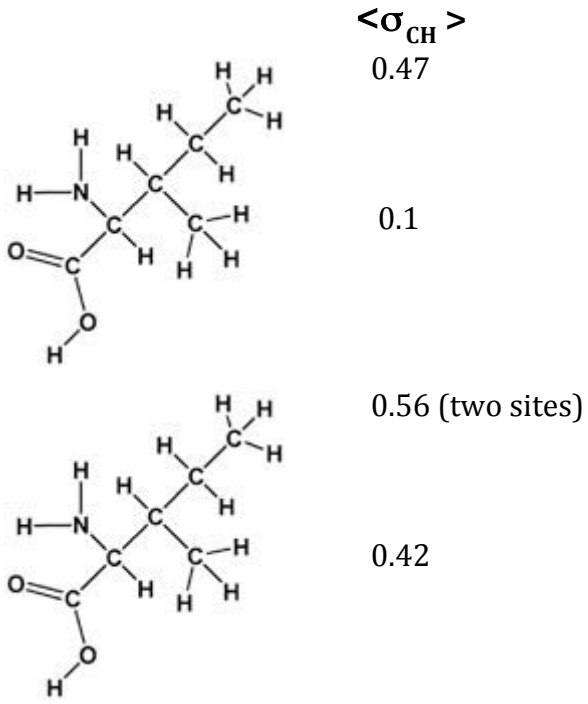

Figure 3.6: Average cross-relaxation rate constants $<\sigma_{CH}>$ (s^{-1}) for C(3') and C(5) methyl carbons in two crystallographically independent molecules of L-isoleucine extracted from the build-up curves shown in Fig. 3.5.

Interestingly, significantly different cross-relaxation rate constant has been obtained for the C(3') methyl carbon in one of two crystallographically inequivalent molecules (Table 1, Fig. 3.6). This could be induced by a higher steric hindrance in three-fold rotation of this particular methyl group due to the differences of local packing in the asymmetric unit of L-isoleucine. Molecular dynamics simulations [37] have indeed suggested that in the crystals of DL-Leucine and D-valine, the individual methyl groups have different steric environments resulting in different effective barriers to rotation. It can be both intra- and intermolecular in origin and are reflected in the correlation times changing in a large range from 5.7 to 170 ps [37]. Similar manifestations of possible steric hindrance in the internal dynamics of some methyl groups at different spatial emplacements in the filamentous Pf1 protein assembly are discussed below.

3.3.2 Probing internal dynamics of methyl groups in Pf1

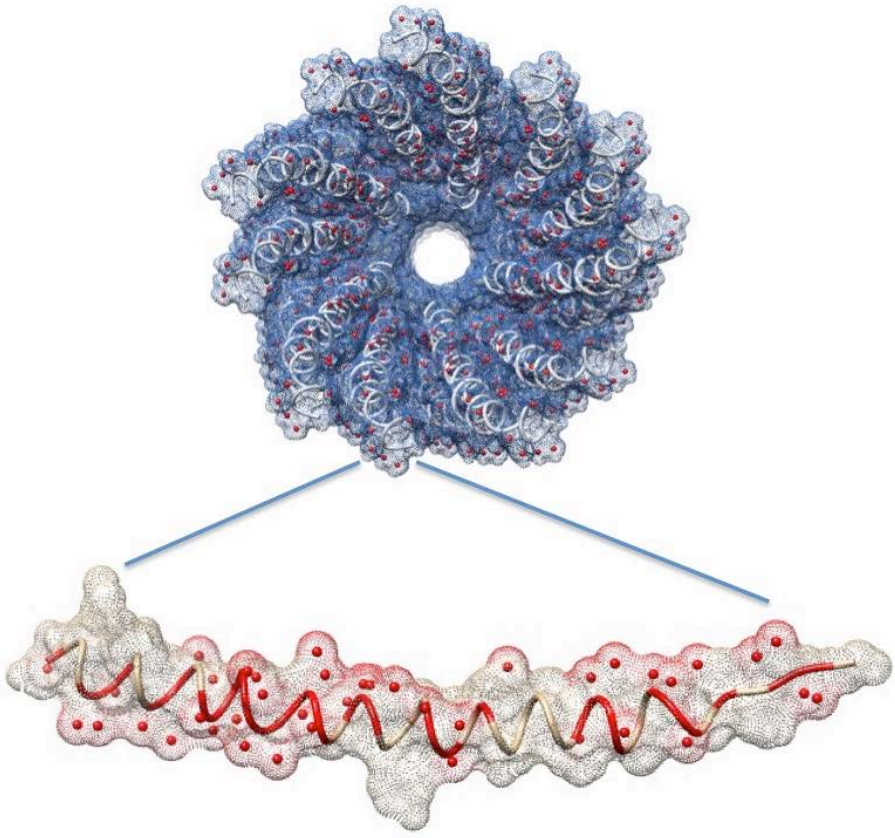

Figure 3.7: Pf1 macromolecular assembly and a monomer unit showing the methyl groups (red dots), which serves as the main reservoir of NOE.

Several one-dimensional ^{13}C spectra were recorded first on U-^{13}C, ^{15}N $Pf1_H$ samples. Figure 3.8 shows four spectra where the blue spectrum is a transient heteronuclear NOE enhanced spectrum with a cross-relaxation time (t_{cr}) of 600ms, a single pulse ^{13}C spectrum is shown in red and the difference of these two in green. An overlay of this difference spectrum with the pure NOE spectrum shown in magenta and recorded employing the one-dimensional version of the pulse sequence (fig.3.1a) confirms the reliability of the method.

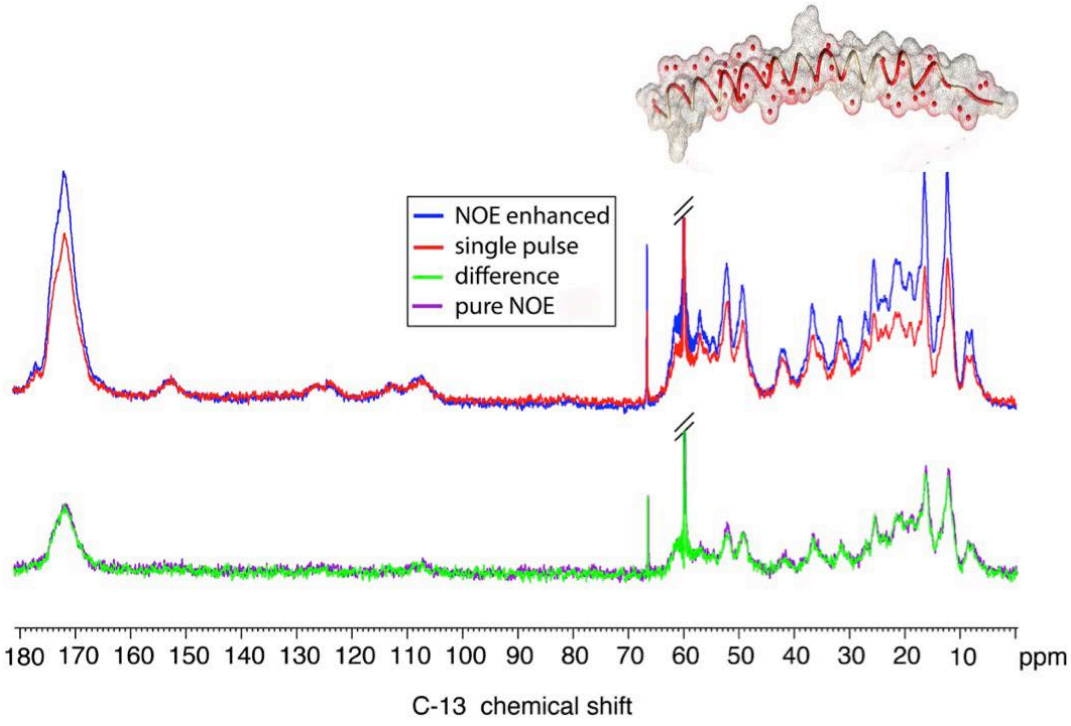

Figure 3.8: Top: Transient NOE enhanced ^{13}C spectrum (blue) and single-pulse ^{13}C reference spectrum (red); Bottom: Difference of the two spectrum on the top (green) and pure NOE ^{13}C spectrum (magenta) with a cross-relaxation delay t_{cr} of 600 ms.

The preparation of simple initial state with saturation irradiation (prior to cross-relaxation time) and the cancellation of the carbon magnetization, which would reconstruct through its own longitudinal relaxation, by the phase cycling once again allows to take the same benefits in the 2D version of the pulse scheme (fig.3.1b).
This pulse scheme was utilized to record a set of 2D experiments with variable cross-relaxation delay times to get a full build up profile of individual cross-peaks containing site-specific motional information.

A 2D ^{13}C-^{13}C correlation NOE spectrum recorded using a cross-relaxation time of 600 ms is shown in figure 3.9.

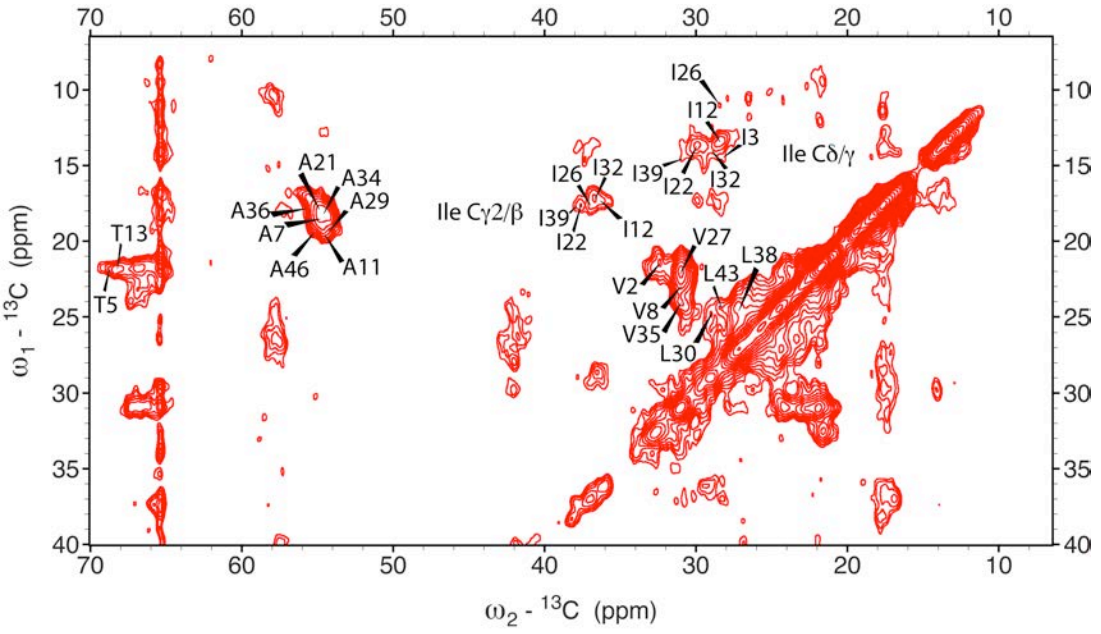

Figure 3.9: ^{13}C-^{13}C correlation spectrum of U-^{13}C, ^{15}N labeled Pf1 recorded on a 800 MHz Bruker spectrometer at 13 kHz MAS using the pulse sequence from Fig. 3.1b with a cross-relaxation delay t_{cr} = 600 ms. during a mixing period t_m = 50 ms, low-power PARIS irradiation was used with an rf amplitude of 10 kHz.

The mixing times (t_m) were chosen and kept relatively short (50 ms) to restrict the magnetization transfer by PARIS to the first neighbors and minimizethe spin-diffusion effects. Some representative, site-specific build up profiles obtained from the time dependence of intensity of relevant cross-peaks in 2D experiments are shown in fig. 3.10. The full set set of data is given in Table 2.

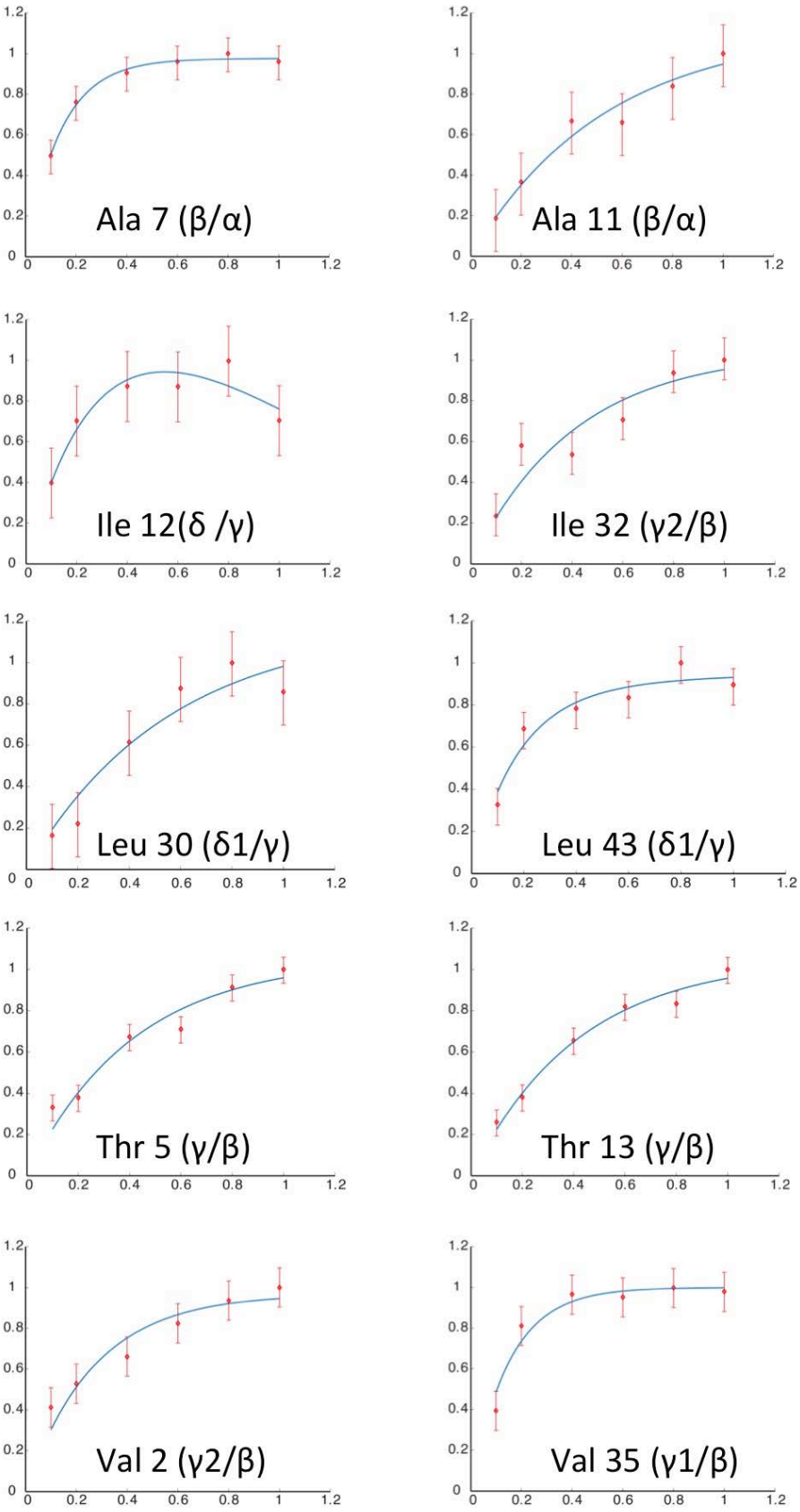

Figure 3.10: Mono/bi-exponential fit of the build up profiles of different cross-peaks obtained from the series of 2D experiments with different cross-relaxation times.

Residue	Slope	Residue	Slope	Residue	Slope
Val2 (γ/β)	3.752	Ile22 (δ/γ1)	2.791	Leu43 (δ/y)	5.319
Val8 (γ/β)	4.512	Ile22 (γ2/β)	2.312	Ala7 (β/α)	7.253
Val27 (γ/β)	5.043	Ile26 (δ/γ1)	1.335	Ala11 (β/α)	1.888
Val35 (γ/β)	6.644	Ile26 (γ2/β)	2.533	Ala21 (β/α)	6.454
Thr5 (γ/β)	2.422	Ile32 (δ/γ1)	4.293	Ala29 (β/α)	5.448
Thr13 (γ/β)	2.401	Ile32 (γ2/β)	2.287	Ala34 (β/α)	6.198
Ile12 (δ/γ1)	4.542	Ile39 (δ/γ1)	2.008	Ala36 (β/α)	4.237
Ile12 (γ2/β)	1.56	Ile39 (γ2/β)	1.401	Ala46 (β/α)	1.758
Leu30 (δ/y)	1.8	Leu38 (δ/y)	3.949		

Table 2: Slope (in s^{-1}) of various cross-peaks extracted from the buildup profiles in the 2D experiments.

Noticeable, each residue has its specific buildup profile. In general, the most dynamic residues are expected to have steeper slope and a higher value of cross-relaxation rate constant than the rigid counterparts. However, as shown on L-isoleucine in section 3.3.1, some effects from steric hindrance can modify the three-fold rotation of the methyl groups affecting directly the observed NOE at the specific site. In fully hydrated Pf1 macromolecular assembly, hydrophobic protein side chain residues have two major features that could significantly influence the three-fold dynamics of a specific methyl site: (i) internal conformational/restricted fluctuations dynamics of the lateral chains which could manifest through a modified intra/inter residue steric hindrance and (ii) proximity to a hydrophilic site which could create additional crowding/mobility effects felt by the methyl group on a nearby site. Even hydrophobic non- exchangeable residues (including alanine, valine, isoleucine, and leucine) at the N- and C-termini of Pf1 have been shown to be hydrated in a very recent study [22] . Consequently, special care has to be taken when considering different structural and motional factors, which could play an active role in modified dynamics of the methyl groups. Further studies will be necessary to get a meaningful insight into the molecular reasons of different internal dynamics of individual methyl groups in Pf1 assembly as revealed by site-specific heteronuclear NOE measurements.

3.4 References

1. Sergeyev, I.V., L.A. Day, A. Goldbourt, and A.E. Mcdermott, *J. Am. Chem. Soc.* 2011, 133 (50), 20208-20217.
2. Liu, D. and L. Day, *Science* 1994, 265 (5172), 671-674.
3. Nambudripad, R., W. Stark, and L. Makowski, *J. Mol. Biol.* 1991, 220 (2), 359-379.
4. Thiriot, D.S., A.A. Nevzorov, L. Zagyanskiy, C.H. Wu, and S.J. Opella, *J. Mol. Biol.* 2004, 341 (3), 869-879.
5. Goldbourt, A., B.J. Gross, L.A. Day, and A.E. Mcdermott, *J. Am. Chem. Soc.* 2007, 129 (8), 2338-2344.
6. Shon, K., Y. Kim, L. Colnago, and S. Opella, *Science* 1991, 252 (5010), 1303-1305.
7. Thomas, G.J. and P. Murphy, *Science* 1975, 188 (4194), 1205-1207.
8. Marvin, D.A., *Current Opinion in Structural Biology* 1998, 8 (2), 150-158.
9. Wachtel, E.J., F.J. Marvin, and D.A. Marvin, *J. Mol. Biol.* 1976, 107 (3), 379-383.
10. Nave, C., A.G. Fowler, S. Malsey, D.A. Marvin, H. Siegrist, and E.J. Wachtel, *Nature* 1979, 281 (5728), 232-234.
11. Welsh, L.C., M.F. Symmons, and D.A. Marvin, *Acta Crystallographica Section D* 2000, 56 (2), 137-150.
12. Specthrie, L., J. Greenberg, M.J. Glucksman, J. Diaz, and L. Makowski, *Biophys. J.* 52 (2), 199-214.
13. Thiriot, D.S., A.A. Nevzorov, and S.J. Opella, *Protein Science : A Publication of the Protein Society* 2005, 14 (4), 1064-1070.
14. Hinz, H.J., K.O. Greulich, H. Ludwig, and D.A. Marvin, *J. Mol. Biol.* 1980, 144 (3), 281-289.
15. Thomas Jr, G.J., B. Prescott, and L.A. Day, *J. Mol. Biol.* 1983, 165 (2), 321-356.
16. Marvin, D.A., C. Nave, M. Bansal, R.D. Hale, and E.K.H. Salje, *Phase Transitions* 1992, 39 (1-4), 45-80.
17. Marvin, D.A. and B. Hohn, *Bacteriological Reviews* 1969, 33 (2), 172-209.
18. Nambudripad, R., W. Stark, S. Opella, and L. Makowski, *Science* 1991, 252 (5010), 1305-1308.
19. Park, S.H., F.M. Marassi, D. Black, and S.J. Opella, *Biophys. J.* 99 (5), 1465-1474.
20. Marvin, D.A., M.F. Symmons, and S.K. Straus, *Prog. Biophys. Mol. Biol.* 2014, 114 (2), 80-122.
21. Purusottam, R.N., R.K. Rai, and N. Sinha, *J. Phys. Chem. B* 2013, 117 (10), 2837-2840.
22. Sergeyev, I.V., S. Bahri, L.A. Day, and A.E. Mcdermott, *J. Chem. Phys* 2014, 141 (22), 22D533.
23. Takeya, K. and K. Amako, *Virology* 1966, 28 (1), 163-165.
24. Wagner, P.L. and M.K. Waldor, *Infection and Immunity* 2002, 70 (8), 3985-3993.
25. Webb, J.S., L.S. Thompson, S. James, T. Charlton, T. Tolker-Nielsen, B. Koch, M. Givskov, and S. Kjelleberg, *J. Bacteriol.* 2003, 185 (15), 4585-4592.

26. Nasu, H., T. Iida, T. Sugahara, Y. Yamaichi, K.-S. Park, K. Yokoyama, K. Makino, H. Shinagawa, and T. Honda, *J. Clin. Microbiol.* 2000, 38 (6), 2156-2161.
27. Mccafferty, J., A.D. Griffiths, G. Winter, and D.J. Chiswell, *Nature* 1990, 348 (6301), 552-554.
28. Nam, K.T., D.-W. Kim, P.J. Yoo, C.-Y. Chiang, N. Meethong, P.T. Hammond, Y.-M. Chiang, and A.M. Belcher, *Science* 2006, 312 (5775), 885-888.
29. Lee, Y.J., H. Yi, W.-J. Kim, K. Kang, D.S. Yun, M.S. Strano, G. Ceder, and A.M. Belcher, *Science* 2009, 324 (5930), 1051-1055.
30. Lee, B.Y., J. Zhang, C. Zueger, W.-J. Chung, S.Y. Yoo, E. Wang, J. Meyer, R. Ramesh, and S.-W. Lee, *Nat Nano* 2012, 7 (6), 351-356.
31. Hansen, M.R., L. Mueller, and A. Pardi, *Nat Struct Mol Biol* 1998, 5 (12), 1065-1074.
32. Zweckstetter, M. and A. Bax, *J. Biomol. NMR* 2001, 20 (4), 365-377.
33. Palaniappan, K.K., R.M. Ramirez, V.S. Bajaj, D.E. Wemmer, A. Pines, and M.B. Francis, *Angewandte Chemie International Edition* 2013, 52 (18), 4849-4853.
34. Stevens, T.K., K.K. Palaniappan, R.M. Ramirez, M.B. Francis, D.E. Wemmer, and A. Pines, *Magnetic Resonance in Medicine* 2013, 69 (5), 1245-1252.
35. Tekely, P., J. Brondeau, K. Elbayed, A. Retournard, and D. Canet, *J. Magn. Reson.* 1988, 80 (3), 509-516.
36. Torii, K. and Y. Iitaka, *Acta Crystallographica Section B* 1971, 27 (11), 2237-2246.
37. Chatfield, D.C., A. Augsten, C. D'cunha, and S.E. Wong, *J. Comput. Chem.* 2003, 24 (9), 1052-1058.

4 Probing the gel to liquid-crystalline phase transition and relevant conformational changes in liposomes by ^{13}C magic-angle spinning NMR

4.1 Introduction

Conformation and dynamics of phospholipid molecules play an important role in determining physical properties and biological functions of biomembranes [1, 2]. They are of prime importance for understanding many basic biological functions like cell-cell surface recognition and cell fusion, transmembrane signaling and ligand-receptors interactions, the control of transmembrane potential, the function of ionic channels or the modulation of membrane enzymes by the lipidic environment. Lipid bilayers can exist in various phases depending on temperature and water content. Consequently, the phase transition in lipids can be thermotropic or lyotropic, i. e. induced by varying the temperature or hydration level, respectively [1].

Several nuclear magnetic resonance (NMR) techniques have been used to study the dynamics of lipid membranes. Deuterium or phosphorus NMR spectra of static samples are used for decades to probe the dynamics of lipid bilayers [3, 4]. Both are sensitive to the movements present in the lipid phases and permit determining phase diagrams in pure lipids or lipid mixture [5]. ^{1}H NMR wide-line measurements revealed that the chain conformation was considerably different upon the passage from the gel to liquid crystalline phase [6]. ^{13}C solid-state NMR spectroscopy is particularly well suited for dynamic studies since it allows the simultaneous investigation of different regions of the lipid molecules, i.e. the polar head group, the glycerol backbone and the acyl chains. Among others, crystalline forms of some racemic and enantiomerically pure phospholipids have been investigated using ^{13}C and ^{31}P cross-polarization (CP) magic-angle spinning (MAS) NMR [7]. The invariance of chemical shifts in the gel phases indicated that no major conformational changes occurred during phase transitions of hydrated bilayers of phosphatidylcholine [7].

Very recently, structural information on crystalline DMPC and the physical properties of DMPC at a low hydration level have been obtained from the ^{13}C CP/MAS NMR

spectra [8]. Fourier transform infrared spectroscopy has been also used to study the changes of acyl chain conformations in phospholipid bilayers to follow lipid phase transitions trough the relative intensity changes of the vibration bands on *trans* and *gauche* segments [9].

In this chapter we report simple spectroscopic features of the main thermotropic phase transition in phospholipid liposomes related to the hydrocarbon chain order-disorder dynamics and the relevant changes of conformations as revealed by the ^{13}C MAS NMR spectra recorded at different temperatures. To our knowledge such spectroscopic features have not been investigated in details and reported so far by using solid state ^{13}C NMR spectroscopy.

4.2 Materials and methods

All lipids (DMPC, 14:0 1,2-dimyristoyl-*sn*-glycéro-3-phosphocholine and DMPE, 14:0 1,2-dimyristoyl-*sn*-glycéro-3-phosphoéthanolamine) were purchased from Avanti Polar™. Pure DMPC liposomes were obtained by adding aqueous buffer solution to the lipid powder (1ml for 100mg). For DMPC/DMPE mixture, chloroform solutions of each lipid were mixed at a 9/1 ratio and solvent evaporated using a rotary evaporator (BuchiTM). Liposomes were obtained by rehydrating the mixture with aqueous buffer as for the DMPC lipids. 4 mm rotors were filled by pipeting lipid solution and a slow speed centrifugation to remove air bubbles. All ^{13}C NMR spectra were recorded for natural abundance DMPC and DMPC/DMPE samples using a single pulse experiments and PISSARRO dipolar decoupling during the acquisition period. Samples of uniformly ^{13}C, ^{15}N labeled TSPO membrane protein reconstituted in natural abundance DMPC/DMPE mixture with and without PK11195 ligand were prepared as described elsewhere [10]. All experiments were performed on a BRUKER Avance II spectrometer with a 4.0 mm rotor spinning at a frequency ν_r = 7 kHz in a magnetic field of 9.4 T (400 MHz for ^1H). The ^{13}C chemical shifts were referenced with respect to the carboxyl carbon of α-glycine (δ_{iso}= 176.5 ppm) [11]. All temperatures of the sample were determined as described elsewhere [12]. The Dmfit program [13] was used for the deconvolution of NMR spectra and the line-shape fitting.

4.3 Results and discussion

4.3.1 Probing trans-gauche conformational changes

Figure 4.1 shows three spectral excerpts from the ^{13}C MAS spectra of DMPC recorded at different temperatures. Two sets of resonances resulting from the coexistence of gel and liquid-crystalline phases are clearly visible for carbons 3, 4-11 and 13 in the spectrum recorded at 303 K. The peak-fitting deconvolution analysis for resonances from the central fragment of the acyl chain encompassing the carbons C4–11 is illustrated in Fig. 4.2. The spectra reveal that the resonance signal of the acyl C4-11 carbons has a multi-component character, whatever the temperature or phase state, and can be deconvoluted with two or three Lorentzian lines. These resonance lines were assigned to the inner and outer parts of this central fragment.

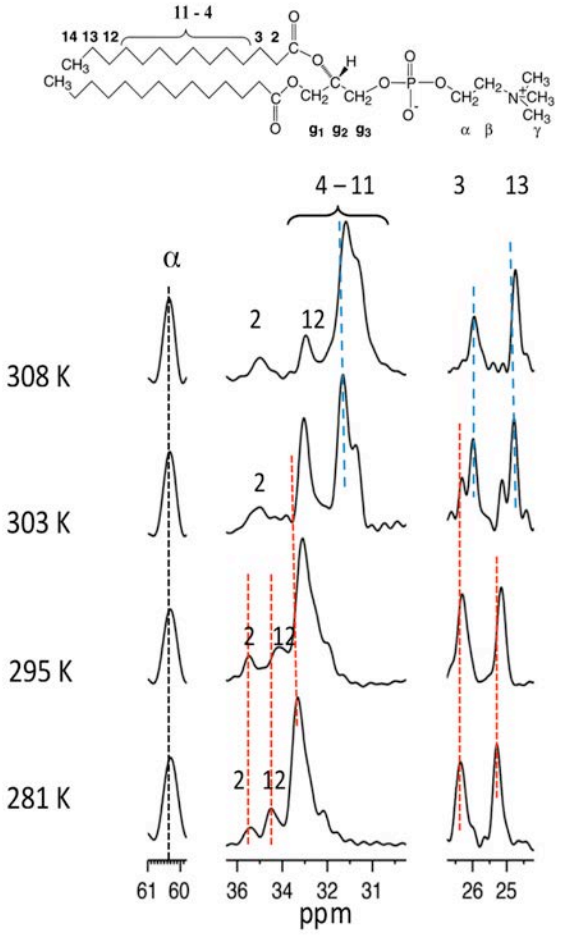

Figure 4.1: (Top) Chemical structure of DMPC. (Bottom) Excerpts from ^{13}C MAS spectra of DMPC recorded at different temperatures encompassing the gel to liquid-crystalline thermotropic phase transition. Note the presence of two sets of resonances in the spectrum recorded at 303 K resulting from the coexistence of two phases.

As visible in Fig. 4.1, all resonances, except from the α carbon, show a high-field shift with increasing temperature. This must be related to the increasing population of *gauche* conformations involved in rapid *trans-gauche* conformational exchange on the NMR time scale. In the gel state at 280 K, all carbons of the acyl chain are supposed to be in an all-*trans* conformation. In contrast, fast exchange between the *trans* and *gauche* conformations occurs at higher temperatures. When a carbon is in a *gauche* rather than a *trans* conformation, the resulting resonance has a smaller chemical shift. Thus, the *gauche* conformations move the resonances up-field. The lowest chemical shift would be reached when the chain assumes the all-*gauche* conformation. Liquid cyclohexane is constrained in such a conformation, and exhibits a chemical shift of 27.84 ppm.

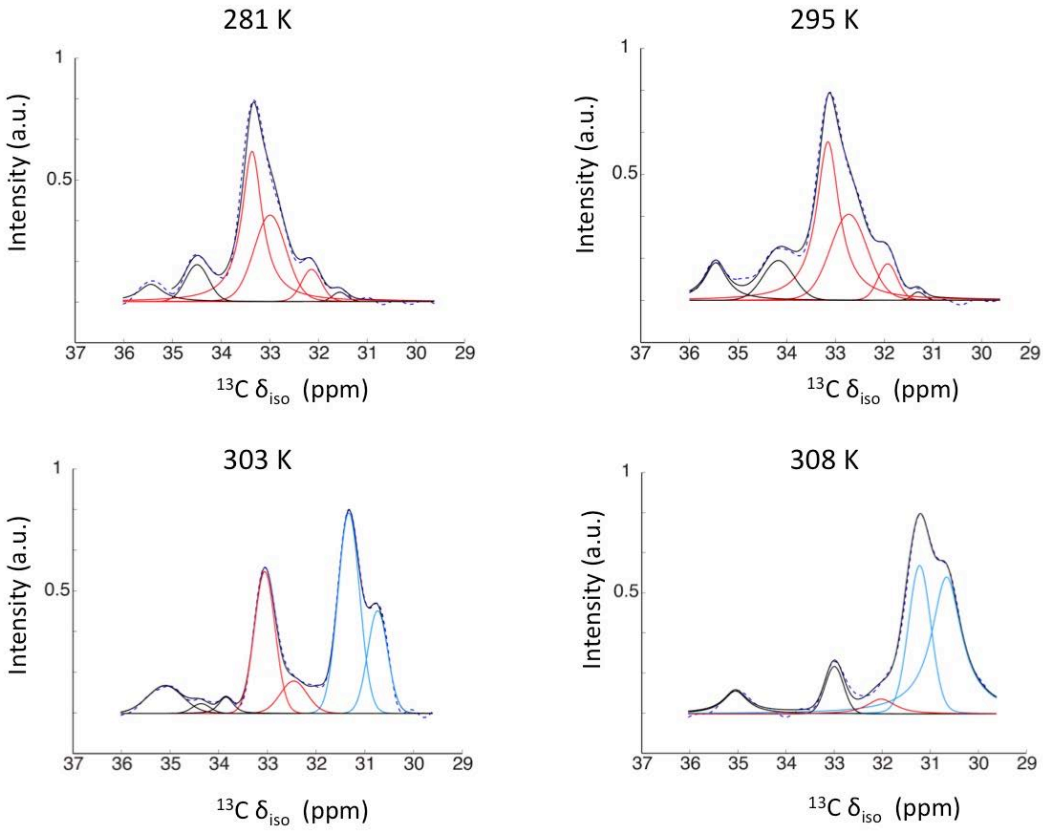

Figure 4.2 : The peak-fitting deconvolution analysis of resonances from the central fragment of the acyl chain encompassing the carbons C4 –C11 in ^{13}C MAS spectra of DMPC liposomes recorded at different temperatures.

Considering that the observed isotropic chemical shift is determined by a linear relationship between the values of the all-*trans* and all-*gauche* conformations

$$\delta_{obs} = f_t \delta_t + f_g \delta_g \quad (1)$$

the fraction of *gauche* conformers, f_g, can be estimated as

$$f_g = (\delta_t - \delta_{obs})/ (\delta_t - \delta_g) \quad (2)$$

This permits to access the fraction of *gauche* conformations at different temperatures from the experimental chemical shifts.

Table 1 gives the fraction of *gauche* conformations for different carbons in the acyl chains of the DMPC liposomes. Significant differences in the percentage of *gauche* conformations induced with increasing temperatures appear clearly for carbons with different emplacement in the acyl chain.

Temperature (K)	Phase	C2	C3	C4 - C11	C12	C13
281	L_β	0.00	0.00	0.00 (0.56)	0.00	0.00
	L_β			0.00 (0.36)		
	L_β			0.00 (0.08)		
295	L_β	0.00	0.03	0.02 (0.57)	0.06	0.05
	L_β			0.04 (0.35)		
	L_β			0.05 (0.08)		
303	L_β	0.00	0.03	0.05 (0.29)		0.06
	L_β			0.05 (0.09)		
	L_α	0.09	0.14	0.30 (0.42)	0.26	0.18
	L_α			0.25 (0.20)		
306	L_β	0.00		0.05 (0.10)		
	L_α	0.09	0.14	0.32 (0.37)	0.26	0.18
	L_α			0.27 (0.53)		
308	L_β			0.05 (0.06)		
	L_α	0.09	0.14	0.32 (0.38)	0.26	0.18
	L_α			0.28 (0.56)		

Table 1: Fraction of gauche conformations as a function of temperature at different carbons of the acyl chains in DMPC liposomes extracted from the relevant isotropic chemical shifts. The numbers in parenthesis give the relative amount of each component for the central C4-11 fragment.

At 308 K the central C14-11 carbons reach the highest percentage while the C2 carbon shows the smallest values. The hydrated bilayers change their phase with increasing temperature from the gel phase (L_{β}) to the liquid-crystalline phase (L_{α}) phase [1]. The Table 1 shows that the gel to liquid-crystalline phase transition creates more gauche conformers in the middle of the fatty acyl chains than at the end and especially at its beginning close to the polar head. This strongly suggests that the formation of *gauche* conformers is favored in the middle of the chain. For the central fragment of eight carbons the fraction ranging from 0.28 to 0.32 translates into an average number of 2.2 - 2.6 *gauche* conformers. Including the average fraction for the outer carbons, this is close to a lower limit reported by Seelig and Seelig [3] who estimated from the deuterium NMR that the number of *gauche* conformers in the liquid crystalline phase of pure dipalmitoylphosphatidylcholine is 3 - 6.

Apart from initially smaller chemical shifts values of acyl carbons in the gel phase of DMPC, as compared with those observed in this study, much modest change in the ^{13}C isotropic chemical shifts was reported earlier upon the passage through the gel to fluid state by using liquid-state ^{13}C NMR spectroscopy [14]. Such a discrepancy must be due to the fact that only a small fraction of the most mobile species, presumable small unilamellar vesicles, can be observed without applying solid state NMR techniques like magic-angle spinning and dipolar decoupling. The small size of the lipid domain may indeed result in modification of the conformer populations, both in the gel and the liquid-crystalline phase. On the contrary, using magic-angle spinning and dipolar decoupling techniques, each leading to efficient suppressing of inherent spectral broadening present in the absence of a rapid isotropic molecular tumbling, a common situation in lipid membranes even in the fluid phase, one can record fully representative ^{13}C spectra, whatever the size of liposome species.

There appears to be so far no data concerning the *trans–gauche* energy difference in the gel and liquid crystalline phase of phospholipids. The energy of the *gauche* conformations relative to *trans* can be described by a Bolzmann relationship

$$n_g/n_t = A \exp(-\Delta E/RT) \qquad (3)$$

where E is the energy difference and $n_{g,t}$ is the number of *gauche* or *trans* conformations.

The double degeneracy of the gauche states leads to a value of 2 for a pre-exponential factor A assuming unrestricted conformational equilibrium of the acyl chains. Since $f_g = n_g/(n_g + n_t)$, we obtain

$$n_g/n_t = f_g/(1 - f_g) = A \exp(-\Delta E/RT) \quad (4)$$

The average energy difference ΔE between *trans* and *gauche* states can be therefore determined from a value of f_g. The calculated average value of the energy difference for the central C4-11 fragment of DMPC is equal to 9.52 ± 0.4 kJ mol^{-1} and 4.02 ± 0.2 kJ mol^{-1} for the gel and liquid crystalline phase, respectively. The latter value is in good agreement with the range of values (2 – 5 kJ mol^{-1}) found experimentally and from molecular simulations in n-alkanes, paraffins and polyethylene in solution or melt states [15-18].

Fig. 4.3 illustrates the peak-fitting deconvolution analysis of resonances from the central fragment of the acyl chain encompassing the carbons C4-11 in the ^{13}C MAS spectra of DMPC/DMPE mixture of liposomes recorded at different temperatures.

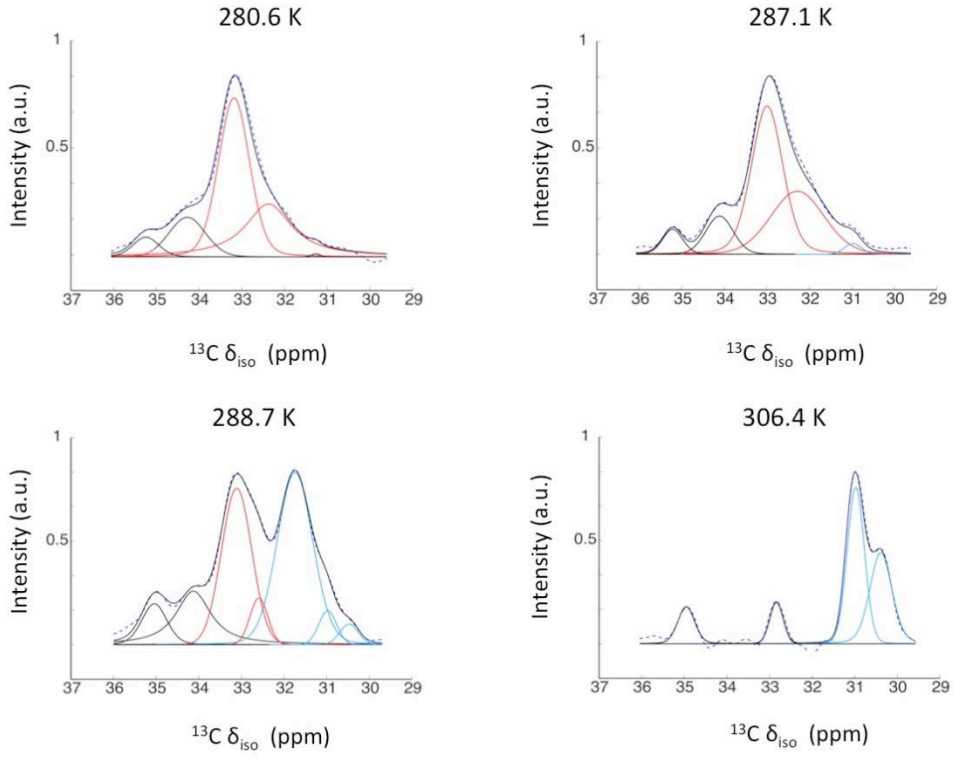

Figure 4.3 : The same as in Fig. 4.2 for ^{13}C MAS spectra of DMPC/DMPE mixture

Noticeably, the resonance signals from the liquid-crystalline phase of this mixture are already present in the spectrum recorded at 288.7 K while such resonances were still absent at 295 K for pure DMPC liposomes (see. 4.2). This is due to a lower melting temperature for the DMPC/DMPE sample (*vide infra*).

Similarly to the DMPC sample, all resonances, except from the α carbon, show a high-field shift with increasing temperature related to the increasing population of *gauche* conformations. However, the calculated average value of the energy difference for the central C4-11 fragment in the liquid crystalline phase is now estimated to be 2.47 ± 0.7 kJ mol^{-1} while for the gel state remains unchanged. This suggests higher later disorder of the acyl chains in the fluid phase of this mixture, which is again corroborated by a lower melting temperature, discussed below.

4.3.2 Revealing chain melting temperature (T_m)

In the gel state, the acyl chains are fully extended and are aligned nearly perpendicular to the plain of the bilayer. Both intra-and intermolecular motions are highly restricted, leading to short- and long-range order within the gelled lipid bilayer and its highly impermeable structure. In contrast, in the liquid-crystalline phase, due to enhanced mobility of the acyl chains, the effective cross-sectional area per phospholipid molecule increases and the bilayer thickness decreases rending the liquid crystalline bilayer permeable [1].

The changes of the normalized amount of magnetization from the central C4-11 carbons (integrated intensity of relevant resonances ranging between 33.3 and 30.6 ppm for DMPC and between 33.1 and 30.4 ppm for DMPC/DMPE as retrieved from the peak-fitting deconvolution analysis) at temperatures encompassing the gel to liquid-crystalline phase transition are shown in Fig. 4.4 for DMPC (left) and DMPC/DMPC (right) samples. In both cases the intensity of the resonance signals around 33 ppm rapidly decreases while that from peaks close to 31 ppm is rapidly growing.

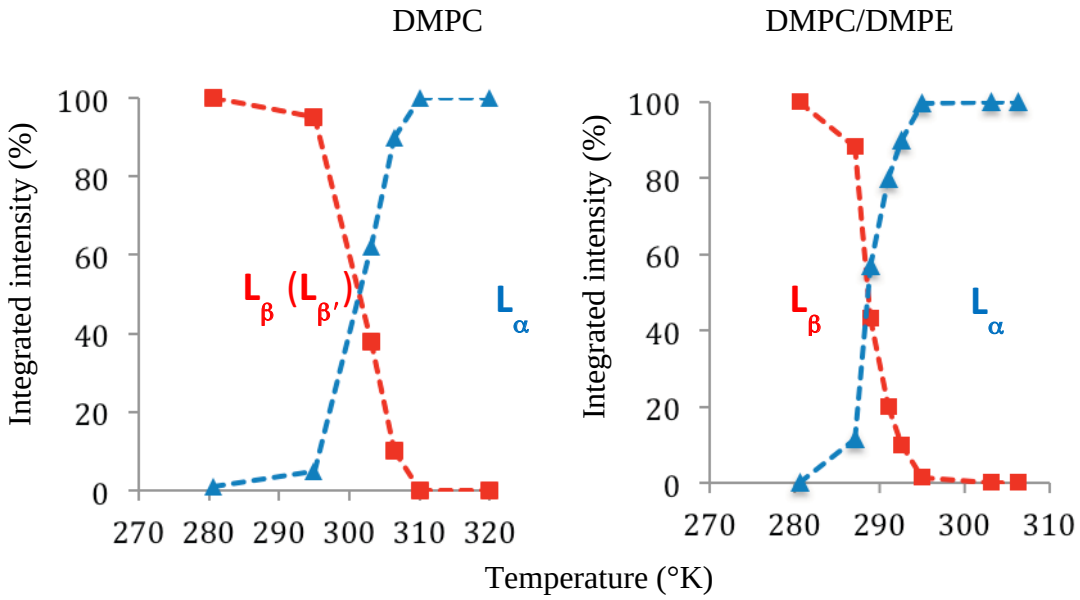

Figure 4.4: Integrated intensity of resonance signals from the central fragment of the acyl chain in the gel phase (red squares) and liquid-crystalline phase (blue tringles) for DMPC (left) and DMPC/DMPE mixture (right).

The comparison of both graphs reveals immediately two striking differences, i.e. a sharper temperature range between an onset and end temperature of chain melting and its significantly lower midpoint T_m temperature for the DMPC/DMPE sample. In single phospholipid-water systems having identical acyl chains and polar head groups, the phase transitions are expected indeed to be sharp [1]. Larger range of temperatures encompassing the melting region in DMPC as compared with its mixture with DMPE could suggest the presence of pre-transition preceding the main transition. This could be due to the presence of a mixed phase composed of the gel (L_{β}) and ripple ($L_{\beta'}$) phases [8]. For the DMPC liposomes, the middle position of magnetization change during the transition from the gel to the liquid-crystalline phase is located close to 300 K that is indeed a commonly observed temperature for DMPC chain melting at high hydration levels [1]. Somewhat unexpectedly, for the DMPC/DMPE mixture, the midpoint temperature of this transition is very close to 290 K. Such a striking decrease of T_m could be due to a smaller size of the polar group in DMPE lipids as compared with DMPC, resulting in higher structural inhomogeneity of the DMPC/DMPE liposomes.

This appears indeed conceivable remembering that the structure of phospholipid assemblies depends to a large extent on the nature of the phospholipid head group, its relative size with respect to the cross-sectional area of hydrocarbon chains, and its propensity to form lateral interactions [7].

The presence of other molecules like cholesterol, proteins and peptides may affect the main thermotropic transition by altering the packing of the fatty acid chains and the conformer populations in both phases. Solid-state NMR spectroscopy is one of the most efficient methods to obtain structural and dynamic information on membrane proteins and other membrane associated molecules [19, 20]. Recently introduced rotational alignment NMR approach permits to determine the structure of membrane proteins in phospholipid bilayers under physiological conditions [21]. For this it is important that the bilayers are in the liquid crystalline phase permitting fast rotational diffusion of membrane proteins about the bilayer normal. As shown in Fig. 4.5, this requirement can be easily controlled during the ^{13}C MAS NMR experiments through the inspection of isotropic chemical shift of natural abundance ^{13}C resonances from the central fragment of the acyl chains in phospholipid bilayers.

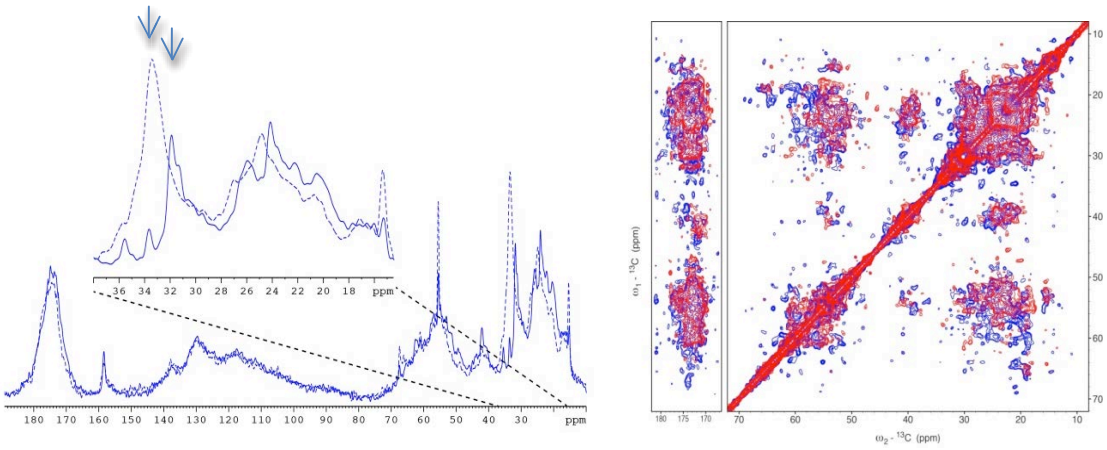

Figure 4.5:1D ^{13}C (left) and 2D ^{13}C-^{13}C (right) MAS spectra of U-^{13}C, ^{15}N labeled TSPO membrane protein reconstituted in natural abundance DMPC/DMPE mixture with(blue) and without (red) PK11195 ligand. The 1D spectra were recorded at 10°C (dashed line) and 30°C (continuous line). Note characteristic shift of resonances (highlighted by arrows) from the central fragment of the acyl chains due to the gel – liquid-crystalline phase transition. Both 2D correlation spectra were recorded at 25°C with enhanced intensity using PARIS irradiation [22] as described in chapter 2.

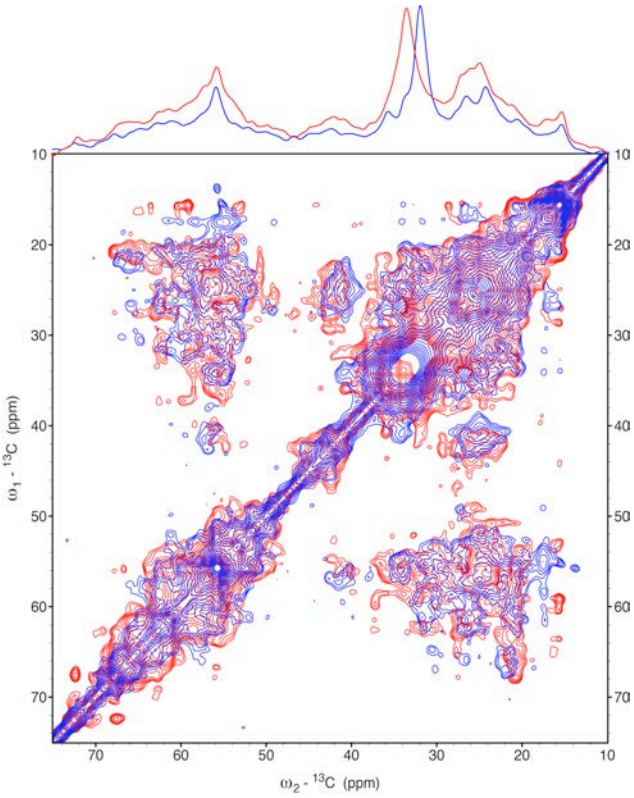

Figure 4.6 : 2D PARIS spectra with NOE enhancement at 10°C (red) and 30 °C (blue) both with ligand.

4.3.3 Conclusions

We have shown that the changes of the isotropic chemical shifts of the acyl chain carbons revealed in natural abundance ^{13}C MAS NMR spectra appear to be a sensitive probe of the gel to liquid-crystalline phase transition and relevant conformation changes. The data reveal that during the chain melting the formation of *gauche* conformers and the decrease the energy differences between *gauche* and *trans* conformers is favored in the middle of the acyl chains. The average value of the energy difference between *trans* and *gauche* states in the central C4-11 fragment of fatty acyl chain in the liquid crystalline state drops from 4.02 ± 0.2 kJ mol^{-1} for pure DMPC liposomes to 2.47 ± 0.7 kJ mol^{-1} in DMPC/DMPE mixture. Smaller size of polar group for DMPE may induce structural inhomogeneity of DMPC/DMPE liposomes and promote chain melting at lower temperature as compared with pure DMPC liposomes. We believe that the observed shifts of resonances from the central part of acyl chain can be useful for a straightforward monitoring of effective transition from the gel to liquid-crystalline phase required for activation of rapid uniaxial rotation of the membrane proteins.

4.4 References

1. Marsh, D., Handbook of Lipid Bilayers, Second Edition, in *Handbook of Lipid Bilayers, Second Edition*. 2013, CRC Press.
2. Aloia, R.C., Membrane fluidity in biology. 1, 1. 1983, New York u.a.: Acad. Pr.
3. Seelig, A. and J. Seelig, *Biochemistry* 1974, 13 (23), 4839-4845.
4. Davis, J.H., *Biochimica et Biophysica Acta (BBA) - Reviews on Biomembranes* 1983, 737 (1), 117-171.
5. Watts, A. and P.J.R. Spooner, *Chem. Phys. Lipids* 1991, 57 (2–3), 195-211.
6. Mackay, A.L., *Biophys. J.* 1981, 35 (2), 301-313.
7. Bruzik, K.S. and J.S. Harwood, *J. Am. Chem. Soc.* 1997, 119 (28), 6629-6637.
8. Nomura, K., M. Lintuluoto, and K. Morigaki, *J. Phys. Chem. B* 2011, 115 (50), 14991-15001.
9. Kóta, Z., M. Debreczeny, and B. Szalontai, *Biospectroscopy* 1999, 5 (3), 169-178.
10. Lacapere, J.-J., S. Iatmanen-Harbi, L. Senicourt, O. Lequin, P. Tekely, R.N. Purusottam, P. Hellwig, S. Kriegel, S. Ravaud, C. Juillan-Binard, E.P. Peyroula, and V. Papadopoulos, Structural Studies of TSPO, a Mitochondrial Membrane Protein, in *Membrane Proteins Production for Structural Analysis*, I. Mus-Veteau, Editor. 2014, Springer New York. p. 393-421.
11. Potrzebowski, M.J., P. Tekely, and Y. Dusausoy, *Solid State Nucl. Magn. Reson.* 1998, 11 (3–4), 253-257.
12. Purusottam, R.N., G. Bodenhausen, and P. Tekely, *J. Magn. Reson.* 2014, 246 (0), 69-71.
13. Massiot, D., F. Fayon, M. Capron, I. King, S. Le Calvé, B. Alonso, J.-O. Durand, B. Bujoli, Z. Gan, and G. Hoatson, *Magn. Reson. Chem.* 2002, 40 (1), 70-76.
14. Brainard, J.R., R.D. Knapp, J.D. Morrisett, and H.J. Pownall, *J. Biol. Chem.* 1984, 259 (16), 10340-10347.
15. Colombo, L. and G. Zerbi, *J. Chem. Phys* 1980, 73 (4), 2013-2014.
16. Darsey, J.A. and B.K. Rao, *Macromolecules* 1981, 14 (5), 1575-1581.
17. Yamanobe, T., T. Sorita, I. Ando, and H. Sato, *Die Makromolekulare Chemie* 1985, 186 (10), 2071-2078.
18. Smith, G.D. and R.L. Jaffe, *The Journal of Physical Chemistry* 1996, 100 (48), 18718-18724.
19. Mcdermott, A., *Annu. Rev. Biophys.* 2009, 38 (1), 385-403.
20. Smith, S.O. and O.B. Peersen, *Annu. Rev. Biophys. Biomol. Struct.* 1992, 21 (1), 25-47.
21. Park, S.H., B.B. Das, A.A. De Angelis, M. Scrima, and S.J. Opella, *J. Phys. Chem. B* 2010, 114 (44), 13995-14003.
22. Weingarth, M., D.E. Demco, G. Bodenhausen, and P. Tekely, *Chem. Phys. Lett.* 2009, 469 (4–6), 342-348.

5 Determination of sample temperature in unstable static fields by combining solid state ^{79}Br and ^{13}C NMR

5.1 Introduction

Accurate temperature control during NMR experiments is a prerequisite for dynamic and structural investigations. This requirement is particularly challenging in high-resolution solid-state spectroscopy with magic angle spinning (MAS) when employing high gas flow rates for driving and bearing, with a separate flow to control of the temperature. High-power radio-frequency (rf) irradiation and friction can lead to significant heating of the sample that variable-temperature control units fail to monitor accurately.

Several approaches for determining the sample temperatures in solid-state NMR experiments have been reported. NMR thermometers can exploit the temperature dependence of the isotropic chemical shifts of specific compounds containing ^{13}C [1-3], ^{15}N [4], ^{31}P [5, 6] , ^{119}Sn [7-9] , ^{207}Pb [10-12] and ^{1}H [13, 14]. Very recently, spin-lattice relaxation rates of ^{79}Br in KBr powder have been exploited, in addition to chemical shifts, for the determination of the sample temperature under magic-angle spinning conditions over a wide temperature range from 20 to 320 K [15].

Monitoring the isotropic chemical shifts to calibrate the sample temperature presupposes a perfect stability of the static magnetic field. It can be difficult to satisfy this requirement in solid-state NMR measurements. Solid-state NMR probes typically do not incorporate any field-frequency lock. Apart from the inherent slow drifts of the static field, a significant instability of B_0, on time-scales between a few tens of minutes and hours, is indeed commonly observed after inserting a solid-state NMR probe into a magnet and setting the relevant shim currents, or indeed after changing the target temperature. This is illustrated in fig. 5.1 showing the temporal evolution of the isotropic ^{13}C chemical shift for CH carbon of adamantane after changing the target temperature to 250 K.

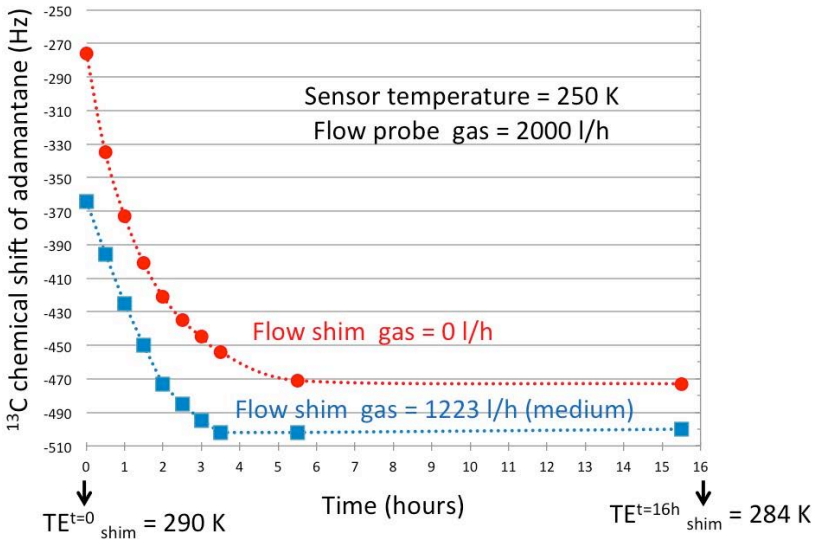

Figure 5.1: Temporal evolution of the isotropic ^{13}C chemical shift due to a drift of the static field B_0 after setting the target temperature to 250 K for a 3.2 mm probe and recorded for the CH carbon of adamantane at 800 MHz Bruker spectrometer.

In this chapter we describe a simple approach to compensate for the effects of for the effects of unstable static fields that can mask the temperature dependence of ^{79}Br isotropic chemical shifts is described. Since KBr has only one isotropic ^{79}Br resonance line flanked by a family of spinning sidebands, a single spectrum cannot provide a conclusive proof that the observed shift is purely induced by temperature. To overcome this problem, a ^{13}C resonance signal from adamantane mixed with KBr was used to monitor any change of the external magnetic field B_0. Adamantane molecules freely rotate in a cubic phase between 208 and 543 K and both their ^{13}C chemical shifts appear to be insensitive to temperature, at least over the range probed in this work. Both KBr and adamantane in natural abundance provide strong signals and the difference between the ^{79}Br and ^{13}C resonance frequencies is only about 0.4 %. Thus one can record both resonances in two consecutive single-pulse experiments within a few seconds without the need to retune the NMR probe.

5.2 Materials and methods

The experiments were conducted at two static fields using a Bruker 800 MHz wide-bore spectrometer equipped with a 3.2 mm E-free MAS probe and a Bruker 400 MHz wide-bore spectrometer equipped with 1.3, 2.5 and 4.0 mm MAS probes. The ^{79}Br and ^{13}C spectra were acquired using four scans each with a recovery interval of 1.0 and 4.0 s, respectively. No decoupling was applied for recording ^{79}Br spectra of KBr while low-power PISSARRO decoupling [16] was used during the acquisition of ^{13}C spectra of adamantane.

5.3 Results and discussion

Figure 5.2 shows the temperature dependence of the apparent ^{79}Br and ^{13}C chemical shifts recorded at two static fields B_0 = 9.4 T (99.8818 MHz for ^{79}Br, 100.2455 MHz for ^{13}C) and B_0 = 18.8 T (200.4446 MHz for ^{79}Br, 201.1682 MHz for ^{13}C) using 4.0 and 3.2 mm probes, respectively, and setting both ^{79}Br and ^{13}C chemical shifts arbitrarily to zero at 296 K, referring to Thurber et al [15].

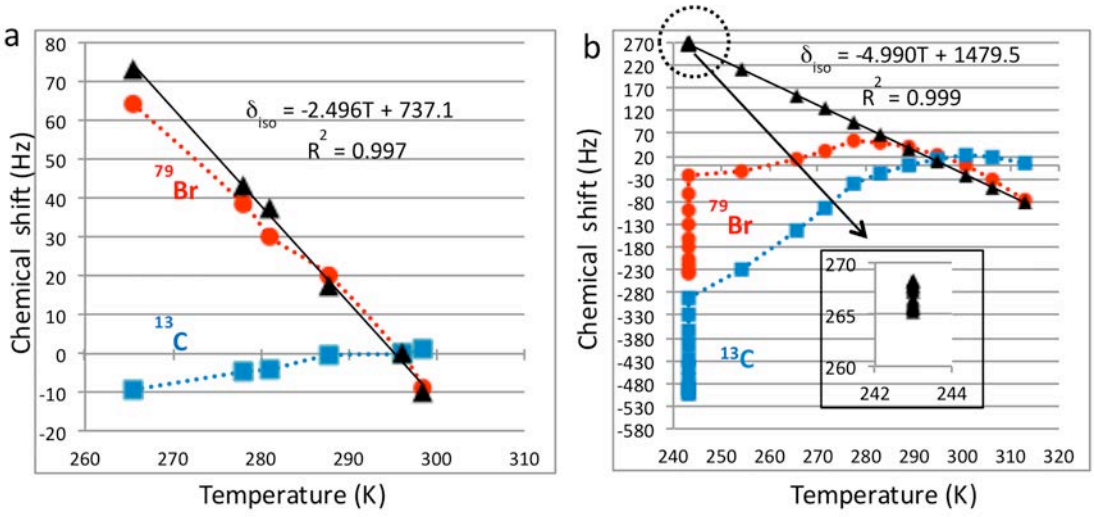

Figure 5.2: Dependence of the apparent isotropic chemical shifts of ^{79}Br (red circles) and ^{13}C (blue squares) of a mixture of KBr and adamantane powders versus temperature recorded in two magnetic fields, and of the corrected isotropic chemical shifts of ^{79}Br (black triangles) adjusted for field changes determined from the ^{13}C shifts: (a) B_0 = 9.4 using a 4.0 mm probe with a spinning frequency ν_{rot} = 7 kHz and (b) B_0 = 18.8 T using a 3.2 mm probe and ν_{rot} = 2 kHz. The flow of the variable temperature gas was 2000 l/h in both cases. At 18.8 T, ten spectra of both ^{13}C and ^{79}Br were recorded on a time scale lasting from 30 min up to 10 hours after the lowest temperature of 243 K became stable.

In each case, for decreasing temperatures, the single-pulse experiments were started only when the temperature reading of the temperature controller had been stable for at least 20 min. A roughly linear down-field shift of the ^{79}Br signal is observed initially in both magnets when decreasing the temperature. The ^{13}C lines of adamantane reveal small but significant up-field shifts at B_0 = 9.4, and down-field shift at 18.8 T. Quite unexpectedly however, a striking reversal of the trends of both ^{79}Br and ^{13}C chemical shifts was observed at 18.8 T below 290 K. This, at first glance was puzzling, apparent reversal of the direction of the ^{79}Br chemical shift can be attributed to the change of the static field. This must be due to a progressive cooling of the shim coils, which appears to lag behind the cooling of the probe. To separate the temperature dependence of ^{79}Br chemical shift from their field dependence, it suffices to subtract the latter's contribution monitored through the ^{13}C resonance. As shown in Fig. 5.2 this permits to recover an unequivocal linear temperature dependence of the ^{79}Br chemical shift [14]. A least-squares analysis of the data yields the same slope -0.025 ± 0.002 ppm/K at both B_0 = 9.4 and 18.8 T, with a correlation coefficients close to 1. It is worth pointing out that in the temperature range probed in this study, the observed drift of B_0 does not lead to any loss of spectral resolution, which would of course hamper monitoring of the chemical shifts. Otherwise, appropriate shimming would be necessary before recording both ^{79}Br and ^{13}C spectra at each temperature. If the use of ^{15}N chemical-shift thermometer from ref. [4] is preferred, it would require to blend it with an another ^{15}N labeled compound provided its chemical shift is not temperature dependent.

Figure 5.3a shows plots of the ^{79}Br chemical shift versus spinning frequency recorded for KBr in rotors with 1.3, 2.5, 3.2 and 4.0 mm diameter without any temperature regulation. In all cases the acquisition was not begun until the ^{79}Br chemical shift had been stabilized. The constant ^{13}C chemical shift of adamantane recorded with a 2.5 mm rotor is also included. An up-field shift of the ^{79}Br resonance may be attributed to increasing frictional heating of the sample with increasing spinning frequencies and can be fitted by using polynomial functions included in the figure. The corresponding frictional heating of the sample shown in Fig. 5.3b for each type of rotor was calculated by using linear fits in Fig.5.2 to convert shifts to temperatures. In the absence of an active temperature control, aprrox. 20% increase in the line-width of the ^{79}Br signal was observed at the highest spinning frequencies employed in this study with different types of rotors.

This is a strong indication of inherent temperature gradients ranging from 3 to 5 °C within fully packed rotors. Increasing the flow of the gas to control the temperature can attenuate these gradients. The precise calibration of temperature gradients within the sample, mandatory for accurate determination of temperature-induced phase transitions and to study the activation of specific motional processes, would require the restriction of the sample to thin, disc-shaped regions, positioned at the center of the rotor and at its bottom and top ends.

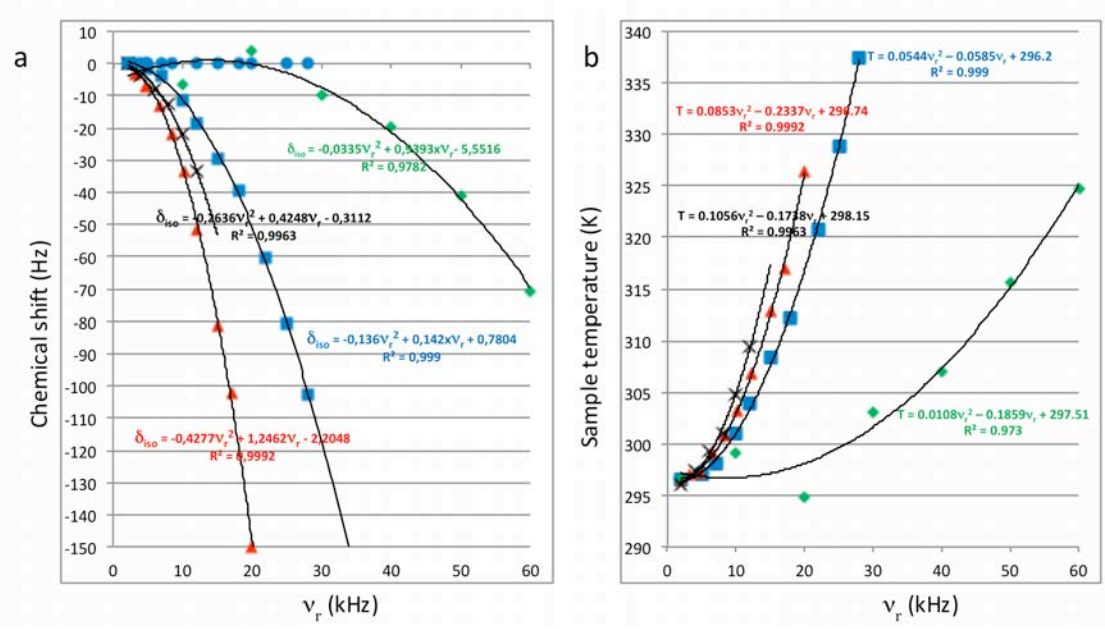

Figure 5.3: (a) Plot of the ^{79}Br chemical shifts versus spinning frequency recorded for KBr using rotors with diameters of 4 mm (black crosses), 3.2 mm (red triangles), 2.5 mm (blue squares) and 1.3 mm (green lozenges). The ^{13}C chemical shifts of adamantane recorded with a 2.5 mm diameter rotor at different spinning frequencies are also shown (blue circles). (b) Frictional heating of the sample for each type of rotor, using the same symbols and colors as in (a). The linear fits shown in Figure 5.2 were used to convert ^{79}Br shifts to temperatures. The flow of the gas was 800 l/h for the 2.5 mm rotor and 2000 l/h for all other rotors.

5.4 Conclusions

A simple blend of KBr and adamantane powders can be used as a reliable chemical-shift thermometer to measure the sample temperature accurately in real time, even in unstable static fields. A simple way was described to determine the accurate temperature dependence of the ^{79}Br resonance after subtracting changes of resonance frequency due to changes of the static field, monitored by the ^{13}C resonance of adamantane.

5.5 References

1. Campbell, G.C., R.C. Crosby, and J.F. Haw, *J. Magn. Reson.* 1986, 69 (1), 191-195.
2. Haw, J.F., R.A. Crook, and R.C. Crosby, *J. Magn. Reson.* 1986, 66 (3), 551-554.
3. Klymachyov, A.N. and N.S. Dalal, *Solid State Nucl. Magn. Reson.* 1996, 7 (2), 127-134.
4. Wehrle, B., F. Aguilar-Parrilla, and H.-H. Limbach, *J. Magn. Reson.* 1990, 87 (3), 584-591.
5. Pan, H. and B.C. Gerstein, *J. Magn. Reson.* 1991, 92 (3), 618-619.
6. Zuo, C.S., K.R. Metz, Y. Sun, and A.D. Sherry, *J. Magn. Reson.* 1998, 133 (1), 53-60.
7. Grey, C.P., A.K. Cheetham, and C.M. Dobson, *J. Magn. Reson. A* 1993, 101 (3), 299-306.
8. Kemp, T.F., G. Balakrishnan, K.J. Pike, M.E. Smith, and R. Dupree, *J. Magn. Reson.* 2010, 204 (1), 169-172.
9. Langer, B., I. Schnell, H.W. Spiess, and A.-R. Grimmer, *J. Magn. Reson.* 1999, 138 (1), 182-186.
10. Bielecki, A. and D.P. Burum, *J. Magn. Reson. A* 1995, 116 (2), 215-220.
11. Isbester, P.K., A. Zalusky, D.H. Lewis, M.C. Douskey, M.J. Pomije, K.R. Mann, and E.J. Munson, *Catal. Today* 1999, 49 (4), 363-375.
12. Takahashi, T., H. Kawashima, H. Sugisawa, and B. Toshihide, *Solid State Nucl. Magn. Reson.* 1999, 15 (2), 119-123.
13. Aliev, A.E. and K.D.M. Harris, *Magn. Reson. Chem.* 1994, 32 (6), 366-369.
14. Dvinskikh, S.V., V. Castro, and D. Sandström, *Magn. Reson. Chem.* 2004, 42 (10), 875-881.
15. Thurber, K.R. and R. Tycko, *J. Magn. Reson.* 2009, 196 (1), 84-87.
16. Weingarth, M., G. Bodenhausen, and P. Tekely, *J. Magn. Reson.* 2009, 199 (2), 238-41.

6 Sensitivity improvement during heteronuclear spin decoupling in solid-state NMR

6.1 Heteronuclear dipolar decoupling in solid state NMR

Achieving high spectral resolution and sensitivity is an essential prerequisite for the application of solid-state nuclear magnetic resonance to large biological systems, such as proteins. Unambiguous assignment of resonances is only feasible if they are well resolved in a multi-dimensional correlation spectrum. Dipolar coupling to the abundant nuclei, heteronuclear dipolar coupling is the principal contributor to the line width of rare spins in solid state. For spinning samples, a reasonable line width is often accomplished by application of radio-frequency (RF) modulation of the abundant spins that suitably manipulate the spin interactions. These modulation schemes are referred to as heteronuclear dipolar decoupling sequences. For several decades until about mid-1990, a continuous burst of high power rf irradiation on the ^{1}H channel called continuous wave (CW) decoupling remained as the most common way to achieve heteronuclear spin decoupling in ssNMR under MAS [1-3]. A major breakthrough was made [4, 5] with the observation that simple modulations of the decoupling irradiation could dramatically improve the performance of the decoupling relative to CW irradiation. This initiated renewed interest in the understanding of the decoupling process in rotating solids and lead to the development of more advanced decoupling sequences, There are many effective heteronuclear dipolar decoupling schemes for the study of these systems. Nevertheless there is a continuous quest for better decoupling schemes that still persists in the literature such as TPPM [5], FMPM [6], SPARC [7], $C12_2^{-1}$ [8], SPINAL [9], XiX [10], eDROOPY [11], PISSARRO [12], SW_f-TPPM [13], rCW [14].

In general the basic parameters that judge the quality of a heteronuclear decoupling scheme can be categorized as follows [15]:

1) ***Decoupling efficiency***: The peak height or full-width at half-height of individual resonance (as normally observed in the direct dimension) is an indicator of the efficiency of decoupling. However, the observed residual line width can be on account of the following [16]: (i) Transverse relaxation due to

incoherent motion, similar to solution-state NMR, (ii) Residual interactions due to incomplete dipolar averaging and (iii) Distribution of chemical shifts, B_0 inhomogeneity, or magnetic susceptibility effects. Whilst the first is negligible in solid-state NMR, the third can be completely refocused with a spin-echo scheme, and the second dominates coherence lifetime in solid-state NMR measurements.

2) ***Robustness to experimental parameters***: The efficiency of a decoupling scheme should be fairly insusceptible of all experimental parameters over the widest range possible. The parameters include the ^{1}H irradiation offset and pulse durations and phases value missets.
3) ***Transverse dephasing times***: Each of the decoupling schemes has different efficiency in averaging out the coherent residuals. This may be observed by measuring the coherence time scales in a spin-echo experiment with a particular decoupling scheme. This effective transverse dephasing time, could be different for various schemes, even if their decoupling efficiency turns out to be similar. This can have consequences in experiments involving spin-echo periods, such as, multidimensional experiments like incredible natural abundance double quantum experiment (INADEQUATE) [17, 18] or REDOR [19] kind of experiments, which involves repeated application of π-pulses.
4) ***Ease of optimization***: This is one of the most important parameters for the routine implementation of a good decoupling scheme. The main issue is whether a decoupling scheme can be suggested with the fewest parameters to be optimized or rule of thumb guidelines and applicable for a wide range of experimental as well as sample conditions.

The efficiency of the classical method, CW scheme, deteriorates with MAS frequency and it becomes largely ineffective at higher MAS frequencies, $\nu_r \geq 15$ kHz. TPPM delivers resolution enhancement over CW scheme by a factor of two and the resulting linewidth remains unaffected with MAS frequency. The optimum performance under TPPM scheme is realised after careful optimisation of experimental parameters. Thus, its implementation is demanding. Taking TPPM as the building block and incorporating phase modulation over it, the SPINAL scheme

was designed. This method was shown to deliver an enhanced performance over TPPM. XiX scheme was shown to be far superior to TPPM at higher MAS frequencies, $\nu_r > 25$ kHz, but the r.f. field strength required is usually much larger than 100 kHz, making it less useful, especially for heat-sensitive samples.

At high static fields, higher spinning frequencies may be preferred to prevent residual spinning sidebands and unwanted rotational resonance effects that occur when an integer multiple of the spinning frequency ν_{rot} is roughly matched with the difference $\Delta\nu_{iso}$ between two isotropic chemical shifts ($n\nu_{rot} = \Delta\nu_{iso}$) [20]. This may lead to harmful line broadening or to undesirable magnetization exchange between specific sites. High spinning frequencies may also be useful at high static fields to create optimal conditions for broadband magnetization exchange in two-dimensional homonuclear correlation experiments [21]. Other indirect benefits of high spinning frequencies are related to the use of small-diameter rotors that allow one to run experiments with less than 1 mg powder sample. However, spinning frequencies around and above 30 kHz may also lead to a dramatic breakdown of the decoupling efficiency over a large range of *rf* amplitudes due to the phenomenon of rotary resonance recoupling (R^3) ($\nu_1 = n\nu_{rot}$) [22]. To overcome this complication, a phase-inverted supercycled sequence for attenuation of rotary resonance (PISSARRO) was developed and shown to be effective in quenching rotary resonance recoupling in the vicinity of $n = 2$ [12]. The method turned out also to achieve a very good decoupling efficiency at high *rf* amplitudes, far from any R^3 condition, as well as in the low-amplitude decoupling regime when $\nu_{rot} = 60$ kHz [23]. This is partially related to its capacity to center the modulation sidebands, which arise from the interference between the decoupling irradiation and the modulation of dipolar couplings by MAS [12].

A thorough analysis of the mechanism of quenching of rotary resonance recoupling effects by the PISSARRO scheme has revealed the crucial role of its mirror symmetry segments combined with phase-shifted irradiation [24]. The immunity of PISSARRO decoupling against the offsets of remote protons, their chemical shift anisotropies and second-order cross-terms between dipolar coupling and chemical-shift anisotropy has also been demonstrated [24, 25]. Since the introduction of PISSARRO decoupling, a new class of pulse sequences, so-called refocused continuous-wave (rCW), has been

introduced [14]. Although rCW pulse sequences were so far only used for spinning frequencies up to 20 kHz, it has been suggested that they would also be efficient at high spinning speeds [26]. Independently, an amplitude-modulated XiX irradiation was proposed in the low-amplitude decoupling regime and tested at spinning frequencies of 60 and 90 kHz [27]. The various heteronuclear decoupling schemes employed for analysis in this chapter are shown in fig. 6.

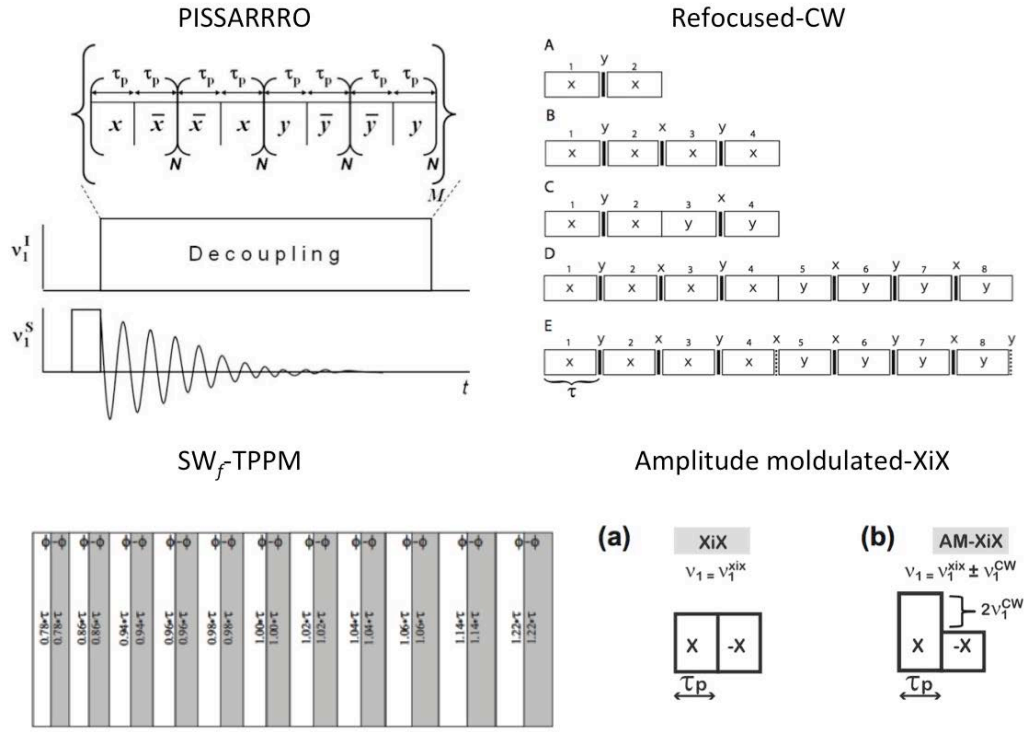

Figure 6: Building blocks of various heteronuclear decoupling schemes.

The building block of PISSARRO comprises of pulse pairs $(\tau_p)_x(\tau_p)_{-x}$ and $(\tau_p)_y(\tau_p)_{-y}$ each of which is repeated N times (typically N = 5, to form a block, and four blocks are combined as shown in fig.4. The refocused CW approach consists of three basic elements: refocusing pulses, phase modulation, and purging pulses. The different variants are constructed by systematically interleaving continuous wave decoupling with appropriately inserted rotor-synchronized high-power π refocusing pulses of alternating phases. The refocusing pulses eliminate residual effects from dipolar coupling in heteronuclear spin systems. In some variants the π pulse refocusing is

supplemented by insertion of rotor-synchronized π/2 purging pulses to further reduce the residual dipolar coupling effects. SW_f-TPPM consists of eleven TPPM pairs with pulse length varied tangentially and can be represented as {$0.78\tau_\varphi$ $0.78\tau_{-\varphi}$} {$0.86\tau_\varphi$ $0.86\tau_{-\varphi}$} {$0.94\tau_\varphi$ $0.94\tau_{-\varphi}$} {$0.96\tau_\varphi$ $0.96\tau_{-\varphi}$} {$0.98\tau_\varphi$ $0.98\tau_{-\varphi}$} {$1.00\tau_\varphi$ $1.00\tau_{-\varphi}$} {$1.02\tau_\varphi$ $1.02\tau_{-\varphi}$} {$1.04\tau_\varphi$ $1.04\tau_{-\varphi}$} {$1.06\tau_\varphi$ $1.06\tau_{-\varphi}$} {$1.14\tau_\varphi$ $1.14\tau_{-\varphi}$} {$1.22\tau_\varphi$ $1.22\tau_{-\varphi}$}. The duration of the central pulse pair (τ) is defined and the tangential frequency sweep is achieved by the multiplicative factor to τ. The basic element of AM-XiX scheme is identical to the XiX sequence, except that the two pulses in the cycle have different amplitudes. Mathematically, two pulses with different amplitudes and 180° out of phase can be described as a XiX sequence with an additional CW component. So, the difference in the amplitude of the two pulses divided by two is considered as the 'CW component'.

In this chapter, it is shown that at high spinning speeds, PISSARRO irradiation has a unique capacity to secure efficient decoupling at commonly used *rf* amplitudes between 80 and 120 kHz and provides significant sensitivity improvements. A comparative analysis of the efficiency of low-amplitude decoupling with decreasing spinning frequencies was done and point out the dependence of decoupling on the *rf* field inhomogeneity of the solenoid coil. For the sake of decoupling performance comparison, SW_f-TPPM [13] decoupling sequence was chosen, which according to recent reports [15], offers improved efficiency over a larger range of *rf* amplitudes and spinning frequencies compared to its popular precursors.

6.2 Experimental: NMR experiments and numerical simulations

Polycrystalline powders of uniformly ^{13}C, ^{15}N-labeled L-histidine hydrochloride monohydrate were used without further purification. All experiments were performed on a 400 MHz Bruker Avance II spectrometer and on a 850 MHz Bruker Avance III spectrometer, both equipped with double resonance CP/MAS probes using rotors with 1.3 mm diameter. For PISSARRO decoupling, only the pulse duration τ_p needs to be optimized in the vicinity of the recommended values, i.e. $\tau_p = 0.2\tau_{rot}$ for decoupling near the $n = 2$ rotary resonance condition, and $\tau_p = 0.9$ or $1.1\tau_{rot}$ for high *rf* amplitudes $\nu_1^H >> 2\nu_{rot}$ [12]. For low-amplitude decoupling, the pulse lengths were optimized so

that the nutation angles $\beta = 2\pi\nu_1\tau$ were in the vicinity of 6π [13]. For routine purposes, the pulse duration τ_p need not be optimized and may be safely fixed to the above-mentioned durations, depending on the spinning frequency and *rf* amplitude. For SW_f-TPPM decoupling [13], optimum nutation angles were found in the range $120° < \beta < 170°$. The phase angle ϕ was optimized between 5° and 20° in steps of 2°. The number of pulse pairs was fixed to 11 and a linear sweep profile was applied. For rCW decoupling, we chose the rCWc version [14] for best performance under our experimental conditions and lower demands on *rf* field strengths. For the refocusing π pulses, an *rf* field amplitude of 220 kHz was used. The optimum, rotor-synchronized continuous wave pulse length, i.e. the delay τ between the refocusing pulses was around 50 µs ($\tau = n\tau_{rot}$, $n \cong 3$). For low-amplitude experiments recorded with the basic AM-XiX scheme [27], the XiX component was found empirically for various MAS frequencies (ν_1^H = 11.9, 10.1, 8.6 kHz υνfor ν_{rot} = 60, 50 and 40 kHz MAS, respectively). The *rf* amplitude of the continuous wave component, as defined in [27], ranged between 2 and 3 kHz. The pulse length was optimized around $\tau_p \cong 5/2\tau_r$. Numerical simulations were carried out with SPINEVOLUTION [28], considering the 5-spin system $C^{\alpha}H^{\alpha}H^{\beta 1}H^{\beta 2}H^{N}$ of L-histidine hydrochloride monohydrate with internuclear distances derived from the crystallographic structure. In each case the pulse durations were optimized numerically in the vicinity of the recommended values.

6.3 Results and discussion

Comparative analysis of latest heteronuclear dipolar decoupling schemes at fast spinning frequencies

Searching for optimal conditions during one- and multi-dimensional solid-state NMR experiments in high static fields may require spinning the sample at frequencies above 40 kHz. This implies challenging requirements for heteronuclear spin decoupling that is of prime importance to obtain high-resolution NMR spectra of organic molecules and materials. This section of the chapter presents a comparative experimental investigation of the performance of the latest heteronuclear decoupling schemes PISSARRO [12], SW_f-TPPM [13], rCWc [14] and AM-XiX [27] at high magic-angle spinning frequencies and different static fields. The results demonstrate that at

commonly used *rf* amplitudes between 80 and 120 kHz, PISSARRO decoupling provides a substantial sensitivity improvement. This is due to its so far unique capacity to quench efficiently rotary resonance recoupling near the $n = 2$ condition, where the *rf* amplitude approaches twice the spinning frequency. This also allows a substantial reduction of the *rf* power dissipation, which may be vital for heat-sensitive samples. The performance of low-amplitude decoupling at different spinning speeds is also compared and its dependence on the inherent inhomogeneity of the *rf* field is probed by numerical simulations.

The performance of PISSARRO, SW_f-TPPM and rCWc at $\nu_{rot} = 40$ and 60 kHz in a medium static magnetic field ($B_0 = 9.7$ T) was compared in Figs. 6.1 and 6.2 for all carbon-13 resonances of L-histidine.

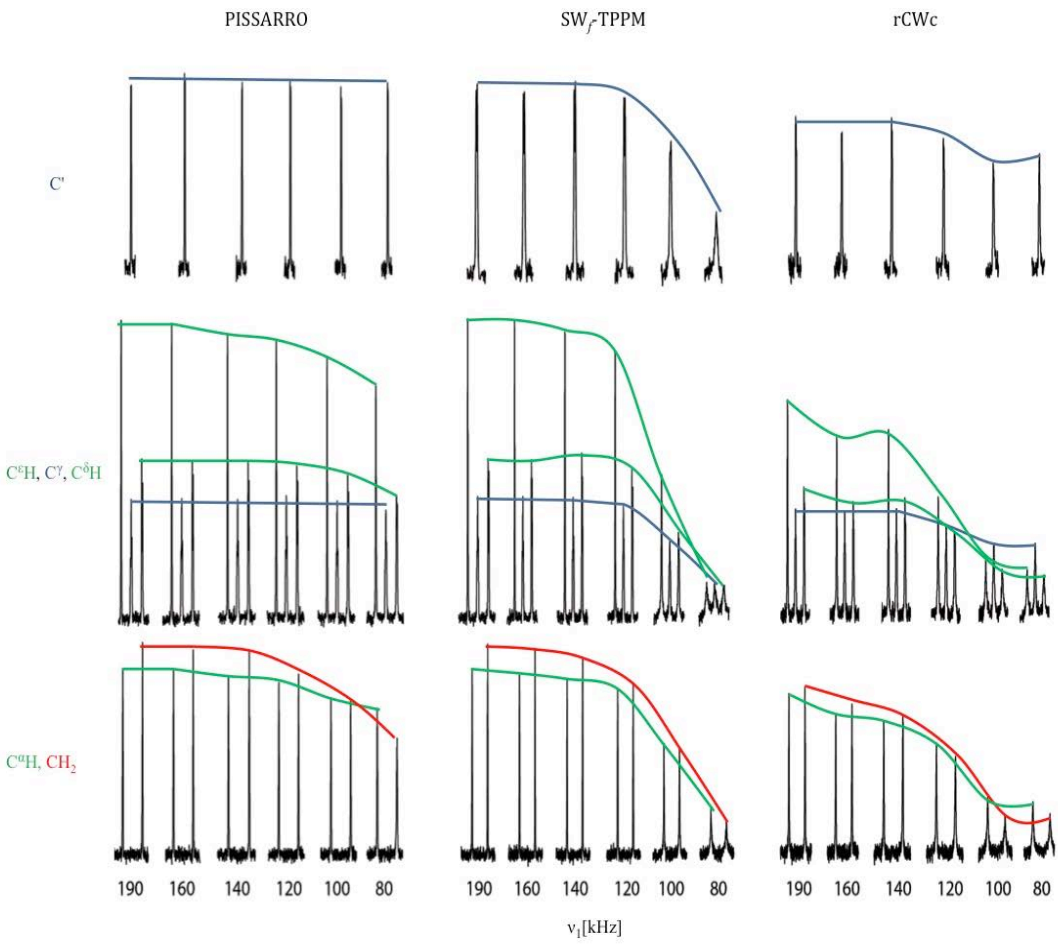

Figure 6.1: Comparison of the efficiency of heteronuclear decoupling for different carbons in L-histidine with PISSARRO (left), SW_f-TPPM (middle) and rCWc (right) at $B_0 = 9.7$ T (400 MHz for protons) and $\nu_{rot} = 40$ kHz as a function of the decoupling *rf* amplitude $190 > \nu_1 > 80$ kHz with the ^{1}H

carrier frequency placed on-resonance for $C^{\alpha}H$. All spectra were recorded with 3.0 ms CP contact time, 8 scans and a 5 s recovery delay between experiments.

A wide range of *rf* decoupling amplitudes 190 > ν_1^H > 80 kHz was tested. For 40 kHz MAS and high *rf* amplitudes between 190 and 120 kHz, PISSARRO and SW_f-TPPM offer very similar performance, while a drop of 42, 30 and 15 % in the peak heights of CH_2, C^aH and non-protonated carbons, respectively, was observed for rCWc. In contrast to PISSARRO, other two methods show a significant drop of performance for ν_1^H < 120 kHz. This drop is greatly amplified at ν_{rot} = 60 kHz due to the destructive interference near the n = 2 rotary resonance condition.

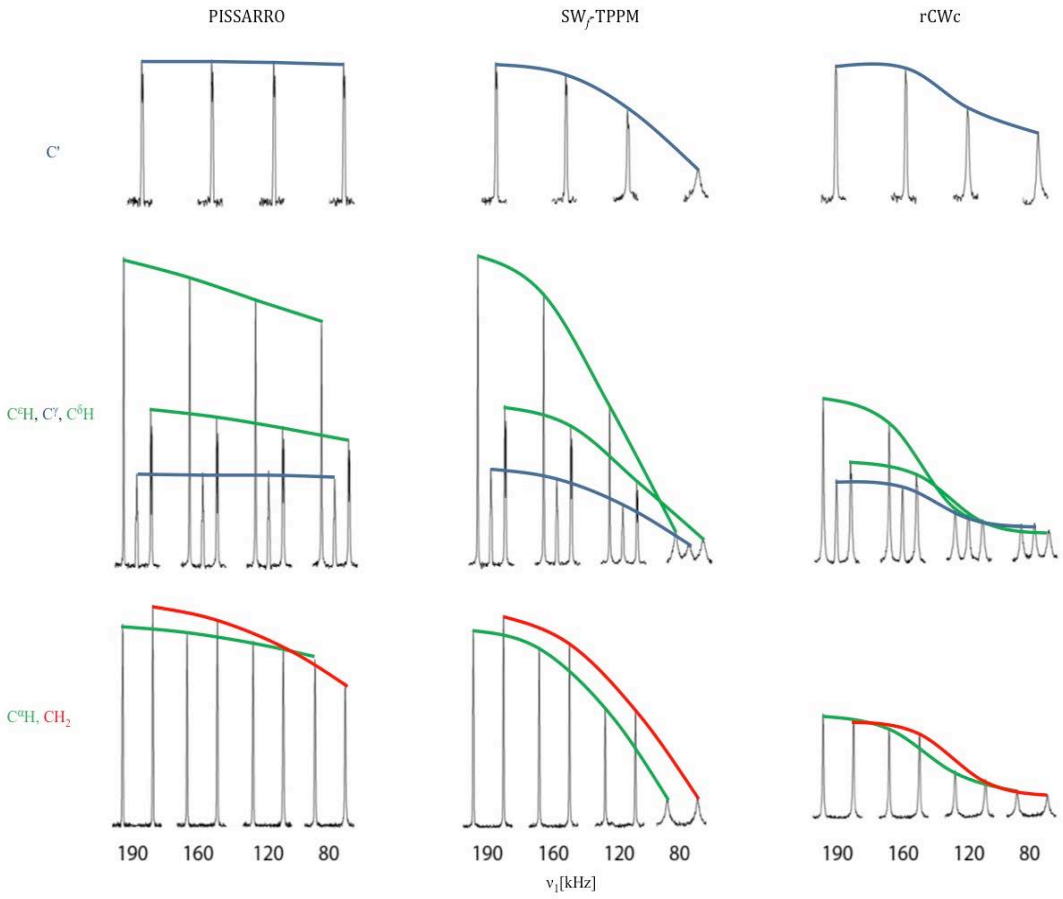

Figure 6.2: Same as in Fig. 6.1 except that ν_{rot} = 60 kHz.

Although somewhat better decoupling near ν_{rot} = 60 kHz can be achieved with high-phase TPPM [29] than with SW_f-TPPM , the peak heights are only about 60 to 80 % of those obtained with PISSARRO.

In ^{13}C spectra of organic solids recorded at high spinning frequencies and very high *rf* decoupling amplitudes, the observed line widths are often not only determined by the performance of decoupling, but may be governed by the inhomogeneous distribution of isotropic chemical shifts and, to a lesser extent, by magnetic susceptibility, dynamic effects and by minor instrumental misadjustments. By combining heteronuclear decoupling with spin echoes, one can determine the residual homogeneous line width (also known as 'refocused line width' characterized by the time constant T_2') that is relevant for many multipulse and multidimensional experiments [30, 31]. To check to what extent T_2' is affected by the *rf* amplitude, we measured the echo decays of $^{13}C^{\varepsilon}H$, which is not involved in homonuclear J_{CC} couplings and has an inhomogeneous line width $\delta H^*_{1/2}$ = 52.6 Hz at ν_1^H = 160 kHz. As shown in Fig. 6.3, a significant drop of T_2' is observed with SW_f-TPPM when decreasing the *rf* amplitude. For ν_1^H = 160, 120 and 80 kHz, we measured T_2' = 66.7, 26.3 and 8.7 ms, respectively. This translates into homogeneous line widths at half-height $\delta H'_{1/2}$ = 4.8, 12.1 and 36.6 Hz. In contrast, the lifetimes measured with PISSARRO are largely independent of ν_1^H (T_2' = 43.5, 41.7 and 37.0 ms for ν_1^H = 160, 120 and 80 kHz, respectively). The corresponding homogeneous line widths are now $\delta H'_{1/2}$= 7.3, 7.6 and 8.6 Hz. This provides satisfactory sensitivity without resorting to high *rf* amplitude.

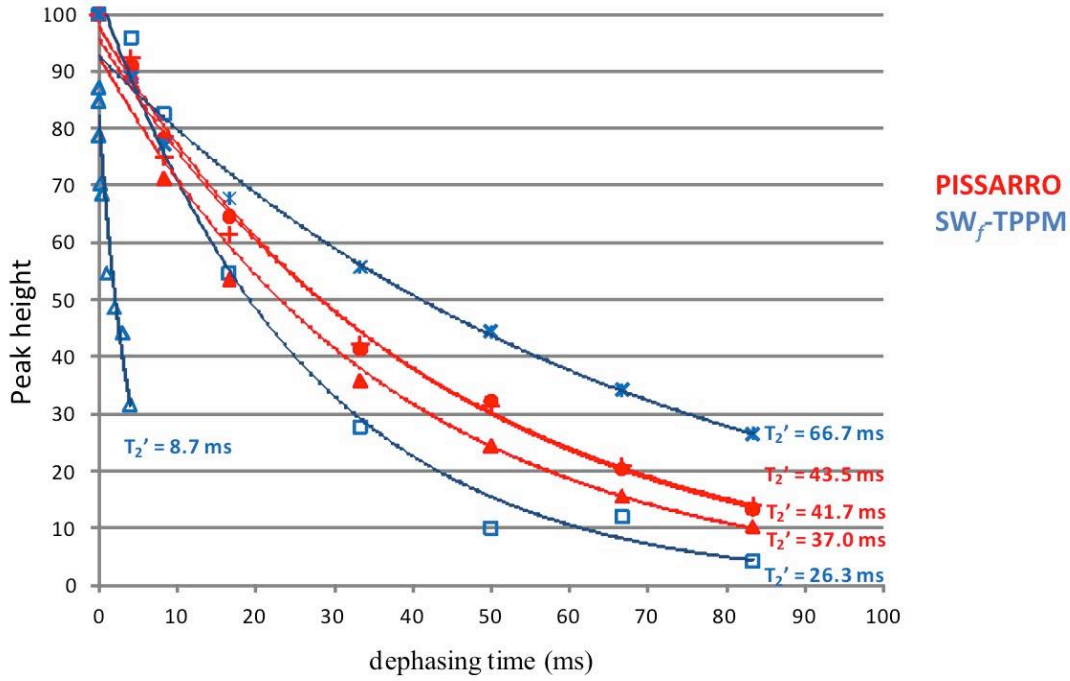

Figure 6.3: The transverse dephasing curves for $C^{\varepsilon}H$ carbon of L-histidine obtained using the spin-echo acquisition procedure at B_0 = 9.7 T and ν_{rot} = 60 kHz. SW$_f$-TPPM pulse sequence was used with a *rf* decoupling amplitude of 160 (*), 120 (□) and 80 kHz (Δ). The T_2' relaxation times are respectively 66.7, 26.3 and 8.7 ms. are The data for PISSARRO at the same *rf* amplitudes are represented by red symbols (+, • and ▲) and the corresponding T_2' values are 43.5, 41.7 and 37.0 ms.

Figure 6.4 shows the decoupling efficiency of PISSARRO, SW$_f$-TPPM and rCWc in high static magnetic field (B_0 = 19.9 T, or 800 MHz for protons) and ν_{rot} = 60 kHz. Similar changes in decoupling performance as a function of ν_1^H as observed at low field (Fig. 6.2) occur, except that the efficiency of SW$_f$-TPPM is somewhat improved near the n = 2 rotary resonance condition.

The data corroborate a substantial sensitivity improvement with PISSARRO decoupling for commonly used *rf* amplitudes $80 < \nu_1^H < 120$ kHz over a wide range of static fields. This will help in high MAS experiments aimed to enhance the sensitivity, e.g., by promoting uniform Overhauser enhancements in ^{13}C NMR spectra of microcrystalline proteins [32].

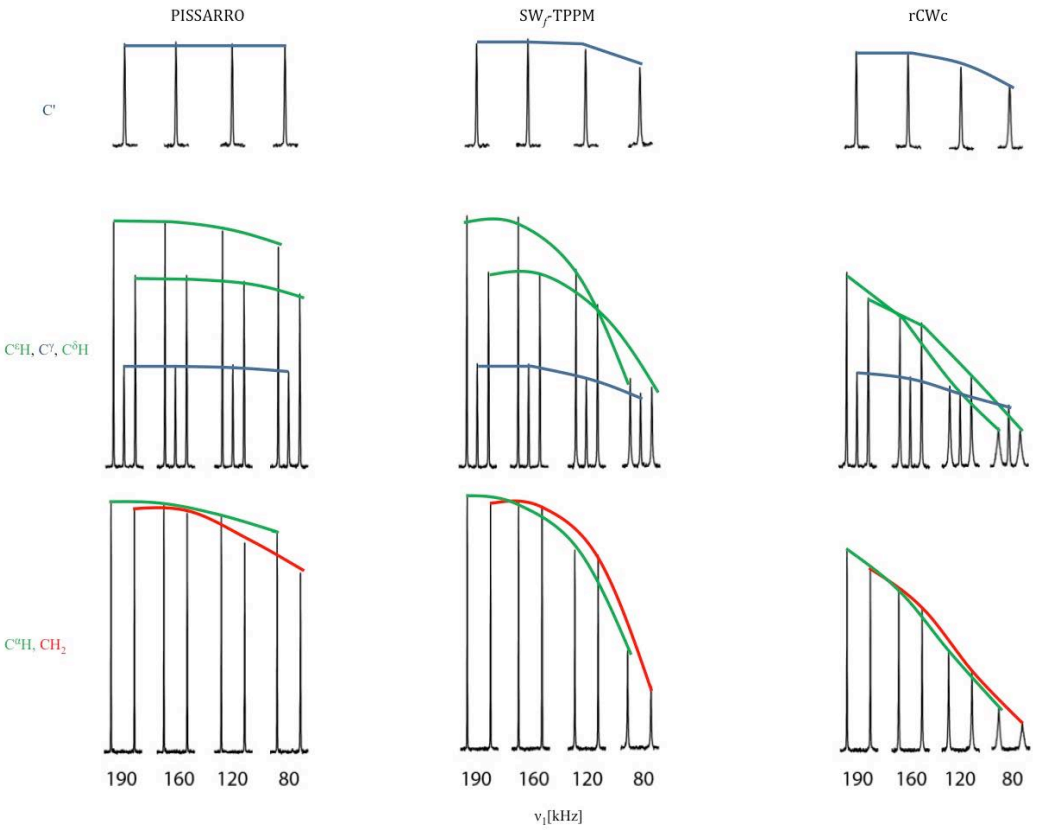

Figure 6.4: Comparison of the efficiency of heteronuclear decoupling for different carbons in L-histidine with PISSARRO (left), SW$_f$- TPPM (middle) and rCWc (right) at B_0 = 19.9 T (850 MHz for protons) and ν_{rot} = 60 kHz as a function of the decoupling *rf* amplitude. All spectra were recorded with a 1.3 ms CP contact time, pre-saturation of ^{1}H during 15.0 ms, NS = 8 and 5 s delay between experiments.

Heteronuclear spin decoupling can also be efficient in a low *rf* amplitude regime with ν_1^H < 30 kHz provided that ν_{rot} > 40 kHz [33 25-27]. It has been demonstrated earlier that at ν_{rot} = 60 kHz in a very high magnetic field B_0 = 21 T (900 MHz for protons), PISSARRO decoupling with ν_1^H = 15 kHz has nearly the same efficiency as with ν_1^H = 150 kHz for both CH_3 and CH resonances in alanine, while the peak height of CH_2 in glycine was 20 % lower.

The comparison of peak heights shown in Fig. 6.5 for L-histidine recorded at B_0 = 19.9 T and ν_{rot} = 60 kHz in the high- and low- amplitude decoupling regimes reveals similar losses for various decoupling scheme.

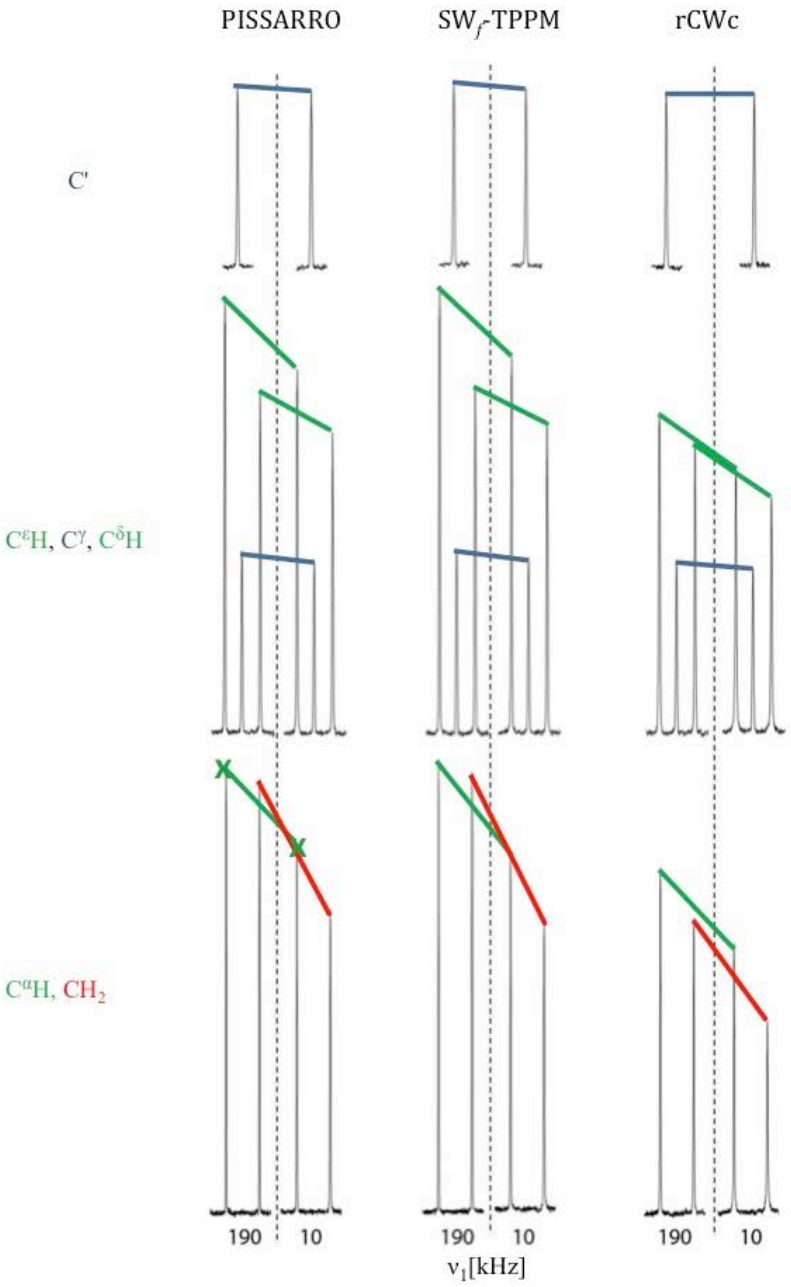

Figure 6.5: Comparison of the efficiency of heteronuclear decoupling for different carbons in L-histidine with PISSARRO (left), SW$_f$ - TPPM (middle) and rCWc (right) at B_0 = 19.9 T and ν_{rot} = 60 kHz in high- and low-amplitude decoupling regime. All spectra were recorded with a 1.3 ms CP contact time, pre-saturation of ^{1}H during 15.0 ms, NS = 8 and 5 s delay between experiments.

For the sake of completeness, Fig. 6.6 shows the peak heights of L-histidine recorded with PISSARRO, SW$_f$-TPPM and AM-XiX in the low amplitude regime ($10 < \nu_1^H <$ 11 kHz) at B_0 = 9.7 T and at three spinning frequencies. The performance is nearly

the same for all three pulse sequences, though slightly better for PISSARRO at ν_{rot} = 40 kHz. More importantly, the observed loss of peak heights at lower spinning frequencies compels one to resort to *rf* amplitudes in the range of $80 < \nu_1^H < 100$ kHz where PISSARRO offers the best efficiency among current decoupling schemes.

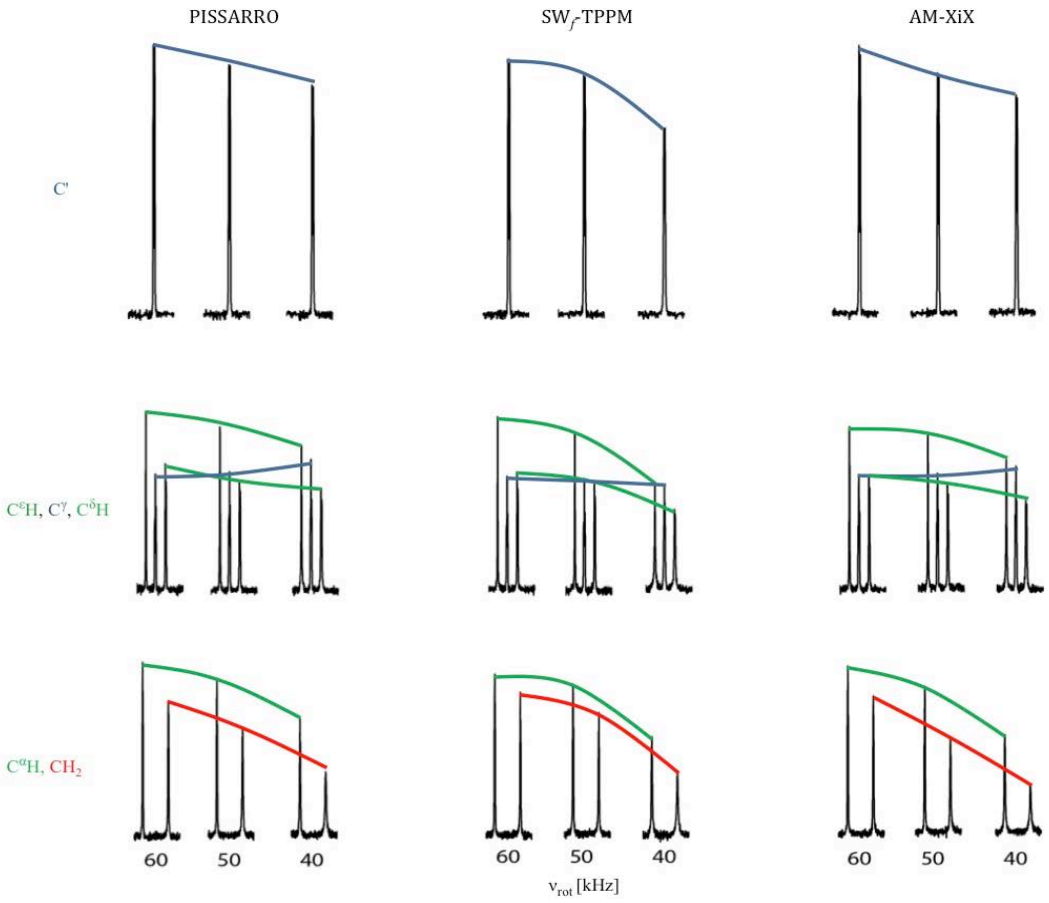

Figure 6.6: Comparison of the efficiency of low-amplitude heteronuclear decoupling for different carbons in L-histidine with PISSARRO (left), SW$_f$-TPPM (middle) and AM-XiX (right) at B_0 = 9.7 T and three spinning frequencies ν_{rot}. The optimized *rf* amplitudes ranged between 10 and 11 kHz to get the best efficiency in each case. All spectra were recorded with a single pulse experiment, pre-saturation of ^{1}H during 15.0 ms, NS = 8 and 5 s delay between experiments. The observed increase of intensity of a quaternary aromatic carbon at lowest spinning frequency results from faster longitudinal relaxation.

All decoupling sequences use pulse durations that must be optimized for a given *rf* power. However, there is an unavoidable distribution of *rf* field amplitudes, mostly along the axis of the solenoid coil. To probe the consequences of this distribution on

the performance of heteronuclear decoupling, the $^{13}C^{\alpha}H$ peak heights were calculated numerically, again considering a spin cluster $C^{\alpha}H^{\alpha}H^{\beta1}H^{\beta2}H^{N}$ in L-histidine with high- and low-amplitude PISSARRO decoupling at 9.7 and 19.9 T and ν_{rot} = 60 kHz (Fig. 6.7).

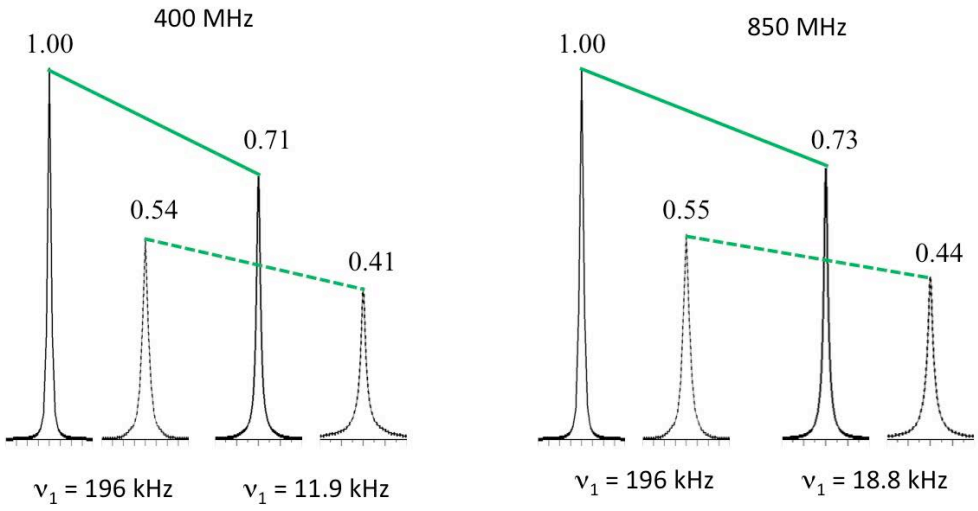

Figure 6.7: Numerically calculated $^{13}C^{\alpha}H$ lines considering a spin cluster $C^{\alpha}H^{\alpha}H^{\beta1}H^{\beta2}H^{N}$ in L-histidine with high- and low-amplitude PISSARRO at B_0=9.4T (left) and 19.9 T (right) and ν_{rot} = 60 kHz. The lines were calculated assuming either a single *rf* amplitude (i.e., a perfectly homogenous *rf* field, shown by solid lines) or a realistic distribution of rf fields calculated for a solenoid coil with an inner diameter of 1.5 mm and a length of 2.5 mm (dashed lines). The optimized high- and low-amplitude pulse durations were 18.48 μs ($1.109*\tau_{rot}$) at both fields and 264.0 μs (corresponding to a nutation angle ~ $3.14\times2\pi$) at 400 MHz and 218.16 μs (or nutation angle ~ $4.1\times2\pi$) at 850 MHz. The resulting full-width at half-height (FWHH) ranged between 2.2 and 2.8 Hz for high- and low-aplitude decoupling respectively.

The peak heights were simulated assuming either a single *rf* amplitude (i.e., a perfectly homogeneous *rf* field) or a realistic distribution of *rf* field amplitudes, calculated using the Bio-Savart law for a solenoid coil with internal diameter of 1.5 mm and 2.5 mm length. The relative *rf* intensity ranges from 100% in the center of the coil to 56% at the edges. Interestingly, much better agreement with the experimental 16 % drop of the $^{13}C^{\alpha}H$ peak height (Fig. 6.5 left) is noted when assuming the relevant inhomogeneity of the *rf* field which leads to a 20 % drop, while with the homogeneous *rf* field it stands for a 27 - 29 % drop. More strikingly, when taking into account the inhomogeneity of the *rf* field, the drop of the peak heights is

close to 45 % for both high- and low-amplitude regimes and for both static fields. A similar decrease of efficiency due to the *rf* field inhomogeneity is expected for other decoupling schemes. This reveals further potential for improving the sensitivity by designing new heteronuclear decoupling methods, especially in the low-amplitude regime, provided one can design a compensation for the *rf* field inhomogeneity. This little-explored aspect will be thoroughly examined in chapter 7.

6.4 Conclusions

We have compared the performance of a few recent heteronuclear decoupling schemes at high magic-angle spinning frequencies where the choice of a particular scheme is not merely of academic interest but important for routine applications. The results show that at commonly used *rf* amplitudes $80 < \nu_1^H < 120$ kHz, the decoupling performance of PISSARRO compares favorably with other decoupling schemes and provides substantial sensitivity improvements. This is due to its unique capacity to quench rotary resonance recoupling near the $n = 2$ condition. Although a loss of intensity of about 15 - 25% is observed with current pulse sequences for low-amplitude decoupling at a spinning frequency $\nu_{rot} = 60$ kHz, compared to the high-amplitude regime, the losses are more pronounced at lower spinning frequencies. This compels one to resort to *rf* amplitudes $80 < \nu_1^H < 100$ kHz where PISSARRO decoupling reveals the best performance, compared with other currently used decoupling schemes, all of which need much higher *rf* amplitudes under such conditions to reach the same decoupling efficiency. We have also demonstrated by numerical simulations that for sample having an axial length equal to that of the solenoid coil, the inherent inhomogeneity of the *rf* field may lead to a decrease of sensitivity by more than 40 %, both in the high- and low-amplitude decoupling regimes. This suggests that further improvements in sensitivity could be achieved when dealing with fully packed rotors, by designed new scheme for heteronuclear decoupling with suitable compensation for the *rf* field inhomogeneity.

6.5 References

1. Häeberlen, U., High resolution NMR in solids : selective averaging. 1976, New York [u.a.]: Acad. Pr.
2. Mehring, M. Principles of High Resolution NMR in Solids. 1983;
3. Schmidt-Rohr, K. and H.W. Spiess, Multidimensional solid-state NMR and polymers. 1994, London; San Diego: Academic Press.
4. Tekely, P., P. Palmas, and D. Canet, *J. Magn. Reson. A* 1994, 107 (2), 129-133.
5. Bennett, A.E., C.M. Rienstra, M. Auger, K.V. Lakshmi, and R.G. Griffin, *J. Chem. Phys* 1995, 103 (16), 6951-6958.
6. Gan, Z. and R.R. Ernst, *Solid State Nucl. Magn. Reson.* 1997, 8 (3), 153-159.
7. Yu, Y. and B.M. Fung, *J. Magn. Reson.* 1998, 130 (2), 317-320.
8. Edén, M. and M.H. Levitt, *J. Chem. Phys* 1999, 111 (4), 1511-1519.
9. Fung, B.M., A.K. Khitrin, and K. Ermolaev, *J. Magn. Reson.* 2000, 142 (1), 97-101.
10. Detken, A., E.H. Hardy, M. Ernst, and B.H. Meier, *Chem. Phys. Lett.* 2002, 356 (3–4), 298-304.
11. De Paëpe, G., P. Hodgkinson, and L. Emsley, *Chem. Phys. Lett.* 2003, 376 (3–4), 259-267.
12. Weingarth, M., P. Tekely, and G. Bodenhausen, *Chem. Phys. Lett.* 2008, 466 (4–6), 247-251.
13. Thakur, R.S., N.D. Kurur, and P.K. Madhu, *Chem. Phys. Lett.* 2006, 426 (4–6), 459-463.
14. Vinther, J.M., A.B. Nielsen, M. Bjerring, E.R. Van Eck, A.P. Kentgens, N. Khaneja, and N.C. Nielsen, *J. Chem. Phys.* 2012, 137 (21), 214202.
15. Madhu, P.K., *Isr. J. Chem.* 2014, 54 (1-2), 25-38.
16. De Paëpe, G., N. Giraud, A. Lesage, P. Hodgkinson, A. Böckmann, and L. Emsley, *J. Am. Chem. Soc.* 2003, 125 (46), 13938-13939.
17. Bax, A., R. Freeman, and T.A. Frenkiel, *J. Am. Chem. Soc.* 1981, 103 (8), 2102-2104.
18. Lesage, A., C. Auger, S. Caldarelli, and L. Emsley, *J. Am. Chem. Soc.* 1997, 119 (33), 7867-7868.
19. Gullion, T. and J. Schaefer, *J. Magn. Reson.* 1989, 81 (1), 196-200.
20. Raleigh, D.P., M.H. Levitt, and R.G. Griffin, *Chem. Phys. Lett.* 1988, 146 (1–2), 71-76.
21. Weingarth, M., G. Bodenhausen, and P. Tekely, *Chem. Phys. Lett.* 2010, 488 (1–3), 10-16.
22. Oas, T.G., R.G. Griffin, and M.H. Levitt, *J. Chem. Phys* 1988, 89 (2), 692-695.
23. Weingarth, M., G. Bodenhausen, and P. Tekely, *J. Magn. Reson.* 2009, 199 (2), 238-41.
24. Weingarth, M., G. Bodenhausen, and P. Tekely, *Chem. Phys. Lett.* 2011, 502 (4–6), 259-265.
25. Weingarth, M., J. Trebosc, J.P. Amoureux, G. Bodenhausen, and P. Tekely, *Solid State Nucl. Magn. Reson.* 2011, 40 (1), 21-6.
26. Vinther, J.M., N. Khaneja, and N.C. Nielsen, *J. Magn. Reson.* 2013, 226 (0), 88-92.
27. Agarwal, V., T. Tuherm, A. Reinhold, J. Past, A. Samoson, M. Ernst, and B.H. Meier, *Chem. Phys. Lett.* 2013, 583 (0), 1-7.

28. Veshtort, M. and R.G. Griffin, *Journal of magnetic resonance* 2006, 178 (2), 248-282.
29. Paul, S., V.S. Mithu, N.D. Kurur, and P.K. Madhu, *Journal of magnetic resonance* 2010, 203 (1), 199-202.
30. De Paëpe, G., A. Lesage, and L. Emsley, *J. Chem. Phys.* 2003, 119 (9), 4833-4841.
31. Mithu, V.S., S. Pratihar, S. Paul, and P.K. Madhu, *Journal of magnetic resonance* 2012, 220, 8-17.
32. Purusottam, R., G. Bodenhausen, and P. Tekely, *J. Biomol. NMR* 2013, 57 (1), 11-19.
33. Kotecha, M., N.P. Wickramasinghe, and Y. Ishii, *Magn. Reson. Chem.* 2007, 45 (SUPPL.), S221-S230.

7 Effect of inherent rf field inhomogeneity on heteronuclear decoupling in solid-state NMR

7.1 Introduction

Efficient heteronuclear decoupling is essential to obtain high-resolution NMR spectra of organic and biological solids containing protons and low-gamma nuclei such as carbon-13. In this chapter we present a detailed analysis of the effect of the inherent rf field inhomogeneity on decoupling by the low-power phase-inverted supercycled sequence for attenuation of rotary resonance (PISSARRO) [1].

All modern decoupling sequences use pulse lengths that must be optimized for a given *rf* power. However, there exists an inherent distribution of *rf* field amplitudes, mostly along the axis of the solenoidal coil. Typically, the relative *rf* amplitude varies from 1.0 in the center of the coil to about 0.5 at its edges. Inevitably, the effect of the rf field distribution manifests itself for fully packed rotors during any decoupling irradiation. To the best of our knowledge, the consequences of the *rf* inhomogeneity on the performance of heteronuclear decoupling have not been thoroughly examined so far. In chapter 6, we have demonstrated by numerical simulations, both in high- and low-power decoupling regimes, that the loss of the peak height due to the inhomogeneity of the *rf* field can reach as much as 40 % for a sample with a length equal to that of the solenoidal coil [2]. Below we discuss alternative ways for improving the efficiency of PISSARRO decoupling by minimizing the impact of the inherent *rf* field inhomogeneity along the axis of the solenoidal coil.

7.2 Experiments and numerical simulations

All experiments were run on 400 and 850 MHz spectrometers with 1.3 mm rotors spinning at a frequency ν_{rot} = 60 kHz. Uniformly ^{13}C, ^{15}N labeled L-histidine was purchased from Cambridge Isotopes and used without further purification. For spatially restricted samples, the top and bottom parts of the rotor were filled with compressed KBr powder. Other experimental details are included in the figure captions. All numerical simulations were carried out with SPINEVOLUTION [3]

considering the 5-spin system $C^{\alpha}H^{\alpha}H^{\beta 1}H^{\beta 2}H^{N}$ of L-histidine hydrochloride monohydrate, with internuclear distances derived from the crystallographic structure.

7.3 Results and discussion

Low-power PISSARRO decoupling with an ideal homogeneous rf field

Spinning at frequencies above 30 kHz may lead to a dramatic breakdown of the decoupling efficiency over a wide range of *rf* amplitudes. This is due to the phenomenon of rotary resonance recoupling (R^3), which can occur when the *rf* amplitude matches a multiple of the spinning frequency ($\nu_{1H} = n\nu_{rot}$) [4]. To overcome this drawback, PISSARRO decoupling was developed and shown to be effective in quenching rotary resonance recoupling in the vicinity of $n = 2$ [1]. The method also turned out to be very efficient at high *rf* amplitudes when $\nu_{1H} >> \nu_{rot}$, far above any R^3 condition, as well as in a regime with low *rf* power and fast spinning, e.g., when $\nu_{1H} < \nu_{rot}$ [5]. This is due in part to its capacity to reduce interference between the modulation of dipolar couplings by the *rf* field and by spinning [1]. A thorough analysis of the mechanism of quenching of rotary resonance recoupling effects by the PISSARRO scheme has revealed the crucial role of mirror symmetry segments combined with phase shifts [6] . The immunity of PISSARRO decoupling against the offsets of remote protons, their chemical shift anisotropies and second-order cross-terms between these anisotropies and dipolar couplings has also been demonstrated [6, 7].

To visualize the basic response of spin systems to low-power PISSARRO irradiation, Fig. 7.1 shows simulations of the dependence of the decoupling efficiency as a function of the *rf* amplitude ν_{1H} (Fig. 7.1b) and the pulse length τ_p (Fig. 7.1c), assuming a perfectly homogeneous *rf* field and a static field 19.97 T (850 MHz for protons) for a spinning frequency $\nu_{rot} = 60$ kHz.. The relaxation induced homogeneous broadening and the inhomogeneous broadening of the resonance peaks was not included in the simulations.

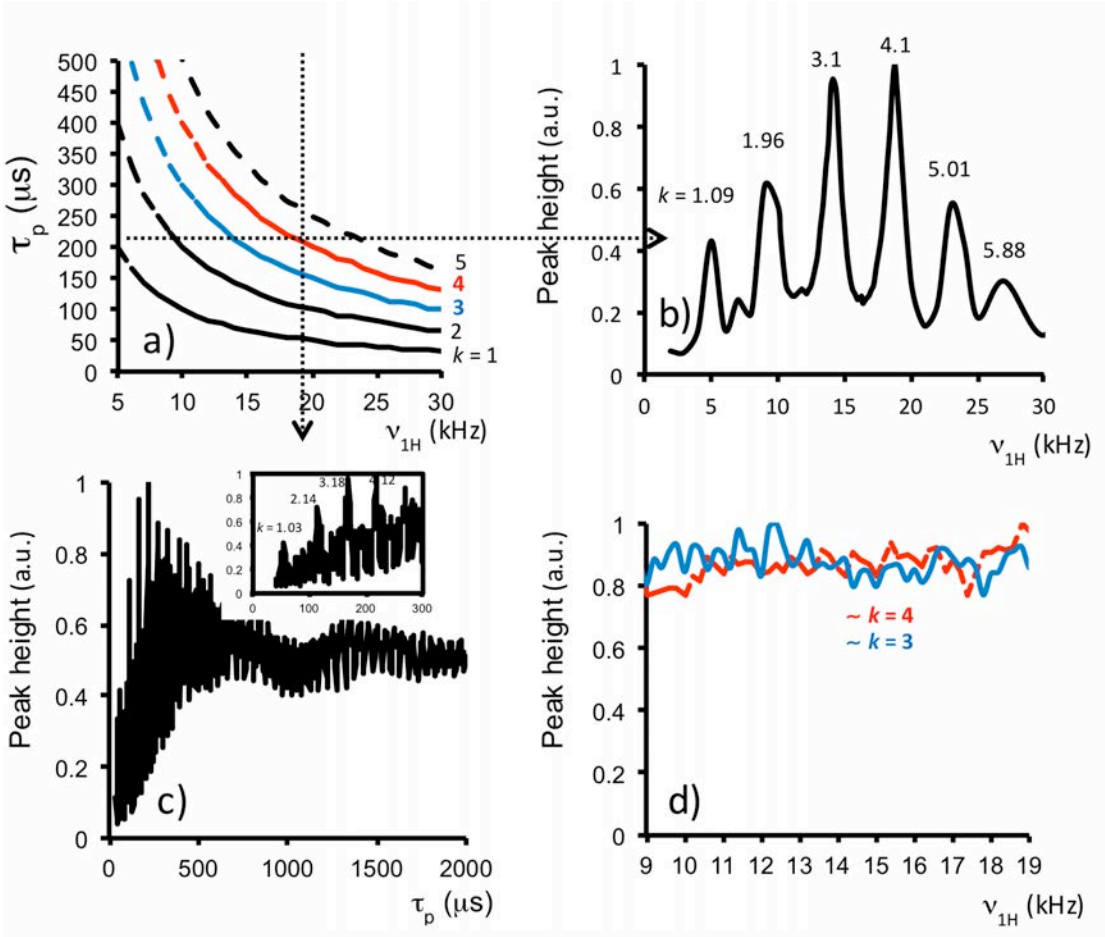

Figure 7.1: Numerical simulations of the efficiency of low-power PISSARRO decoupling in a magnetic field 19.97 T (850 MHz for protons) for a spinning frequency 60 kHz, assuming a perfectly homogeneous *rf* field. (a) Relationship between the pulse length τ_p and the *rf* amplitude ν_{1H} when the nutation angles β of the pulses are multiples of 2π, i.e., $\beta = 2\pi k$ where k is in the vicinity of integer values $k = 1, 2, \ldots$ (b) Numerical simulations of the height of the $^{13}C^{\alpha}H$ resonance of L-histidine as a function of the *rf* amplitude for a fixed pulse length $\tau_p = 218.16$ µs. (c) Simulated height of the $^{13}C^{\alpha}H$ resonance of L-histidine as a function of the pulse length for a fixed *rf* amplitude $\nu_{1H} = 18.8$ kHz. (d) Simulated height of the $^{13}C^{\alpha}H$ resonance of L-histidine as a function of the *rf* amplitude for optimized pulse lengths τ_p with nutation angles $\beta = 2\pi k$ in the vicinity of $k = 3$ and 4.

The figure shows that decoupling is most efficient when the pulse length τ_p is chosen so that the nutation angle β is in the vicinity of a multiple of 2π, i.e. $\beta = 2\pi\nu_{1H}\tau_p = k2\pi$ with integer $k = 1, 2, 3,\ldots$ According to our earlier observations, the undesirable 'dips' in Fig. 7.1c are due to recoupling effects that occur when the pulse duration coincides with a multiple of a quarter the rotor period [1, 4]. Note that the two highest maxima near $k = 3$ and 4 indicate a good performance over a wide range of *rf* amplitudes $10 < \nu_{1H} < 20$ kHz (Fig. 7.1d).

Analogous numerical simulations (not shown) for a static field B_0 = 9.4 T (400 MHz for protons) show a very similar response. This corroborates earlier observations of the effective immunity of PISSARRO against offsets of remote protons and their chemical shift anisotropies [5, 7].

Effects of the inherent rf field inhomogeneity

As mentioned above, all modern decoupling sequences make use of pulse lengths that must be experimentally optimized for a given *rf* power. Naturally, there exists an inherent distribution of *rf* field amplitudes across the volume of a sample in a solenoidal coil. The effects may be appreciated in Fig. 7.2 which shows nutation envelopes recorded for three differently packed rotors: (a) a fully packed rotor, (b) a sample with an axial length equal to and roughly coinciding with that of the solenoidal coil, and (c) a sample consisting of a ca. 1 mm disk that is located near the center of the coil. The top and bottom parts of the rotor were filled with compressed KBr powder. The striking differences in signal decay reflect the distribution of the *rf* field amplitude ν_{1H} across the volume of the sample. The most pronounced decay is observed for a fully packed rotor due to signals from the top and bottom parts of the sample that are located near and beyond the edges of the coil. The decay is somewhat less pronounced when the sample has a length matched with the coil.

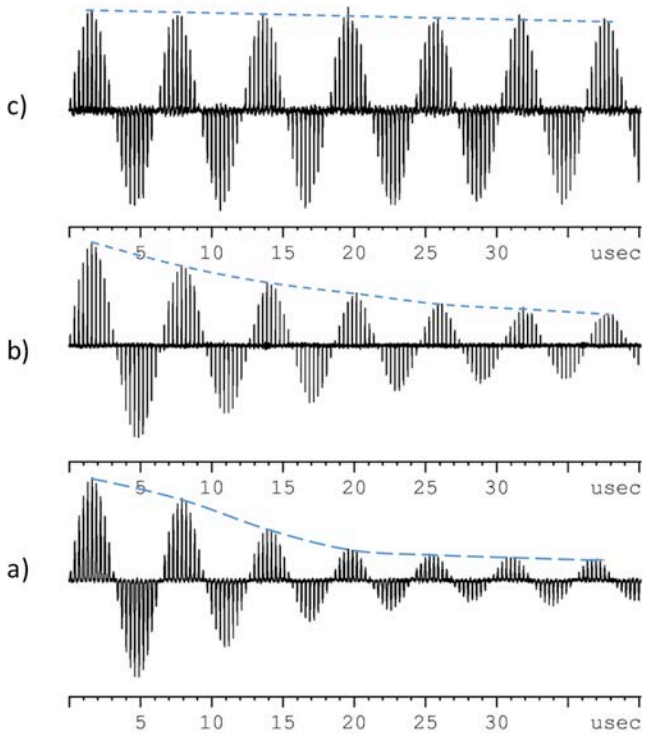

Figure 7.2: Experimental height of the ^{13}C-H peak of L-histidine as a function of the length of a ^{1}H pulse preceding cross-polarization, recorded for (a) a fully packed rotor, (b) a sample with an axial length roughly coinciding with the 2.5 mm length of the solenoidal coil, and (c) a sample with a thickness limited to ~1.0 mm (c). For (b) and (c) the top and bottom parts of the rotor (~1.25 mm and ~2.0 mm on both ends, respectively) were filled with plugs of KBr powder. All experiments were run at 400 MHz. For convenience, the nutation envelopes were normalized to the same maximum height; their actual amplitudes drop by about 10 % in (b) and 50 % in (c).

A disk-shaped sample is naturally exposed to a more limited distribution of *rf* field amplitudes, although the decay due to such distribution is not completely suppressed. Indeed, using phase-alternated pulses we checked that the remaining decay observed in Fig. 7. 2c is not due to relaxation effect.

To compare the decoupling performance in the presence and absence of *rf* inhomogeneities, one needs to know the actual variation of the *rf* field along the axis of a solenoidal coil. Figure 7.3a shows simulations of the *rf* field for a solenoidal coil with an inner diameter of 1.5 mm and a length of 2.5 mm, calculated using the Biot-Savart law. The relative *rf* intensity ranges from 1.0 in the center of the coil to 0.56 at its edges. To probe the consequences of this non-uniform *rf* field on the decoupling performance for a sample with a length equal to and coincident with the solenoidal coil, we have compared numerical simulations for an ideal homogeneous *rf* field. Since the main variation is along the axis of the solenoidal coil, we have omitted

radial variations of the *rf* field near the edges of the solenoidal coil, although these may induce first-order spinning sidebands of small amplitude that are independent of the spinning frequency [8].

As shown in Fig. 7.3b and 7.3c, the *rf* field distribution leads to dramatic effects on the simulated peak heights. This is a direct consequence of different decoupling efficiencies at different locations in the sample for a given pulse length and nominal *rf* amplitude (*vide infra*).

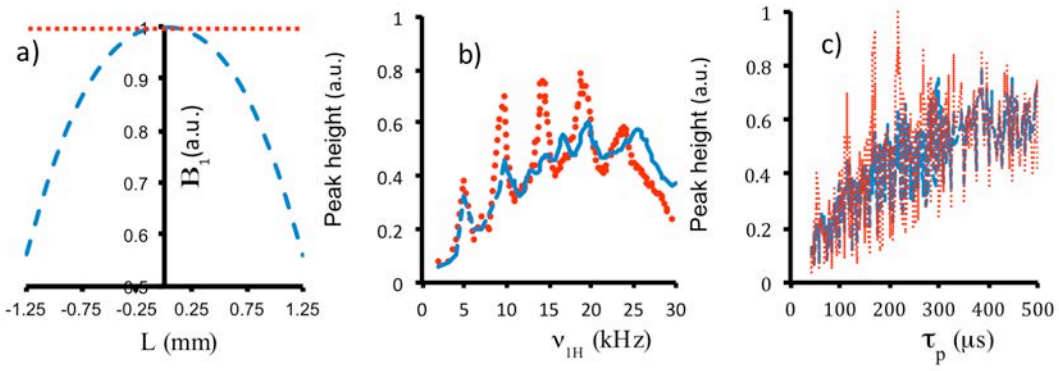

Figure 7.3: Effect of the inhomogeneity of the *rf* field on the efficiency of low-power PISSARRO decoupling. (a) The amplitude of the *rf* field B_1 calculated with the Biot-Savart law along the axis of a solenoidal coil with 1.5 mm internal diameter and 2.5 mm length (blue dashed line). The red dotted line refers to an ideal homogeneous *rf* field. (b) Calculated height of the $^{13}C^{\alpha}H$ resonance of L-histidine as a function of the nominal *rf* amplitude for a pulse length τ_p = 220 μs and an ideal homogeneous *rf* field (red dotted line) and for an inhomogeneous *rf* field (blue dashed line). (c) Calculated height of the $^{13}C^{\alpha}H$ resonance of L-histidine as a function of the pulse length τ_p for a nominal *rf* amplitude ν_{1H} = 18.8 kHz, either for an ideal homogeneous *rf* field (red dotted line) or for an inhomogeneous *rf* field (blue dashed line). The numerical simulations assumed a sample with a length equal to that of the solenoidal coil. All other parameters are as in Fig. 7.1

Fig. 7.4 shows experimental intensities of $^{13}C^{\alpha}H$ peaks of a disk of L-histidine powder that is only ~1.0 mm thick and that is placed approximately in the center of the *rf* coil, recorded as a function of the *rf* amplitude. The intensities were calculated by assuming the same parameters with *rf* variations of 40% along the length of the coil. The experimental maxima appear close to a nutation angle $\beta = 2\pi k$ with integer k = 2, 3, …, a feature that is neatly reproduced by numerical simulations. However, despite the spatially restricted sample, the experimental intensities of maxima are weaker, and they appear broader than in the calculated envelopes, especially for long pulse lengths

(τ_p). This is due to homogeneous and inhomogeneous broadening that was not included in the simulations, to the fact that the sample may not have been placed exactly in the center of the coil (*vide infra*), and that the slice of histidine powder may have been somewhat thicker than 1 mm.

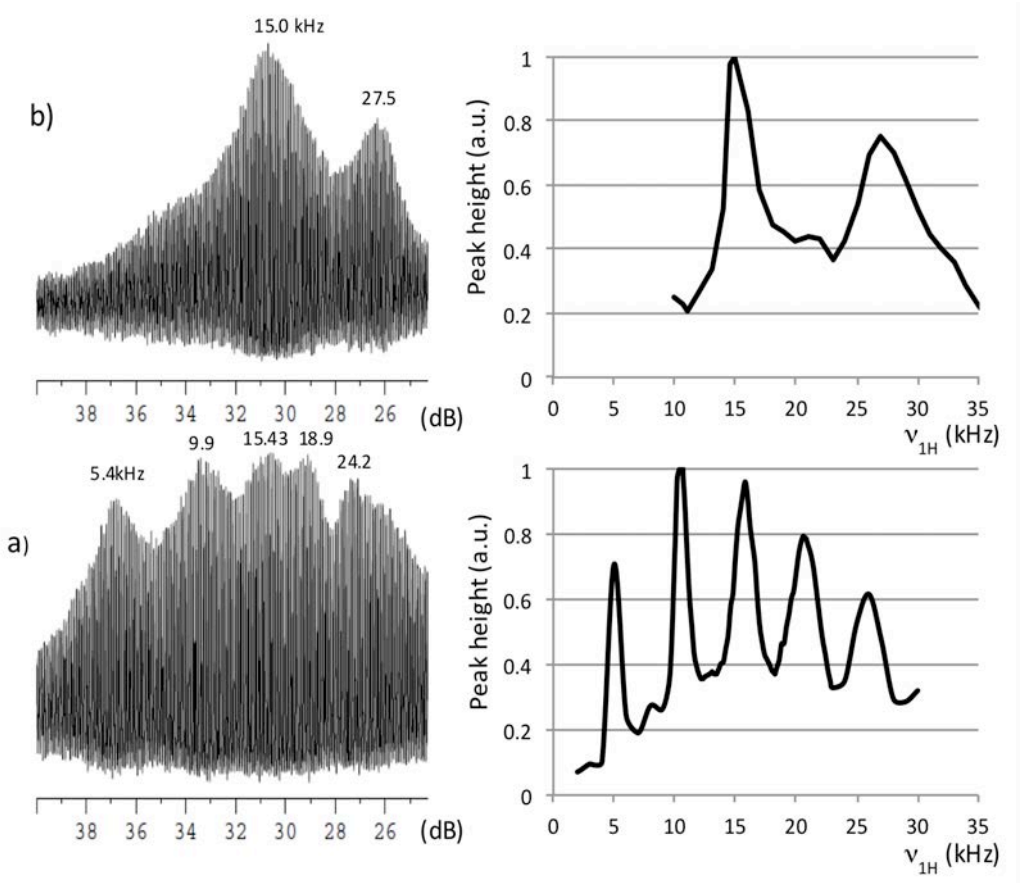

Figure 7.4: (Left) Experimental $^{13}C^{\alpha}H$ peak heights of a thin disk with a thickness of ~1.0 mm of L-histidine powder roughly centrally located with respect to the *rf* coil, recorded as a function of the decoupling *rf* amplitude, expressed in dB of attenuation. The top and bottom parts of the rotor were filled with KBr powder (two plugs of ~2.0 mm length.). The spectra were obtained on a 400 MHz spectrometer with ν_{rot} = 60 kHz using a pulse length τ_p = 204 μs in (a) and τ_p = 69 μs in (b). (Right) Corresponding $^{13}C^{\alpha}H$ peak heights calculated for the relevant *rf* inhomogeneities.

Similar differences are observed when comparing experimental and calculated intensities of the $^{13}C^{\alpha}H$ peaks as a function of the pulse length τ_p (Fig. 7.5). As expected, the shorter the pulse lengths, the higher the *rf* amplitudes must be to reach the best decoupling efficiency with a nutation angle β close to a multiple of 2π (Fig. 7.4).

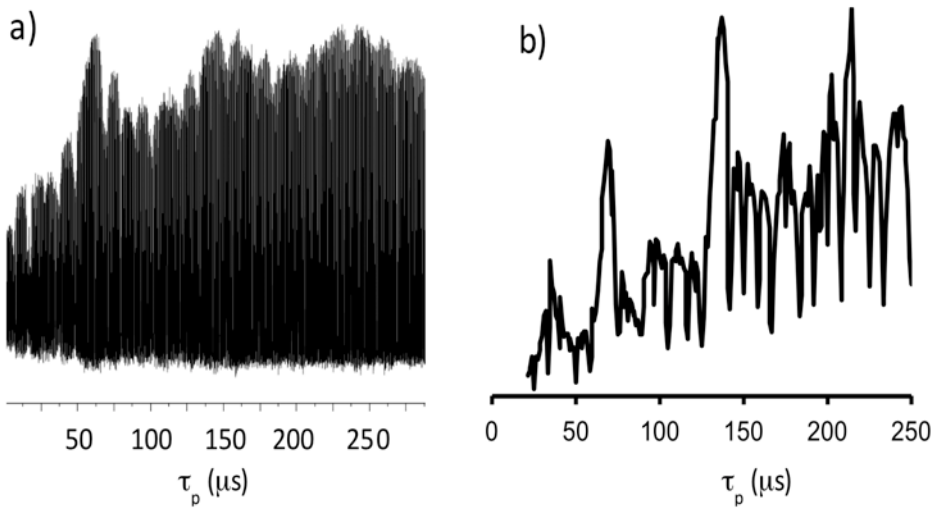

Figure 7.5: (a) Experimental $^{13}C^{\alpha}H$ peak heights of L-histidine as a function of the pulse length τ_p, recorded with an average *rf* decoupling amplitude $<\nu_{1H}>$ = 14.8 kHz. The sample consisted of a thin disk of ~ 1.0 mm that was roughly centered with respect to the *rf* coil. The spectra were obtained at 400 MHz with a spinning frequency ν_{rot} = 60 kHz. (b) Calculated intensities of the $^{13}C^{\alpha}H$ peak with the same parameters.

Figure 7.6 shows experimental $^{13}C^{\alpha}H$ peaks of L-histidine as a function of the *rf* amplitude for a sample with a length equal to and roughly coinciding with that of the solenoidal coil, and for a slice of ca. 1 mm thickness positioned near the center of the coil. The heights of the $^{13}C^{\alpha}H$ peaks were calculated by averaging over the relevant *rf* distributions. For a sample that is exposed to a wide distribution of *rf* amplitudes, both the experimental and calculated envelopes appear shallow and are shifted in frequency for *rf* amplitudes below 20 kHz.

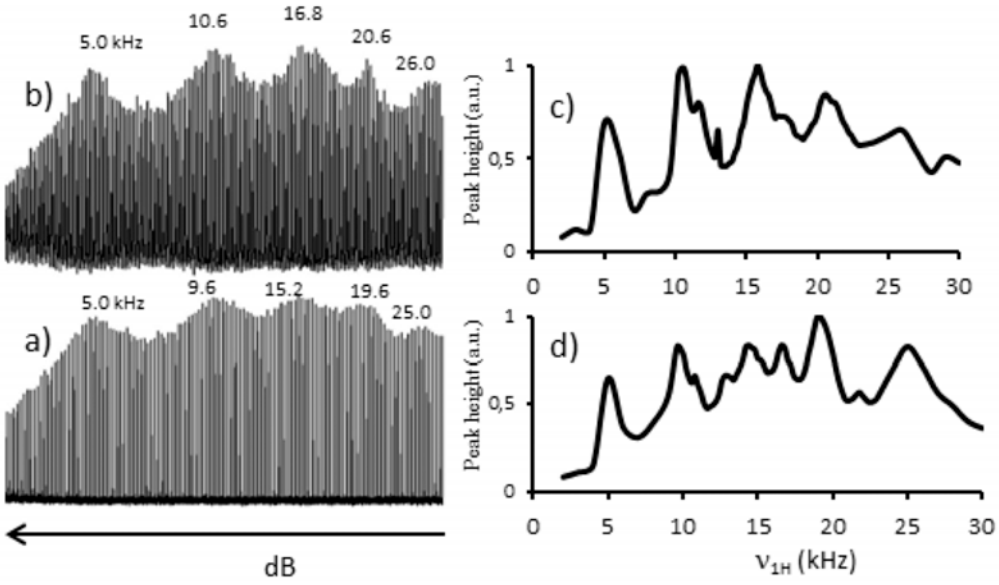

Figure 7.6: (Left) Experimental $^{13}C^{\alpha}H$ peak heights of L-histidine recorded as a function of the decoupling *rf* amplitude. (a) For a sample having a length equal to that of the *rf* coil. (b) For a sample consisting of a disk of ~ 1.0 mm thickness that was roughly centered with respect to the *rf* coil. The spectra were obtained on a 400 MHz spectrometer with ν_{rot} = 60 kHz using optimized pulse lengths (a) τ_p = 218 μs and (b) τ_p = 202 μs for an average *rf* amplitude $<\nu_{1H}>$ = 18.8 kHz. To facilitate the comparison, the experimental envelopes were normalized to the same maximum height; the actual drop in peak height is about 50 % in (b). (Right) Corresponding envelopes of the $^{13}C^{\alpha}H$ peak heights calculated with the same parameters and relevant *rf* inhomogeneities.

To further probe the effects of the position of the sample, Fig. 7.7 compares the envelopes of peak heights calculated for a slice of 1 mm thickness that is either centered with respect to the coil (blue solid line), or placed near the edge of the coil (green dashed-dotted line), compared with a sample having an axial length equal to and coinciding with that of the coil (red dashed line). Although the experimental envelope recorded for a centrally placed thin disc roughly reproduces the calculated envelope (blue solid line), its maxima are again strongly attenuated which must be mostly due to inhomogeneous broadening that is a more pronounced in a high static field. Beside effects similar to those observed in Figs. 7.4 and 7.6, a pronounced loss of peak height is calculated for low *rf* amplitudes when the disk is placed near the edge of the coil. This is yet another indication that the *rf* field inhomogeneity plays a key role, since the efficiency of decoupling critically depends on the spatial position of the sample.

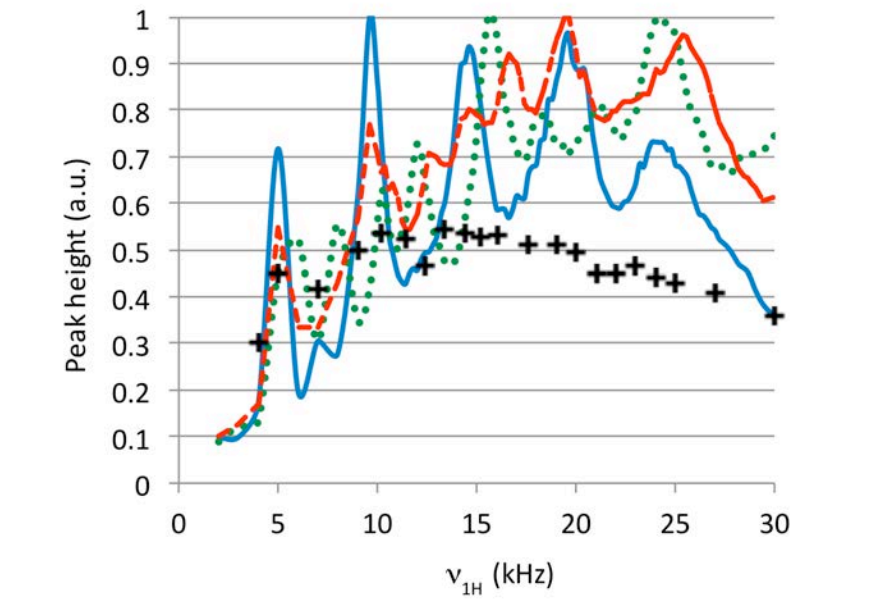

Figure 7.7: Calculated ^{13}C-H peak heights of L-histidine as a function of the nominal *rf* amplitude including the relevant inhomogeneity for a sample consisting of a thin disk of ~ 1.0 mm thickness that was assumed to be either (blue solid line) centered with respect to the *rf* coil or (green dotted line) placed near its edge. (Red dashed line): similar calculations for a sample having a length equal to that of the coil. All calculated graphs are normalized to the same maximum height. All numerical simulations used the same parameters. The experimental intensities (black crosses, arbitrary normalized) were recorded on a 850 MHz spectrometer with ν_{rot} = 60 kHz for a sample consisting of a thin slice of ~ 1.0 mm thickness that was roughly centered with respect to the *rf* coil, using a pulse length τ_p = 220 μs.

Towards a compensation for rf field inhomogeneity

Knowing the inherent variations of the *rf* field amplitude along the axis of a solenoidal coil and the response of the spin system to PISSARRO irradiation with a given pulse length and *rf* amplitude, one can visualize idealized decoupling efficiency for different spatial positions of a sample having a length matched with the length of the coil (Fig. 7.8).

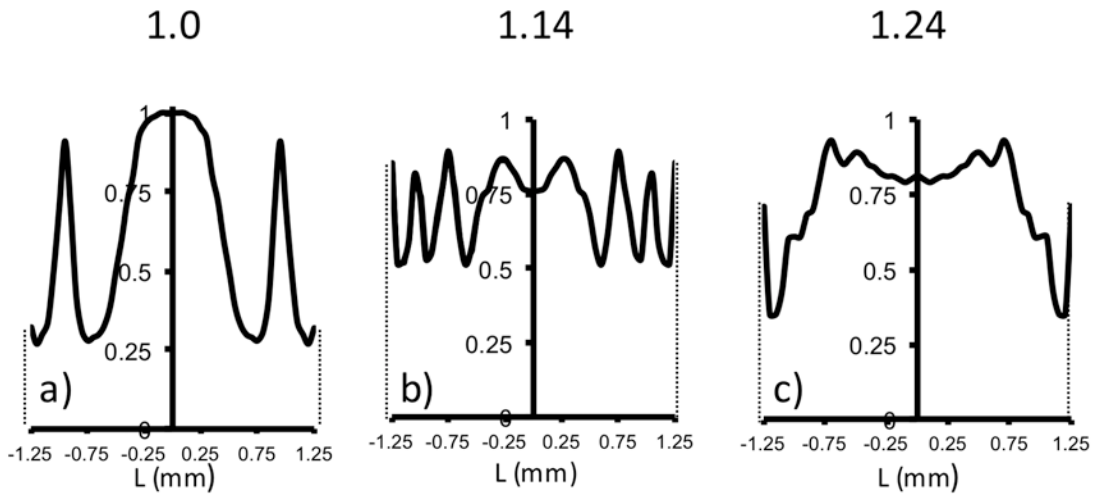

Figure 7.8: Spatial profiles of the $^{13}C^{\alpha}H$ peak heights calculated for pulse lengths (a) τ_p = 218 μs and (b) τ_p = 386 μs, and (c) using two different pulse lengths τ_p = 297 and 386 μs in the basic phase-inverted pulse pair of the PISSARRO sequence, taking into account variations of the *rf* field along the axis of a coil of 2.5 mm length. All simulations assumed a nominal *rf* amplitude ν_{1H} = 18.8 kHz, all others parameters being as in Fig. 7.7. The numbers give the normalized integrated intensity (area under the graphs) of each spatial profile.

The spatial profile of the decoupling efficiency (as reflected in the peak height of the $^{13}C^{\alpha}H$ resonance of histidine) has been calculated for an optimal pulse length τ_p = 218 μs and a nominal *rf* amplitude ν_{1H} = 18.8 kHz (Fig. 7.8a). As expected (see Fig. 7.7), this reveals the best decoupling in the central part of the coil extending over 20% of its length, plus two narrow off-centered positions. However, the remaining spatial positions suffer from significant losses in decoupling efficiency that penalize the global performance. Remembering that PISSARRO decoupling with fully packed rotors is one of the most efficient [1, 2, 4, 5] of recently proposed schemes, losses due to the *rf* field distribution are expected to be similar for other decoupling pulse sequences. Although, as shown in Fig. 7.8b, the dips in the peak heights of Fig. 7.8a can be partially alleviated by using a longer pulse length τ_p = 386 μs, this goes at the expense of the efficiency of decoupling in the central part of the coil. However, the integrated intensity (area under the graph) grows by 14 % as compared with Fig. 7.8a. Interestingly, an improved gain of 24 % takes place when combining two different pulse lengths within the phase-inverted basic pulse pair of the PISSARRO sequence (Fig. 7.8c). This is due to the fact that the central part of the decoupling profile that comprises roughly 60% of the total coil length now appears more uniform.

This suggests that the use of basic pulse pairs with two different pulse lengths could improve the global decoupling efficiency, especially in systems where relaxation and conformation induced homogeneous and inhomogeneous broadening of the resonance peaks is not too severe.

7.4 Conclusions

All modern decoupling sequences use pulse lengths that are optimized for a nominal *rf* amplitude. However, there is an inherent distribution of *rf* field amplitudes that has harmful effects for all decoupling schemes. We have demonstrated that for low power PISSARRO decoupling the distribution of the *rf* field across the volume of the sample can have a significant impact on the performance. Even for small samples, this can lead to a decrease of the peak heights. In spite of the fact that PISSARRO is one of the most efficient schemes, both in the high and low-power decoupling regimes, a detailed analysis has revealed further potential for improving its efficiency by employing variable pulse lengths to minimize the effects of the *rf* field inhomogeneity. This will be of special practical interest for systems with modest relaxation induced homogeneous broadening and conformation determined inhomogeneous broadening.

7.5 References

1. Weingarth, M., P. Tekely, and G. Bodenhausen, *Chem. Phys. Lett.* 2008, 466 (4–6), 247-251.
2. Purusottam, R.N., G. Bodenhausen, and P. Tekely, *Chem. Phys. Lett.* 2014, 614 (0), 220-225.
3. Veshtort, M. and R.G. Griffin, *J. Magn. Reson.* 2006, 178 (2), 248-282.
4. Oas, T.G., R.G. Griffin, and M.H. Levitt, *J. Chem. Phys* 1988, 89 (2), 692-695.
5. Weingarth, M., G. Bodenhausen, and P. Tekely, *J. Magn. Reson.* 2009, 199 (2), 238-41.
6. Weingarth, M., G. Bodenhausen, and P. Tekely, *Chem. Phys. Lett.* 2011, 502 (4–6), 259-265.
7. Weingarth, M., J. Trebosc, J.P. Amoureux, G. Bodenhausen, and P. Tekely, *Solid State Nucl. Magn. Reson.* 2011, 40 (1), 21-6.
8. Tekely, P. and M. Goldman, *J. Magn. Reson.* 2001, 148 (1), 135-141.

Résumé :
RMN à l'état solide est devenue un outil de premier plan pour la caractérisation morphologique, structurale et dynamique de protéines microcristallines, de matériaux polymères, synthétiques ou naturels, de petites molécules d'intérêt pharmaceutique ou des minéraux. Les progrès dans la compréhension de la structure et de la dynamique des systèmes moléculaires à l'état solide sont très fortement dépendants des méthodologies mises en œuvre dans leurs études.

Cette thèse s'inscrit dans cette optique en portant l'effort principal sur certains aspects méthodologiques de la RMN à l'état solide, avec comme objectif de développer des nouvelles approches ou améliorer les méthodes déjà utilisées et ceci afin d'extraire de façon optimale des informations spécifiques sur le système de spins étudié. Les études fondamentales de systèmes solides d'intérêt biologique, la mise au point de nouvelles méthodologies ainsi qu'une analyse méthodologique approfondie forment l'essentiel de cette thèse ayant pour le dénominateur commun une amélioration de la sensibilité des expériences RMN à l'état solide. Le mémoire de thèse présente dans sa première partie de nouvelles approches dans les études structurales et dynamiques des protéines microcristallines, membranaires et fibrillaires ainsi qu'une étude dynamique et conformationnelle des chaines phospholipidiques dans les liposomes. La deuxième partie est essentiellement concentrée sur une analyse détaillée de certains aspects méthodologiques de la RMN du solide en relation avec le découplage dipolaire hétéronucléaire, indispensable dans l'obtention des spectres de haute résolution.

Mots clés : [rmn; solide; protéines; dynamiques; récouplage; découplage]

[Towards improved sensitivity of solid-state nmr experiments in biosolids]

Abstract :
Solid-state NMR has become a major tool for morphological characterization, structural and dynamic microcrystalline proteins, polymers, synthetic or natural materials, small molecules of pharmaceutical interest or minerals. Progress in understanding the structure and dynamics of molecular systems in the solid state are very heavily dependent on methodologies implemented in their studies.

This thesis in this context carrying the main effort on certain methodological aspects of NMR in the solid state, with the goal of developing new approaches and improve the methods already used and in order to extract optimum specific information on the spin system under study. The fundamental studies of solid biologically relevant systems, the development of new methodologies and a thorough methodological analysis form the core of this thesis with the common denominator for an improvement of the sensitivity of NMR experiments in solid state. The thesis presents the first part of new approaches in structural and dynamic studies microcrystalline proteins, membrane and fibrillar and a dynamic study and conformational channels in phospholipid liposomes. The second part is mainly concentrated on a detailed analysis of some methodological aspects of solid state NMR related heteronuclear dipolar decoupling essential in obtaining high resolution spectra.

Keywords : [nmr; solid, proteins, dynamics, recoupling; decoupling]